BRNO UNIVERSITY OF TECHNOLOGY

Faculty of Electrical Engineering and Communication

DOCTORAL THESIS

Brno, 2021   Ing. Martin Štůsek

BRNO UNIVERSITY OF TECHNOLOGY
FACULTY OF ELECTRICAL ENGINEERING AND COMMUNICATION
DEPARTMENT OF TELECOMMUNICATIONS

TAMPERE UNIVERSITY
FACULTY OF INFORMATION TECHNOLOGY AND COMMUNICATION SCIENCES
DEPARTMENT OF ELECTRICAL ENGINEERING

RESEARCH ON RELIABLE LOW-POWER WIDE-AREA COMMUNICATIONS UTILIZING MULTI-RAT LPWAN TECHNOLOGIES FOR IOT APPLICATIONS

DOUBLE DEGREE PROGRAMME BETWEEN BRNO UNIVERSITY OF TECHNOLOGY AND TAMPERE UNIVERSITY

DOCTORAL THESIS

AUTHOR	MSc. Martin Štůsek
ADVISORS	Prof. Evgeny Kucheryavy, Ph.D.
	Assoc. Prof. Jiří Hošek, Ph.D.

BRNO 2021

ABSTRACT

This doctoral thesis addresses the "Research on Reliable Low-Power Wide-Area Communications Utilizing Multi-RAT LPWAN Technologies for IoT Applications". Despite the immense progress in massive Machine-Type Communication (mMTC) technology enablers such as Low-Power Wide-Area (LPWA) networks, their performance does not have to satisfy the requirements of novelty Internet of Things (IoT) applications. The main goal of this Ph.D. work is to explore and evaluate the limitations of current LPWA technologies and propose novel mechanisms facilitating coverage planning and assessment. Proposed frameworks are fine-tuned and cross-validated by the extensive measurement campaigns conducted in public LPWA networks. This doctoral thesis further introduces the novelty approach of multi-RAT LPWA devices to overcome the performance limitation of individual LPWA technologies. The current implementation primarily focuses on diminishing the greatest multi-RAT solutions disadvantage, i.e., increased power consumption by employing a machine learning approach to radio interface selection.

KEYWORDS

Typeset by the `thesis` package, version 4.00; `http://latex.feec.vutbr.cz`

DECLARATION

I declare that I have written the Doctoral Thesis titled "Research on Reliable Low-Power Wide-Area Communications Utilizing Multi-RAT LPWAN Technologies for IoT Applications" independently, under the guidance of the advisor and using exclusively the technical references and other sources of information cited in the thesis and listed in the comprehensive bibliography at the end of the thesis.

As the author I furthermore declare that, with respect to the creation of this Doctoral Thesis, I have not infringed any copyright or violated anyone's personal and/or ownership rights. In this context, I am fully aware of the consequences of breaking Regulation § 11 of the Copyright Act No. 121/2000 Coll. of the Czech Republic, as amended, and of any breach of rights related to intellectual property or introduced within amendments to relevant Acts such as the Intellectual Property Act or the Criminal Code, Act No. 40/2009 Coll., Section 2, Head VI, Part 4.

Brno   . . . .
author's signature

ACKNOWLEDGEMENT

Contents

List of Figures

List of Tables

1   Introduction

The current trend of joining various Internet of Things (IoT) networks and technologies under one umbrella of mutually connected services, also known as Heterogeneous IoT (HetIoT), represents a research field that has strong potential. HetIoT is currently gaining momentum in numerous areas, including smart homes, smart cities, intelligent transportation, smart metering, Industry 4.0, and wearables [1–3]. With such an extensive basis, HetIoT will influence our lives, providing convenient services for the upcoming years. The current IoT and Machine-to-Machine (M2M) solutions already represent heterogeneous systems consisting of wireless sensor networks, mobile networks, wireless mesh networks, vehicular networks, and Low-Power Wide-Area (LPWA) technologies [4,5]. However, radically diverse requirements of IoT applications, communication technologies, and heterogeneity of network architecture make the development of HetIoT applications extremely complex task [6].

1.1   State-of-the-Art M2M Communication

At its core, IoT targets ubiquitous interconnected devices with unique digital identities monitored and controlled by a central server. To provide real-time control, monitoring, and security management, IoT adopts various long and short-range wireless communication technologies. In other words, these HetIoT networks employ wireless communication modules, sensors, and other smart terminals for ubiquitous sensing at any time [2,6].

It is essential to bear in mind that coexisting heterogeneous network units limit the efficiency of channel resource utilization. With the ultimate goal of delivering the data from smart sensors over different environments, with hard-to-reach devices, the research of energy-efficient technologies, including LPWA has been initiated [4,7]. However, high adoption of HetIoT brings another challenge connected with congestion problems [8,9]. An immense number of concurrently communicating devices effectively prevents the system from operating in a timely manner. Therefore, it is crucial to optimize the scheduling of network resources with respect to unexpected/emergency events to be served – having a quality of service in mind. Future research tasks also include exploring new networking models for HetIoT, big data integration, data privacy, and seamless transfer in heterogeneous network units [2,5,10]. This work is not trying to give all answers but rather concentrates on LPWA technologies as enablers of M2M communication and recently also massive Machine-Type Communication (mMTC) in heterogeneous LPWA networks.

The upswing of LPWA technologies is primarily initiated by the massive growth of M2M communication throughout the last decade [11]. These new wireless commu-

nication technologies are solely oriented on extended coverage and prolonged battery life. In line with the M2M requirements, LPWA technologies are primarily designed for small data transmissions over long distances while maintaining reduced power consumption [12, 13]. It is expected that LPWA technologies will cover a variety of applications, including personal IoT applications, home automation, assets tracking, smart grids, and infrastructure monitoring, see Fig. 1.1.

Fig. 1.1: LPWAN technology use cases [13].

Concentrating on the fundamental parameter of the LPWA, which is long-range, the large link budget is needed. Usually, LPWA technologies operate with a link budget ranging between 140 and 160 dB. With such capabilities, it is possible to reach a communication distance of 5 km in the urban environment and more than 10 km in rural areas. Extended coverage is also connected with receivers' sensitivity. In the case of LPWA, communication modules providing sensitivity of more than -130 dBm are not rare. To achieve these sensitivity levels, LPWA technologies use a slower modulation rate requiring narrowband channels (usually smaller than 25 kHz). Based on the Shanon-Hartley theorem slowing the modulation rate by half increases the energy of each bit/symbol twice – thus, it increases the link budget two times (+3 dB) as well. Such an approach, however, negatively influences the resulting data-rate [12, 14]. For example, Sigfox utilizes a modulation rate of 100 Bd with one-bit Binary-Phase Shift Keying (BPSK) modulation. Hence, it results in the final data rate of 100 bps, which may look archaic, but it is still sufficient for certain undemanding M2M applications [15].

Another option how to achieve a large link budget is to spread the energy of a narrowband channel across a wider band and incorporate processing (coding) gain.

This approach is so effective that it is possible to receive signals below the noise floor (Signal-to-Noise Ratio (SNR) < -20 dB). Generally, coded signals provide better performance in terms of minimum detectable energy, with higher resilience to jamming and narrowband interferences. On the other hand, the spectrum is not utilized as effectively as in the case of narrowband technologies. Considering a 100 Hz channel operated by Ultra-Narrowband (UNB) technology Sigfox, the thermal noise level is -154 dBm. With the required SNR of 10 dB, the theoretical maximum sensitivity reaches -144 dBm. For the 125 kHz spread-spectrum channel utilized by LoRaWAN technology, the thermal noise power increases to -124 dBm. Therefore even with the 20 dB coding gain, we can only achieve the same sensitivity of -144 dBm, as in the case of the narrowband signal [14–16].

With the same level of importance, the extended battery life of 10+ years is critical to reducing M2M devices' maintenance costs. To achieve prolonged battery life, LPWA technologies implement optimizations in all vertical of the communication infrastructure, including (i) network topology, (ii) Duty Cycle (DC), (iii) transceiver complexity, and (iv) lightweight Medium Access Control (MAC) layer [4].

The use of mesh topology to extend the coverage is not optimal for LPWA networks as it requires dense infrastructure to provide reliable services. Also, the routing protocols used in mesh networks bring additional communication overheads, require more complex devices, increase the cost, and leads to reduced battery life. LPWA technologies, on the other hand, use a simple star or start-of-stars topology with a single-hop transmission. It brings significant energy savings on the End-Device (ED) side as the complex tasks are delegated to the Base Station (BS), which usually continuously listens for incoming data transmission on multiple frequencies (channels). Further, the ED can initiate the transmission without prior connection setup. Moreover, the channel access is mainly based on purely random Abramson's Logic of Hiring Access (ALOHA) protocol, or in the case of Third-Generation Partnership Project (3GPP) standards, more deterministic slotted ALOHA is utilized [4, 13].

1.2 Research Motivation

The unprecedented growth of the IoT sector and M2M communication influences even the usually rigid industry sectors including Supervisory Control and Data Acquisition (SCADA) systems. The beginnings of SCADA systems can be traced back to the 1960s [17, 18]. In these times, the systems heavily relied on telephony lines, and the monitoring functionality was hard-wired to the equipment as the solid-state devices were in the infancy stage. However, the giant step forward came in

the 1970s with minicomputers based on 8 or 16-bit processors. The minicomputers automatized the operators' tasks and offered additional functions like scanning, monitoring, and alarming. Further advancement led to the appearance of microprocessors, the basis for Programmable Logic Controller (PLC)s. The programmability, being the most significant assets of PLC, allowed vendors to develop more efficient and cost-effective systems. Since then, the SCADA has evolved into the complex interconnected Internet Protocol (IP)-based systems communicating mostly via an Ethernet connection [17–19].

Though the SCADA systems were initially designed for inside-the-fence applications, they are also rapidly adopted in outside-the-fence scenarios. The fastest adoption is currently in the energy distribution sector, i.e., water, electricity, and natural gas. However, the adoption of SCADA in the outside-the-fence application brought new challenges. In the case of remote assets, both power and communication coverage are crucial. Inside-the-fence SCADA assets, located in the manufacturing plant, have access to an unlimited, reliable power source. In contrast, remotely located SCADA assets usually rely on batteries, representing a strongly limited power source. A further challenge comes with signal coverage. The devices may operate in areas with severe radio conditions, i.e., underground construction, remote deployments, or deep indoor applications. For the telecommunication operators, it can be uneconomical to cover these places with conventional technologies. However, novelty LPWA technologies may help to solve both battery-life and signal coverage issues [17, 20].

Also, the recent wireless networks statistics reveal the importance of wide-area IoT in the following years. According to the Ericsson mobility report [21], the number of wide-area IoT connections will grow from 1.6 billion in 2019 to 5.5 billion in 2025. On top of that, more than half of IoT connections will be realized by cellular LPWA technologies, including LTE-Cat M and Narrowband IoT (NB-IoT). Globally, Cisco's annual internet report [11] forecasts a 14 % market share of the LPWA technologies by 2023, representing the fastest-growing mobile communication segment. In total, it means growth from 223 million LPWA devices in 2018 to 1.9 billion in 2023.

However, the massive growth of IoT and M2M communication predicted by the leading technology companies is not groundless. Within the European Union, the Third Energy Package obligates the member states to implement smart metering deployments as a part of a climate-neutral economy by 2050. The most significant progress has been made in smart electricity meters deployment, where the European Commission expects at least 80 % market penetration by 2021. Namely, it represents almost 245 million connected devices. However, in the case of gas and water, market adoption is much lower. As each smart metering device must provide a remote

interface, in most cases supplied by wireless technologies, this market offers enormous potential for LPWA technologies [22].

Also, the smart meters vendors are aware of the LPWA technologies' importance in this area. The latest Device Language Message Specification (DLMS)/Companion Specification for Energy Metering (COSEM) release, the de facto global standard for energy metering, control, and management, introduced a new LPWAN profile. This new profile defines how the COSEM data model and the DLMS/COSEM application layer can be transported via various LPWA technologies using the Static Context Header Compression and Fragmentation (SCHC) framework. The adaptation layer represents a set of mechanisms providing header compression/decompression and optional fragmentation/reassembly algorithms for underlying LPWA MAC/PHY layers. From the perspective of higher layers, the standard builds upon full IPv6, User Datagram Protocol (UDP), and COSEM wrapper headers. Currently, the LPWAN profile emphasizes LoRaWAN and NB-IoT technologies, but the adoption of other standards is also possible [23, 24].

1.3 Scope of the Dissertation

Based on the facts mentioned in Section 1.2, it is clear that LPWA technologies will play a crucial role as mMTC enablers in the upcoming years. Therefore, it is necessary to evaluate their performance in real-world applications and eliminate the shortcomings. With the advent of new demanding mMTC scenarios, single LPWA technology does not have to be sufficient in terms of communication reliability and delay. Thus the multi-RAT LPWA solutions may be crucial to fulfill these demands. However, it will be vital to select technologies that complement each other in their strengths and weaknesses in such a case. On top of that, it will be necessary to develop radio interface selection algorithms mitigating the increased power consumption of multiple RATs. These tasks represent the main goals of this doctoral thesis.

To this aim, this doctoral thesis provides a comprehensive analysis of current LPWA technologies in all verticals from the signal propagation up to multi-RAT optimizations. In particular, the primary goals are divided into three subsequent research studies:

- **LPWA Propagation Models** - the precise prediction of signal propagation in the radio environment represents the uppermost question during any wireless technology design. The development of such empirical propagation models requires to conduct a large-scale measurement campaign, data-fitting, and accuracy verification. For this purpose, a new quantitative comparison metric

is introduced. Also, the developed models' accuracy is cross-verified by the second measurement campaign.

- **Coverage Assessment Planning** - the assessment of radio network coverage is an essential task for network deployment and maintenance. However, the conduct of measurement campaigns on such a scale is a costly and time-consuming process. Therefore, any reduction of required measurements is beneficial. To this aim, this work proposes a new methodology of measurement point selection without the explicit knowledge of BS locations based on well-known interpolation algorithms.

- **Multi-RAT Solution for mMTC Scenarios** - the most crucial challenges of multi-RAT deployments include increased power consumption and automatic radio interface selection. Both these issues can be addressed by using machine learning algorithms. Specifically, Reinforcement Learning (RL) algorithms solving the Multi-Armed Bandit (MAB) problem seems to be a viable solution. However, to gain a sufficient length of traces, also doubly-stochastic Markov chain model is developed. This model represents a convenient tool for characterizing the dynamics of the radio interface. Further, it is needed to have precise knowledge of power consumption in each operating condition and state. Therefore, results of the power measurement campaign serve as the basis of the developed battery-life expectancy model used by the RL algorithms.

1.4 Dissertation Outline and Main Results

This doctoral thesis consists of six individual chapters covering the author's research between 2016 and 2021. The provided results represent the most significant outcomes of the author's work published in well-recognized scientific journals, proceedings of international conferences, and book chapters. Overall the thesis is logically structured in order to provide insight into all critical parts of research on low-power wide-area communications utilizing multi-RAT LPWA technologies for IoT applications. The introduction section enlights the state-of-the-art heterogeneous networks, closely followed by the description of LPWA technologies' fundamental principles and features. Chapter 2 is dedicated to MTC's history in legacy communication systems, followed by a description of emerging mMTC use cases in both IoT and Industry 4.0. Finally, the second chapter concludes by reporting on mMTC enablers, namely LPWA technologies, and their connection with the multi-RAT approach. Going further, Chapters 3 – 5 contain the core ideas as well as the main outputs of this doctoral thesis.

Chapter 3 describes two large-scale measurement campaigns of LPWA technologies in two major cities in the Czech Republic. The chapter further provides a com-

parison of commonly used sub-GHz empirical propagation models from three primary sources: (i) standardization bodies, (ii) vendors/operators, and (iii) academia. The accuracy of selected models is ranked based on the developed quantitative metric, and the best-performing ones are used in the derivation of the new propagation models. Then, data from the second city are used to verify the accuracy of newly created models to provide coherent results.

Building upon the acquired knowledge, Chapter 4 provides a comprehensive framework for assessing network deployments radio conditions with the minimum number of measurement points. The developed toolbox estimates the signal quality of LPWA technologies in the closest proximity of the measurement point by utilizing well-known interpolation methods. Further, two proposed thinning algorithms reduce the number of measurement points in a sequential manner to evaluate the accuracy of the interpolation with decreasing number of generating points. The first thinning algorithm uses a probabilistic approach, whereas the second one addresses this issue deterministically.

Going further, Chapter 5 deals with the battery life optimization of LPWA multi-RAT devices. Incorporating data from the long-term measurements allow developing a doubly stochastic Markov model for generating traces of arbitrary length used in subsequent machine learning algorithms. With power consumption results acquired during an extensive measurement campaign of several modules, it is possible to predict the behavior of LPWA technologies in the whole operational range. In terms of LPWA, it means Maximum Coupling Loss (MCL) values of up to 164 dB [25] and signal levels as low as -135 dBm. This consumption data denotes the rewards for the selected RL policies. Identically to the MAB problem, the RL algorithms' ultimate goal is to choose the arm with the highest average rewards. Theoretically, it leads to the highest achievable battery life possible.

Finally, Chapter 6 concludes the whole doctoral thesis.

2 Massive Machine-Type Communications in 5G Era

In the course of the last decade, we are witnessing an unprecedented paradigm shift from human-oriented communication towards the direct data exchange between machines. According to Cisco annual report, M2M applications will represent 50 % of the connected devices by 2023. It is also expected that the M2M connections will be the fastest-growing category of devices [11].

It is also reflected in the rise of communication technologies solely oriented on M2M applications. These technologies include LPWA representatives from license-exempt spectrum such as Sigfox and LoRaWAN along with 3GPP-defined ones like LTE Cat M1/M2 or NB-IoT. However, M2M plays a crucial role also in 5G New Radio (NR), see Table 2.1. Within the 5G ecosystem, mMTC serves as an enabler of M2M communication [4, 7, 26].

2.1 Legacy Communication Systems

Before the arrival of 5G technologies, the mobile networks were primarily designed with Human-to-Human (H2H) communication in mind. In other words, the main focus was given to human-centric communication, such as voice services or data transmissions in the Downlink (DL) direction [27]. The first shift in this paradigm came with 3GPP Release 10, which introduced initial steps towards the M2M capable networks [28].

However, mobile network technologies ratified by 3GPP are not the only communication standard available. The need for effective transmission of small data units with low frequency gave rise to a plethora of long-range wireless technologies. Nevertheless, with the advent of 5G NR and LPWA networks, these legacy technologies lost momentum and became relevant only in particular use cases [29, 30].

2.1.1 3GPP-Based Technologies

The 3GPP originated as a consortium associating several national standards development organizations aiming to develop a technical specification for the third generation of the cellular communication system. Aside from this task, 3GPP also provided maintenance and improvements to legacy second-generation mobile networks. The purpose of this consortium did not vanish after the introduction of the third-generation cellular systems. Contrary, the 3GPP further continued with the development of fourth and later fifth-generation mobile networks [31, 41, 42].

Tab. 2.1: Overview of 3GPP Releases [28, 31–40].

3GPP Relase	Release date	Details
Phase 1	1992	Basic GSM specification
Phase 2	1995	GSM extension including EFR Codec
Release 96	Q1 1997	GSM updates, 14.4 kb/s user data rate
Release 97	Q1 1998	GSM additional features, GPRS
Release 98	Q1 1999	GSM additional features, GPRS for GSM 1900, EDGE, AMR Codec
Release 99	Q1 2000	3G UMTS with WCDMA
Release 4	Q1 2001	UMTS all-IP core network
Release 5	Q1 2002	IMS and HSDPA
Release 6	Q4 2004	HSUPA, MBMS, IMS enhancements, PTT over cellular, WLAN cooperation
Release 7	Q4 2007	Improvements in QoS and latency, VoIP, HSPA+, NFC integration, EDGE evolution
Release 8	Q4 2008	LTE introduced, system architecture evolution, OFDMA, MIMO, dual cell HSDPA
Release 9	Q4 2009	WiMAX/LTE/UMTS interoperability, dual cell HSDPA with MIMO, dual cell HSUPA, LTE Home eNodeB
Release 10	Q1 2011	LTE Advanced, Backward compatibility with Release 8, Multi-Cell HSDPA, MTC subscription, congestion and overload control
Release 11	Q3 2012	HetNet, CoMP, in-device coexistence, advanced IP interconnection of services, on-line device triggering, PS-only service provisioning
Release 12	Q1 2015	Enhanced small cell operation, extended carrier aggregation, massive Multiple-Input Multiple-Output (MIMO), UE Cat 0, PSM, D2D communication, MBMS enhancements
Release 13	Q1 2016	LTE Unlicensed/License Assisted Access, LTE Cat M1, LTE Cat NB1, elevation beamforming, full dimension MIMO, indoor positioning
Release 14	Q2 2017	LTE support for V2X, in-band carrier aggregation, LTE Cat M2, LTE Cat NB2, mission critical enhancements
Release 15	Q4 2018	5G Phase 1, mMTC, V2X Phase 2, WLAN and unlicensed spectrum use, network slicing, service-based architecture
Release 16	Q3 2020	5G Phase 2, V2X Phase 3, URLLC, unlicensed NR, satellite access in 5G, integrated access and backhaul
Release 17	∼2021	Low complexity NR devices, NR >52.6 GHz, edge computing in 5G, MIMO enhancements

2G Networks

The first commercially available digital mobile networks started to appear in the nineties. In Europe, these networks utilized a Global System for Mobile Communication (GSM), representing the second generation (2G) of cellular technologies. GSM uses the principle of switching physical circuits with channel access based on Time-Division Multiple Access (TDMA). On top of the voice services, GSM also provides data transfer capabilities via the switched circuits. However, with the boom of data application at the end of the second millennium, the Circuit-Switched Data (CSD) reached its limits. As a result, the 3GPP consortium released an extension of the GSM providing packet-based communication. With General Packet Radio Service (GPRS), it is possible to achieve data rates ranging from units to tens of kb/s, depending on the signal quality, the mobile station capabilities (modulation coding schemes, multi-slot support), and the available radio resources. Further improvements in the transmission speed were brought by Enhanced Data rates for GSM Evolution (EDGE) technology. With the newly introduced eight-state Phase Shift Keying (PSK), the data rates can reach up to two hundred kb/s [35, 36].
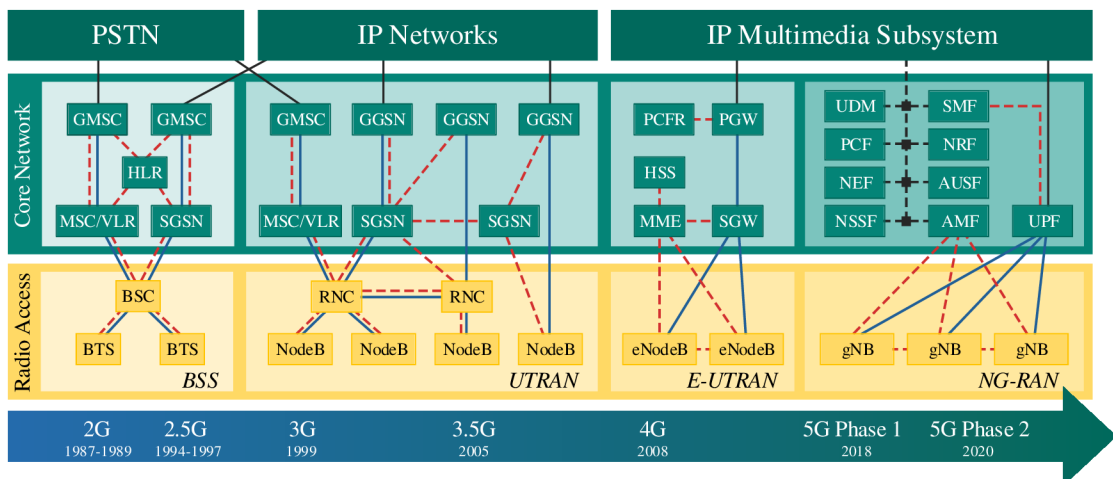
Fig. 2.1: 3GPP technologies evolution [43].

3G Networks

At this point, the introduction of the third-generation (3G) mobile networks was a logical step. This generation is represented by Universal Mobile Telecommunications System (UMTS) (mainly in Europe) and Code Division Multiple Access (CDMA) 2000 (mostly in the American continent). Both technologies utilize the novelty approach of channel access called CDMA. This access method allows using the same frequency band in neighboring cells. Combined with the introduction of multi-state modulation and a three-level channel model (transport, logical, and

physical), CDMA also significantly increased the access network effectiveness. However, the overall architecture of the system is adopted from 2G networks, see Fig. 2.1. Hence, the core of the access network consist of BS and controllers. In the backbone part, the circuit-switched domain for voice services is used, and the so-called packet-switched domain provides packet-oriented applications. Also, the increase of transmission speed in the order of few hundreds of kb/s compared to the EDGE technology was only marginal [35, 36].

The remarkable improvements in transmission speed were introduced with High-Speed Downlink Packet Access (HSDPA), and High-Speed Uplink Packet Access (HSUPA) joined into High-Speed Packet Access (HSPA) specification. Depending on the User Equipment (UE) technical specification and the operator's policy, it was possible to reach the speed of units of Mb/s up to tens of Mb/s. Besides the increased throughput, network latency (mainly in its access part) was significantly reduced by moving some Radio Network Controller (RNC) functions to the UMTS BS called Node B. Further innovations were introduced with HSPA+ supporting the Multiple-Input Multiple-Output (MIMO) technique, dual-carrier HSDPA, and 64 states Quadrature Amplitude Modulation (QAM) [35, 36].

4G Networks

A further step towards the new generation of mobile networks came with a unified way of providing telecommunication services. At this point, all services provided by the system are packet-oriented, i.e., Internet Protocol (IP) based. To this aim, the access part of the network was modified by removing the base station controllers and introducing a new access solution based on Orthogonal Frequency-Division Multiple Access (OFDMA). The whole radio access network thus contains only one type of element called evolved Node B (eNodeB) as depicted in Fig. 2.1. Together with other improvements, these steps enable the system to reach the latency in the order of tens of ms in the radio part. This already does not prevent the deployment of services running in real-time [34, 44].

These specifications are part of 3GPP Release 8, and they have been the basis for the first generation of Long Term Evolution (LTE) devices. Even though this release brought a significant amount of innovations, according to International Telecommunication Union (ITU) requirements on International Mobile Telecommunications-Advanced (IMT-Advanced) standard, it can not be considered as a fourth-generation (4G) network. It is also worth mentioning that this release introduced the first study on facilitating M2M communication in the 3GPP system. One year after the initial introduction of LTE, 3GPP Release 9 has been released. This standard still does not fulfill 4G requirements but introduces the concept of femtocells (home eNodeB),

19

adds support for Multimedia Broadcast Multicast Service (MBMS), and extends the Location Based Services (LBS) functionality. In terms of M2M, this release provides a feasibility study on the security aspects of remote provisioning and change of subscription for M2M equipment [44].

The following 3GPP Release 10, also known as LTE Advanced, is the first specification fulfilling the IMT-Advanced specification. Thus, it is the first real 4G network standard. The data rate of more than 1 Gb/s, requested by IMT-Advanced, is achieved mainly via carrier aggregation. Further improvements include enhanced MIMO operation in both directions, new communication bands, self-optimizing networks, LTE relays, and enhancements to MBMS. However, this release focuses also on the issues of M2M communication in the LTE terminology called MTC. Firstly it is an MTC subscription which allows activating/deactivating particular MTC feature in a unified manner. The subscription to a specific MTC service is bound with International Mobile Subscriber Identity (IMSI) stored in Universal Subscriber Identity Module (USIM). Further, Release 10 provides four different ways to address network congestion and overload. These countermeasures specify (i) low access priority, (ii) attach with IMSI at Public Land Mobile Network (PLMN) change, (iii) long minimum periodic PLMN search time, and (iv) specific handling of invalid USIM states. Since not all planned Machine-Type Communication (MTC) features were implemented, the remaining tasks were moved into 3GPP Release 11. The main changes included finalization of MTC architecture for better cooperation with MTC devices in external networks, on-line device triggering, and Packet Switched (PS)-only service provisioning [27, 28, 34].

2.1.2 Non-3GPP

The arrival of LPWA technologies represented a great leap forward for M2M communication. However, even before, there were technologies designed explicitly for machine type communication. Naturally, they do not possess the same versatility and parameters as the LPWA technologies but share a significant resemblance with them. Similar to LPWA, the legacy technologies predominantly utilized sub-GHz due to better signal propagation [14, 45]. For a more detailed comparison of legacy technologies in question, see Table 2.2.

IQRF

Introduced back in 2004 by Czech company Microdis, Intelligent Radio Frequency (IQRF) is among the first technologies solely focused on M2M communication. IQRF transceivers operate in the sub-GHz Industrial, Scientific and Medical (ISM) band with standardized frequencies 868, 433, or 916 MHz based on regional specifics

Tab. 2.2: Comparison of legacy M2M communication technologies [46–51].

	IQRF	**Wireless M-BUS**	**Wavenis**
Spectrum	ISM	ISM	ISM
Frequency	915/868/433 MHz	868/433/169 MHz	915/868/433 MHz
Bandwidth	100 kHz	12.5/50 kHz	25/50 kHz
Link budget	120 dB	120 dB 146 dB (169 MHz)	125 dB 137 dB (915 MHz)
Max. EIRP	10 dBm	14 dBm 30 dBm (169 MHz)	14 dBm 27 dBm (915 MHz)
Max. payload	64 B	245 B	N/A
Data rate	19.836 kb/s	2.4–32.768 kb/s	4.8–100 kb/s
Consumption	Tx: 25 mA Rx: 12 mA PSM: <1 uA	Tx: 37 mA, 703 mA (30 dBm) Rx: 22 mA PSM: <0.2 uA	Tx: 45 mA, 850 mA (27 dBm) Rx: 18 mA PSM: ~0.5 uA
Battery life	5–10 years	+10 years	5–10 years
Module cost	10$	12$	10$

and user requirements. In the most commonly used 868 MHz band, it is possible to utilize 62 channels, each having a 100 kHz bandwidth. Even though IQRF provides more than 1 km single-hop communication range (in free space), this technology's primary benefit lies in mesh topology. The coordinator controls the network and communicates in a synchronous manner with all other nodes. Each node belonging to the routing network further repeats the transmitted signal. As the routing nodes may transmit only in a specific interval, the collisions are excluded. This type of pathfinding is called directional flood routing based on Virtual Routing Number (VRN), which corresponds to the transmitter's physical location relative to the network coordinator and defines time interval when the node can convey the data [47, 49].

As the primary focus of IQRF is in M2M communication, the infrequent transmission of small data packets is expected. Thus the maximum payload of 64 B with the data rate of 19.836 kb/s is more than sufficient. In terms of communication delay, it is about 50 ms for the maximum payload. However, it must be reckoned with the mesh network topology. The value of 50 ms is valid for single-hop communication, but in the worst case of 240 hops (IQRF limitation), it leads to a 12 s delay in one direction. IQRF also promises a multi-year battery life by utilizing multiple power-saving features. During the data transmission, the consumption can be as high as 25 mA if the maximum output power of 10 dBm is selected. Notably, it is

only 12 mA in reception mode and may be reduced even further by activating the radio unit only in short intervals. In this mode, it is possible to reach the average consumption of around $16\,\mu$A. Nevertheless, the most significant power conservation can be achieved when the module is in sleep mode with a current consumption of only about $1\,\mu$A [47, 49].

Wireless M-BUS

This technology originated as an extension of the wired Meter BUS (M-BUS) standard utilized in smart metering systems, primarily in the European region. From the perspective of the Open Systems Interconnection (OSI) model, Wireless M-BUS represent a new physical and link layer defined by EN13757-4 standard from 2005. Higher layers are identical to Meter BUS standard [52].

Initially, Wireless M-BUS was designed for the 868 MHz band, where twelve 100 kHz channels are available. However, later it was extended by 433 and 169 MHz options. Aside from the better signal propagation on lower frequencies, also higher transmission power values can be used. A practical range of 600 m represented the maximum for the 868 MHz band at 14 dBm, whereas in the case of 169 MHz with 30 dBm, it is more than 2000 m. Wireless M-BUS also provides several operating modes that differ in the used frequency band, modulation, coding, directionality, and transmission speed. Mode S is designed for stationary devices requiring infrequent data transmission with a maximum throughput of 32.768 kb/s. Submodes $S1$ and $S2$ further define if the communication is unidirectional or bidirectional. In $S1$ mode the module goes back to the sleep mode immediately after data transmission. On the other hand, in $S2$, the module is waiting for a short time for incoming data. The T mode behaves the same as the S but provides 100 kb/s transmission speed and uses coding 3 of 6 instead of Manchester. Also, the submodes $T1$ and $T2$ are available. The C mode is identical to the T mode but utilizes NRZ coding. When the meter does not send data spontaneously, the $R2$ mode can be used. In this mode, the module wakes up periodically and waits for a wake-up frame. Then the bidirectional channel with a bit rate of 4.8 kb/s is opened. Finally, the N mode defines transmission in the 169 MHz band with several channels providing 2.4, 4.8, or 19.2 kb/s bitrate utilizing Gaussian Frequency Shift Keying (GFSK) or 4-GFSK modulation. Within this mode, it is possible to achieve the sensitivity of up to -119 dBm [50, 52, 53].

The Wireless M-BUS network has a star topology with the concentrator/master device in the center. Concentrator never initiates the communication but passively wait for incoming connections from client/slave end nodes. This behavior is also crucial for battery longevity. As the module spends most of its lifetime in sleep

mode, a battery life of more than 15 years is expected. In this mode, the consumption does not exceed $0.2\,\mu$A, while during the transmission, it is around 37 mA. When the bidirectional mode is selected, the power consumption during the reception is about 22 mA [51, 54].

Wavenis

Coronis Systems introduced Wavenis wireless protocol stack in 2005 as a solution for control and monitoring applications. Wavenis operates in ISM frequency bands, including 868, 433, and 915 MHz based on geographical location. Some of the devices also support the 2.4 GHz band in which Wavenis can cooperate with Bluetooth technology [46, 48].

The data rate may vary from 4.8 up to 100 kb/s based on the selected frequency and channel bandwidth. Nevertheless, only GFSK modulation is used for all configurations. In 433 and 868 MHz frequency bands, Wavenis may utilize one 25 kHz channel. This combination allows for the slowest data rate of 4.8 kb/s. However, with the 50 kHz channel, the data rate is doubled. As 16 channels are available, the Frequency Hopping Spread Spectrum (FHSS) technique improving resistance to interference is used. FHSS is also utilized in the 915 MHz band, where 50 channels are available, allowing for a data rate of 19.2 kb/s per channel. Nevertheless, the maximum throughput of 100 kb/s can be achieved only with a 300 kHz wide channel [46, 48].

The output power of 14 dBm, in combination with the 868 MHz frequency band, allows Wavenis to achieve a one-hop communication range of up to 1 km. Such coverage makes it usable even in a star topology, but Wavenis also support tree and mesh topologies extending the communication range. Like other M2M technologies, Wavenis focuses on the extended battery life of up to 10 years. In the idle mode, where the device spends most of the time, $3\,\mu$A consumption is expected. The highest consumption is during the data transmission with a peak value of 45 mA, followed by 18 mA in reception mode [46, 55].

2.2 MMTC Communication Enablers

With the increasing importance of M2M communication, mMTC was identified as one of the 5G technologies pillars. As a tremendous number of connected devices is expected, a set of basic requirements is defined. The complexity of the devices should be significantly reduced to keep the final price low. Due to the possibility of deployment in deep indoor locations, mMTC devices must provide extended coverage of +20 dB compared to conventional LTE networks. Moreover, the connection

Tab. 2.3: Comparison of current LPWA technologies [15, 56–64].

Technology	Sigfox	LoRaWAN	LTE Cat NB1	LTE Cat NB2	LTE Cat M1	LTE Cat M2
Spectrum	ISM	ISM	Licensed	Licensed	Licensed	Licensed
Frequency	868/915 MHz	433/868/915 MHz	700-2100 MHz	700-2100 MHz	700-2600 MHz	700-2600 MHz
Technology	Proprietary	PHY: Proprietary MAC: Open	Open LTE	Open LTE	Open LTE	Open LTE
Bandwidth	100, 600 Hz	125, 250, 500 kHz	200 kHz	200 kHz	1.4 MHz	5 MHz
Link budget	162 dB	157 dB	164 dB	164 dB	155.7 dB	155.7 dB
Max. EIRP	UL: 14 dBm[1] DL: 27 dBm	14 dBm	23 dBm	23 dBm	23 dBm	23 dBm
Max. payload	UL: 12 B DL: 8 B	242 B	1600 B	1600 B	8188 B	8188 B
UL data rate	0.1-0.6 kb/s	0.25-11 kb/s[2]	0.3-62.5 kb/s	0.3-159 kb/s	HD: 375,[3] 590 kb/s[4] FD: 1,[3] 3 Mb/s[4]	HD: 2.625 Mb/s FD: 7 Mb/s
DL data rate	0.6 kb/s	0.25-21.9 kb/s[2]	0.5-27.2 kb/s	0.5-127 kb/s	HD: 300,[3] 800 kb/s[4] FD: 0.8,[3] 1 Mb/s[4]	HD: 2.35 Mb/s FD: 7 Mb/s
Consumption	Tx: 14 mA RX: 7 mA PSM: <1 μA	Tx: 44 mA Rx: 12 mA PSM: <1 μA	Tx: 240 mA Rx: 46 mA PSM: 3 μA	Tx: 240 mA Rx: 46 mA PSM: 3 μA	Tx: 360 mA Rx: 70 mA PSM: 8 μA	Tx: 360 mA Rx: 70 mA PSM: 8 μA
Battery life	10+ years	10+ years	10+ years	10+ years	10+ years	10+ years
Module cost	2 $	6 $	8 $	10 $	10 $	10 $
Security	AES-128	AES-128	LTE Security	LTE Security	LTE Security	LTE Security

[1] The value is relevant for EU.   [2] 50 kb/s for FSK modulation.   [3] 3GPP Release 13.   [4] 3GPP Release 14.

density of devices can reach up to 1 million devices per square km. Still, the latency has to be less or equal to 10 seconds, even on the connectivity edge, i.e., with an Maximum Coupling Loss (MCL) of 164 dB. The battery life of the device operating at this MCL must overcome 10 years for the data transfer consisting of 200 and 50 B messages in UL and DL, respectively. This estimation operates with 5 Wh battery [25].

Although the requirements mentioned above are stringent, and covering all of them requires novelty approaches, one group of technologies is capable of this. The LPWA networks provide sufficient coverage, excellent battery life in reasonably priced devices. Also, global availability is ranking LPWA technologies among the best mMTC enablers. Notably, LPWA is currently the fastest-growing area of IoT and covers technologies from both licensed and license-exempt bands [11]. The first group defines the 3GPP ratified technologies, such as LTE Cat M1/2 and NB-IoT. The most typical representatives of the second group are Sigfox and LoRaWAN [26, 65–67].

2.2.1 Limitations of Legacy Technologies

Reflecting on the mMTC requirements given in the previous section, it is clear that non of the mMTC technologies until Release 12 could not fulfill any of these [28]. Even though the network infrastructure was already well established, allowing for almost arbitrary mobility. The main focus was given on the human-centric communication oriented towards high-speed DL transmissions. Also, the battery life was not great, and it was far from the expected +10 year. The first change came with the introduction of LTE Cat 0 devices in 3GPP Release 12. Having a reduced data rate of 1 Mb/s in both directions and an optional half-duplex mode allowed to reduce the modem complexity by 50 %. In combination with the newly introduced PSM, the theoretical lifetime was extended up to 10 years. However, the extended coverage and support for high-density deployments were not tackled until subsequent 3GPP Release 13. This release brought the first 3GPP ratified mMTC technologies, namely LTE Cat M1 and NB-IoT [28, 34, 38].

For the non-3GPP communication technologies, the situation was radically different. These technologies were already designed with the MTC concept to provide extended battery life and support for tens of thousands of devices in one network. However, they are still not capable of achieving the requested link budget of 164 dB. Mitigating impacts of insufficient MCL, legacy M2M technologies often provide advanced mesh topology. Although it allows extending the devices' communication range, it also decreases their battery life. Each hop in a mesh topology stands for message retransmission by an individual machine. The mesh routing protocols are
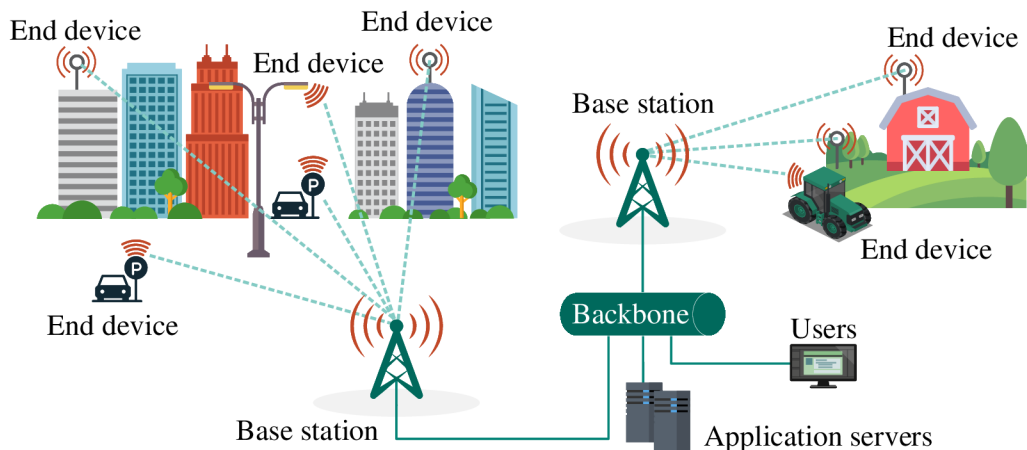
Fig. 2.2: Typical architecture of an LPWA network [68].

more computationally demanding, thus require more power. From this perspective, the star topology used by LPWA networks provides the best performance, see Fig. 2.2. The start topology requires only one powerful BS in its center, whereas the EDs may be extremely simple. The BS continuously listens for incoming messages, whereas the ED wakes up from sleep mode only to transmit the data [13, 14]. However, even the mesh topology was not the Achilles heel of legacy M2M technologies. The main problem lies in the non-existing infrastructure. Cellular networks are from the beginning planned to provide country-scale coverage. But the legacy M2M networks usually relied on a single BS. Practically it excludes any mobility, which is crucial for most of the IoT/mMTC scenarios. This is why the LPWA replaced these technologies and became the fastest growing area of IoT. Currently, Sigfox provides nationwide coverage in more than 70 countries. None of the legacy M2M can compete with such a developed infrastructure [12, 69].

2.2.2 3GPP-Based LPWA Technologies

As it was already mentioned, 3GPP Release 12 brought the first MTC capable class of devices [28]. From the perspective of M2M battery life, the most important novelty was the introduction of PSM. It is a special operating mode in which the device completely turns off the radio part. Naturally, it disallows any communication with eNodeB, but the consumption drops down to units of μA [56]. Prior to the PSM transition, the device has to negotiate the values of two timers, which drive the whole process. As it is depicted in Fig. 2.3a, the timer T3324 (GPRS Timer 2, Active Timer) defines the activity period, and T3412 (GPRS Timer 3, Periodic Tracking Area Update Timer) characterize the Tracking Area Update (TAU) period. Both

26

timers are activated immediately after the Radio Resource Control (RRC) release. The device still listens for incoming messages for the active period of timer T3324; then, the module proceeds to PSM by deactivating the radio part. When the timer T3412 reaches its set value, the device wakes up, conveys the TAU message, and the whole process is restarted. The maximum periods of T33224 and T3412 timers are 186 minutes and 413 days, respectively [70].

(a) PSM. (b) eDRX.
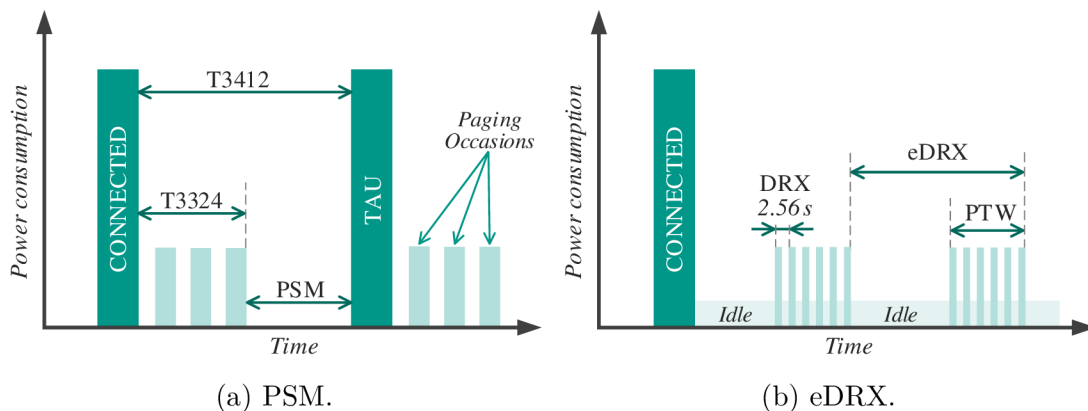
Fig. 2.3: Power saving mechanisms in 3GPP Release 13 [70].

With the following release, 3GPP introduced a new method of power conservation, called Extended Discontinuous Reception (eDRX) [34]. This method is not as effective as the PSM but diminishes the problem of long unavailability during sleep mode. Basically, eDRX is an evolution of DRX used in legacy LTE networks. In DRX, the device only needs to listen for Paging-Radio Network Temporary Identifier (P-RNTI) codes in Physical Downlink Control Channel (PDCCH) at the prescribed paging intervals. If the paging is intended for the device, the UE starts with data reception. Otherwise, the module transit into idle mode until the next paging occasion. The maximum DRX interval is 2.56 s, as depicted in Fig. 2.3b. Nevertheless, eDRX allows UE to listen for the paging interval in a short Paging Transmission Window (PTW) interval followed by a more extended idle period. The eDRX duration ranges from 5.12 s up to 175 minutes with PTW between 1.28 and 20.48 s [56, 70]. However, 3GPP Release 13 did not bring only the eDRX but also a new LPWA technologies LTE Cat M1 and NB-IoT detailed in the following sections.

NB-IoT

Initially introduced in 3GPP Release 13, NB-IoT (LTE Cat NB1) represents a technological enabler of mMTC. Due to newly introduced narrowband channels, NB-IoT is not backward compatible with legacy LTE. Still, they can coexist in one system

as the majority of the numerology has been kept. Thanks to this fact, the implementation of NB-IoT to the legacy LTE often represents only a software update. Aside from the above described inband deployment, NB-IoT can also operate in the guard band of regular LTE channel or as a standalone technology, see Fig. 2.4. With the 180 kHz bandwidth, NB-IoT precisely fits in a one LTE Physical Resource Block (PRB). For standalone implementation in 200 kHz GSM channel, it means 10 kHz buffer on each channel side. To provide extended coverage of +20 dB (in comparison with LTE), NB-IoT heavily relies on message transmission repetitions. The Narrowband Physical Random Access Channel (NPRACH) preamble, as well as Narrowband Physical Uplink Channel (NPUSH) data, may benefit from up to 128 repeats. For the Narrowband Physical Downlink Shared Channel (NPDSCH) data, it is even 2048 repetitions [56, 59, 64].

(a) In-band.   (b) Guard-band.   (c) Standalone.
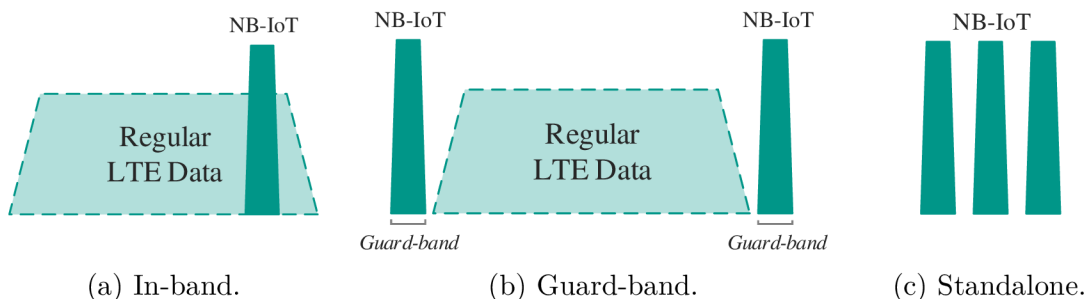
Fig. 2.4: NB-IoT deployment options [70].

Although NB-IoT reuses a significant part of LTE numerology, some parameters had to be trimmed to reduce modules' complexity. Thus, NB-IoT supports only Frequency Division Duplex (FDD) half-duplex mode with a single antenna port. In DL direction, NB-IoT relies on OFDMA with 15 kHz subcarrier spacing identical to LTE. Due to limited complexity, NB-IoT uses Tail-Biting Convolutional Code (TBCC) instead of turbo codes. The standard further defines only Quadrature Phase Shift Keying (QPSK) modulation to be used in DL with Transport Block Size (TBS) limited to 680 bits. It allows for the maximum data rate of approximately 26 kb/s. The UL channel provides more complexity as it supports both multi- and single-tone transmissions. Like in LTE, multi-tone transmission utilizes Singe Carrier Frequency Division Multiple Access (SC-FDMA) with 15 kHz subcarrier spacing. Multi-tone transmission can use 3, 6, or 12 QPSK modulated subcarriers reaching the maximum data rate of about 62 kb/s. However, single-tone transmission allows NB-IoT to utilize typical 15 kHz spacing and introduces a new 3.75 kHz variant. To reduce Peak-to-Average Power Ratio (PAPR), $\pi/2$-BPSK, and $\pi/4$-QPSK modulations with continuous phase are selected. The UL may also benefit from slightly larger TBS of 1000 bits compared to DL direction. Nevertheless, the maximum

message size in both directions is 1600 B, limited by the Packet Data Convergence Protocol (PDCP) Service Data Unit (SDU) [56,59,67].

Due to limited bandwidth, NB-IoT also introduced a new NPRACH with a maximum bandwidth of 45 kHz. Overall, the random access channel procedure is not much different from LTE, and it is based on the slotted ALOHA approach. The NPRACH uses a single-tone transmission with frequency hopping and 3.75 kHz spacing. The preamble contains four symbol groups made up of a Cyclic Prefix (CP) and four identical symbols. If needed, the groups can be repeated up to 128 times. NPRACH further supports two formats differing in CP length, limiting the maximum cell radius to 10 or 40 km [56].

As the utilization of a licensed spectrum does not impose strict requirements on maximum Equivalent Isotropically Radiated Power (EIRP) or Duty Cycle (DC) restriction, NB-IoT Release 13 defines two power classes of 23 and 20 dBm. Due to such high power values, the consumption during transmission may reach up to 300 mA. In reception mode, the consumption is around 46 mA with a more relaxed 6 mA in idle. Notably, these values do not allow for the promised 10-year battery life. To this aim, NB-IoT can utilize a combination of both PSM and eDRX modes, reaching the average consumption $<3\,\mu$A [56,71].

Even though NB-IoT in 3GPP Release 13 was a giant leap forward, some of the issues connected with mMTC persisted. These were resolved in following 3GPP Release 14, referred to as LTE Cat NB2. The most crucial change is associated with UE mobility. In 3GPP Release 13, the module can initiate reconnection procedure only in idle mode, which is ineffective in radio conditions with frequent handovers. The 3GPP Release 14 address this shortcoming by allowing reconnection during active RRC session. LTE Cat NB2 further supports Observed Time Difference Of Arrival (OTDOA) and Enhanced Cell ID (E-CID) positioning, new 14 dBm power class, multicast connections, and non-anchor carrier operation. Also, by allowing larger TBS of up to 2536 bits and increasing the number of Hybrid Automatic Repeat Request (HARQ), higher data rates were achieved. Namely, it is 127 kb/s and 159 kb/s for DL and UL, respectively [57].

In the 3GPP Release 15, the NB-IoT functionality was further extended with the local Radio resource management (RRM) policy. It allows Mobility Management Entity (MME) to store information about the UE and its traffic profile, which can improve the scheduling. On top of that, also the wake-up signals and Early Data Transmission (EDT) are available. The wake-up signal informs the device if it is necessary to monitor Narrowband physical downlink control channel (NPDCCH) for paging when the UE is in DRX or eDRX. With the early data transmission, the UE is able to convey the data in Msg3 of the random access procedure (carrying approximately 328 to 1000 bits). This release further reduces system acquisition

time using E-UTRA Absolute Radio Frequency Channel Number (EARFCN) pre-provisioning. With the introduction of a new NPRACH format, the cell radius is extended up to 100 km. However, also the small-cells (micro, pico, and femto) are supported in 3GPP Release 15 [57].

LTE-Cat M

This technology introduced in 3GPP Release 13 is designed explicitly as an 3GPP enabler for applications requiring long battery life, advanced services, and higher data throughput. LTE Cat M1 is fully compatible with legacy LTE systems by sharing its numerology, i.e., channel raster, subcarrier spacing, CP length, and frames structure. Thus, the LTE Cat M1 is intended for inband deployment. In comparison with NB-IoT, both full- and half-duplex modes, mobility (limited-to-full), Time-Division Duplexing (TDD), FDD, and Voice over LTE (VoLTE) are supported natively. The mMTC requirements are reflected in reduced bandwidth of 1.08 MHz (1.4 MHz, including guard bands), which equals the 6 PRB. It allows LTE Cat M1 in full-duplex mode to achieve data rates of up to 1 Mb/s (only about 300 kb/s in half-duplex). Similar to other LPWA technologies, the extended coverage is achieved mainly via repetitions. The mandatory Mode A with a limited number of repetitions (32 for Physical Uplink Shared Channel (PUSH), Physical Downlink Shared Channel (PDSCH), and Physical Random Access Channel (PRACH)) adds 10–12 dB to the link budget, resulting in the MCL of 155.7 dB. Also, only Mode A supports full mobility, voice services, 8 HARQ, and several transmission modes. Optional Mode B supports up to 2048 repetitions for both PUSH and PDSCH and 128 for PRACH. It allows LTE Cat M1 to add up to 20 dB to the link budget but radically increases the latency from milliseconds to seconds (up to 10 s) [56, 72, 73].

In order to provide extended battery life, LTE Cat M1 implements both PSM and eDRX. Also, two power classes with a maximum EIRP of 20 and 23 dBm are supported. Nevertheless, the most crucial change is the replacement of the wideband Physical Downlink Control Channel (PDCCH) with a new narrowband MTC Physical Downlink Control Channel (MPDCCH) (covers only 6 PRB), which bears the Downlink Control Information (DCI). The primary purpose of this channel is to schedule uplink and downlink grants and random access procedures [56].

The DL direction of LTE Cat M1 relies on OFDMA with 15 kHz subcarrier spacing, and as in the case of LTE, turbo codes are used. The messages with a maximum TBS of 1000 bits may be 16QAM, or QPSK modulated. For the UL direction, the limitation of TBS and available modulations are identical. However, UL direction multiplexing is based on SC-FDMA to lower a PAPR and reduce intersymbol interferences [56, 73].

With the rapid growth of high demanding mMTC scenarios, there was a chance that LTE Cat M1 will not be sufficient for such devices. Therefore 3GPP Release 14 addressed these issues and, on top of that, introduced a new category of UE called LTE Cat M2. Due to an extended bandwidth of 5 MHz, the maximum data rates increased to 7 and 4 Mb/s for UL and DL, respectively. The higher data rates are also available for LTE Cat M1 devices via the increased TBS size; the new maximum for UL direction is 2984 bits. For LTE Cat M2 devices, it is 4008 bits in DL and 6968 bits for UL. Further, the number of HARQ processes was increased to 10, enabling HARQ acknowledgment bundling. In order to allow more efficient use of subframes, also new repetition factors were introduced. Similar to NB-IoT, E-CID and OTDOA positioning together with multicast transmissions are available in Release 14 [58].

The 3GPP Release 15 further improves energy efficiency by defining 14 dBm power class and wake-up signals. By introducing EDT, the UE can transmit data during the random access procedure (up to 1000 bits) without the need to continue to the connected state. The acquisition time can be further reduced using EARFCN pre-provisioning, resynchronization signal, and improved System Information Block (SIB)/MIB demodulation. This release additionally supports the flexible starting PRB, Channel Quality Indicator (CQI) table with a broad range, 64QAM in DL, and $\pi/2$-BPSK in UL to increase spectral efficiency [58].

2.2.3   Non-3GPP LPWA Technologies

Non-3GPP LPWA technologies initiated the trend of modern M2M communication. More precisely, it was the main interest of the French company Sigfox, which started in 2009. Further, in 2012 they also launched the first commercial LPWA network [15]. At that time, radio technology was finally becoming less expensive, and integration applications were becoming easy to use. In order to decrease the initial cost, non-3GPP technologies mostly operate in license-exempt bands. It brings advantages of free radio resources at the expense of restricted DC, limited transmission power, and a higher chance of interferences [13, 66]. However, all the technologies are aware of this and can still provide adequate services for M2M devices.

Sigfox

It represents an LPWA technology operating in ISM frequency bands ranging from 862 to 928 MHz. The used frequency band is dependent on the currently selected Radio Configuration (RC); this also covers output power, spectrum access mechanism, throughput, and coexistence with other technology. Sigfox network has a star or star-of-stars topology consisting of EDs, at least one Gateway (GW), and

the cloud core. The ED data are wirelessly transferred towards the GWs and then forwarded to the cloud via an Internet connection. Notably, only the ED can initiate the communication at any time instance using an ALOHA-like channel access mechanism, not violating the limitations of radio channels imposed by the regulatory bodies and network operators. These regulations restrict the maximum payload size in UL direction to 12 B. The UL messages are Differential Binary Phase Shift Keying (DBPSK) modulated and conveyed at the rate of 100 b/s (RC 1, 3, 5, 6, and 7) or 600 b/s (RC 2, 4). For the first group, it represents Time on Air (ToA) from 1.12 to 2.08 s based on the payload size. The regulation in RC1 and RC7 further limits the DC to 1 % (36 s) per hour period. It practically limits the transmission to 6 messages per hour, i.e., 140 messages in 24 hours. In RC3 and RC5, the Listen Before Talk (LBT) technique is used. Before the communication, the device must verify that the whole 200 kHz channel is free of any signals stronger than -80 dBm. Due to more stringent regulations in both Americas, Australia, and some Pacific-Asia regions, the RC2 and RC4 use frequency hopping by repeating the message three times on different frequencies. The maximum ToA is limited to 400 ms on each channel with no new emission before 20 s. For the 600 b/s data rate, the actual ToA value ranges between 187 and 347 ms with repetitions inter-packet delay of 6.7 ms up to 2 s. In the case of the remaining RCs, the ED can send the packet only once in single-frame repetition mode or with multiple repetitions in multi-frame mode. The repetitions delay ranges from 40 ms to 2 s [15, 59, 60].

Each RC in Sigfox further defines four power classes 0u–3u based on the maximum EIRP. The highest power class 0u recommends a maximum limit of 24 dBm (RC 2, 4), 16 dBm (RC 1, 3, 6, 7), and 14 dBm (RC5). On the contrary, the lowest power class 3u, defines the power limits below 10 dBm (RC5), 2 dBm (RC 1, 3, 6, 7), and 0 dBm (RC 2, 4). Since mMTC heavily relies on UL data transfer, bi-directional communication is an optional feature in Sigfox networks. Bi-directional "B-procedure" (contrast to "U-Procedure") transmission is selected on a per-message basis by setting a special flag in the UL frame header. When B-procedure is active, 20 s (19 s for RC 3 and 5) after the first UL packet, the ED opens a receiver window for 25 s (33.5 s for RC 3 and 5). Upon successful reception of the DL packet, the ED must confirm the reception by transmitting the control DL message. The UL transmission of service message needs to start within 1.4 to 4 s after the DL message reception. This message carries the essential service information, including the battery level and Received Signal Strength Indicator (RSSI) of the DL message. All DL transmissions rely on GFSK modulation with a 600 b/s data rate. In comparison with UL transfers, the DL regulations are more pronounced with a maximum payload size of 8 B and four messages per day. However, DL may benefit from an increased maximum EIRP of 27 dBm [15, 60].

LoRaWAN

It is the next representative of LPWA technologies operating in the ISM spectrum from 433 up to 915 MHz. However, the most commonly used bands are 868 MHz in Europe and 915 MHz in the United States, Australia, and Asia. Like other non-3GPP LPWA technologies, LoRaWAN networks have a star or star-of-stars topology consisting of three different types of devices. Namely EDs, at least one GW, and a network server. On top of that, these devices can be complemented with a network join server to handle and coordinate devices inter-network roaming. In most cases, communication is initiated by ED using ALOHA-based channel access mechanism.

The physical layer of the LoRaWAN standard builds upon proprietary Long Range (LoRa) modulation developed by Semtech, whereas the MAC layer represents an open standard. It brings the significant advantage of creating private networks next to the operator-deployed public ones. The LoRa modulation is based on Chirp Spread Spectrum (CSS) modulation and provides substantial flexibility in terms of data rates, robustness, and bandwidth. The modulation speed can be controlled by Spreading Factor (SF), which can take up to six different values ranging from SF7 to SF12. With each increase of SF by one, the packet ToA rises 1.5 up to 2 times while increasing the link budget by 1.5-2 dB. To provide the most extended battery life possible, the ED is typically configured to use the lowest SF ensuring reliable communication. Selected SF can be set manually, or an Adaptive Data Rate (ADR) mechanism can be used [59, 61, 62].

Within the European frequency band, LoRaWAN supports a maximum of 16 channels. Each channel supports all SFs values from SF7 to SF12 with a bandwidth of 125 kHz. On top of that, LoRaWAN defines a single high data rate channel with SF7 and bandwidth of 250 kHz. This numerology results in the physical data rate ranging from 0.25 to 11 kb/s. The 868 MHz ISM band regulation further defines a maximum EIRP of 14 dBm and 1 % DC. Hence, the selected Data Rate (DR) limits the maximum payload that ranges from 51 B (SF12) to 242 B (SF7).

In the 915 MHz frequency band, the situation is more complicated. The first 64 channels are defined as 125 kHz ones supporting SF7 up to SF10, using a 4/5 Coding Rate (CR). Next, additional 8 slots utilizing 500 kHz bandwidth at SF8 are delineated in UL direction. The standard also defines 8 DL channels with 500 kHz bandwidth at SF7 to SF11. This numerology allows overcoming the limitation of 400 ms ToA by employing at least 50 channels, each occupying less than 250 kHz with the power level not greater than 30 dBm. For the 500 kHz channels, the Power Spectral Density (PSD) can not be higher than 8 dB per 3 kHz of spectrum. In practice, it limits the ED output power to 26 dBm. Based on the allowed transmission time, the maxim payload size varies from 11 to 242 B, with data rates between 0.98

and 21.9 kb/s [59, 61].

To enable DL transmission, ED opens one or two Receive Window (RW)s at specific timeslots (usually after 1 and 2 s) following each UL data transfer. The RW1 is opened in the same frequency channel and usually uses the same SF utilized for UL. When no data was received in RW1, the ED should open another RW (RW2) using a pre-specified channel and SF. The RWs can be used to deliver UL acknowledgments, carry user payload, or control commands. The above-described behavior defines A class device. On top of that, the ED may periodically open another RWs (class B) or spend the whole idle time in reception mode (class C) [61, 62].

2.3   Emerging multi-RAT Use Cases and Applications

Despite the immense advancement in mMTC and the coming of LPWA technologies, there will never be a silver bullet solution that fits all scenarios. In that respect combination of multiple radio technologies into a single device presents a viable solution. This solution already found its place in human-type terminals such as laptops, smartphones, and tablets, enabling nearly ubiquitous connection. Naturally, multi-Radio Access Technology (RAT) has its drawbacks, including increased complexity, higher price, and power consumption. However, due to the progression in lithography and other chips manufacturing processes, radio modules' costs are rapidly dropping. Thus the prevailing limitation is mostly the increased consumption. But with modern machine learning and optimizing algorithms, even this can be mitigated [74–76].

2.3.1   Smart City

The smart city scenarios are currently representing the most challenging tasks for mMTC. No other system puts such different requirements on the heterogeneity of the network deployments. The needs of various smart city applications tremendously differ in throughput, latency requirements, coverage, and battery life. Logically, the low power technologies suitable for sensor networks can not handle the needs of Augmented Reality (AR) and Virtual Reality (VR) applications. Thus the multi-RAT deployment can serve as an enabler for these heterogeneous applications. The smart sensor periodically reporting the environmental conditions may be equipped with a second interface allowing to transmit the video transmission in unexpected events such as fire or car crash. Also, cell-free and cooperative multi-cell solutions are highly discussed in smart city scenarios. The traditional cellular networks are not capable of handling ultra-dense deployments, including millions of connected

devices. However, in this concept, the multi-RAT equipped devices utilizing high-rate and low-rate backhaul links will appear as cell-free distributed systems. It allows for achieving a significant performance gain compared to traditional mobile networks [2, 77–79].

2.3.2   Smart Transportation

It is clear that smart transportation and V2X communication will be a strongly heterogeneous system with many different communication technologies, see Fig. 2.5. Very likely, there will not be a single universal technology providing universal communication channel. Inter-vehicles communication requires the lowest latency possible as the cars may move at high speeds, and even the small delay makes a significant difference in distance. This is crucial, especially for autonomous/self-driving vehicles, where mutual coordination without latency is vital. On the other hand, communication with infrastructure has far inferior requirements on both latency and data throughput. Combined, this represents the optimal use-case for a multi-RAT solution. On a highway, the vehicle will use a low-latency connection to communicate with other cars. However, it can send service reports to the owner via a long-range interface with undefined delays when parked [80–82].
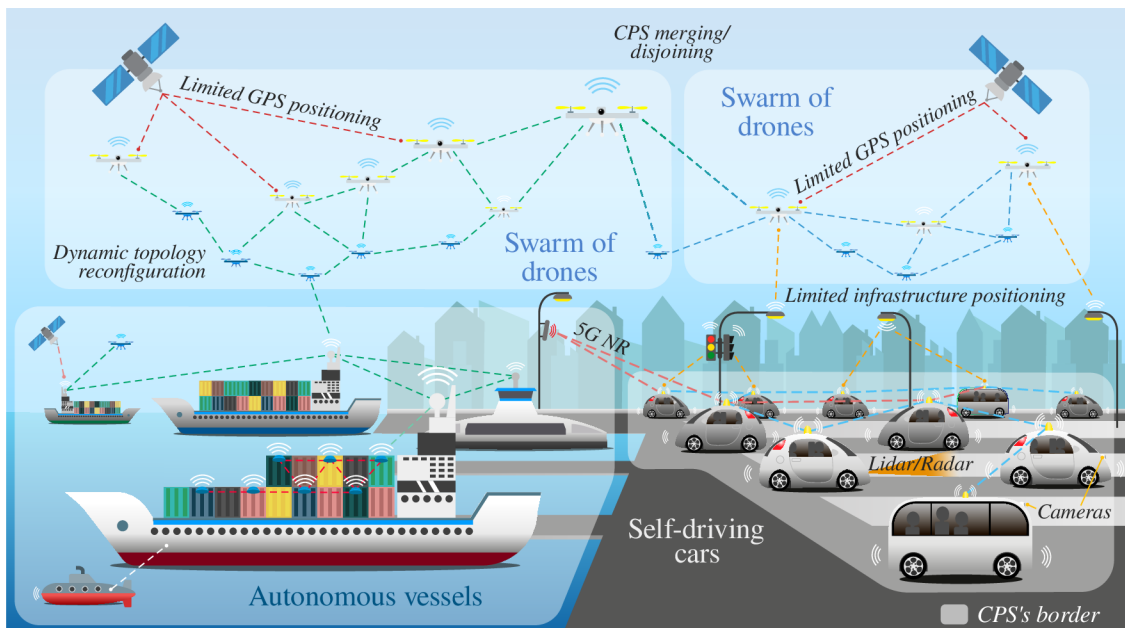
Fig. 2.5: Example of multi-RAT connectivity scenario.

2.3.3 Tracking/Logistic

Currently, inter-modal containers represent the most common way of shipping products around the globe. However, no single-hop RAT can provide reliable and cost-effective communication during the whole shipping process. Albeit satellite communication provides nearly ubiquitous coverage, it is still a costly service. Moreover, the satellite connection inside a warehouse or cargo hold represents a challenging task. The most common cellular networks are not omnipresent, and their offshore coverage is sparse and does not exceed a few kilometers. The technologies operating in the ISM band represent a low-cost solution but suffer from fragmented coverage and lack of spectrum harmonization. With a multi-RAT solution, the containers can convey their data via a private infrastructure when available. While traveling by land, the devices monitor surroundings networks and automatically selecting among them. At the open sea, ships' onboard private infrastructure ensures communication services and further uses a satellite link to send aggregated/compressed data. In the case of coast proximity, the ships' coverage can be extended by utilizing Unmanned Aerial Vehicle (UAV) as repeater/switch, see Fig. 2.5. In summary, multi-RAT improves connectivity, reduces outages, and provides augmented reliability. It also allows for reducing data delivery latency by avoiding retransmissions [75, 80, 83].

2.3.4 Smart Metering

The smart metering usually represents a delay-tolerant system with low requirements on the transmission latency. However, in unexpected events such as alarms, tampering, or unauthorized access, it is necessary to deliver this information in a delay-critical manner. Such a case represents the optimal use of a multi-RAT solution. In the standard situations, the data are transferred via a low-performance interface, whereas the alarm events use a more powerful one. The second interface can further serve for firmware upgrades. For the low-performance interface, the firmware package may require division into several smaller chunks transferred in several batches. On the receiver side, the individual parts must be merged, and the integrity verified. However, the more powerful interface can download the firmware as a single file, omitting the merging process. As a result, the multi-RAT solution allows accelerating the firmware upgrade, which is a crucial task as it may contain a fix for security vulnerabilities. Indirectly, it can also increase battery life as one message via high-performance technology may result in lower power consumption than several transmission of low-power communication technology [75, 83, 84].

2.3.5 Wearables and eHealth

In the area of wearables and eHealth, the benefit of multi-RAT is threefold. Firstly, the life-threatening events which are connected with unexpected changes in vital signs can be directly reported to the attending physician. For this purpose, the device uses low-latency communication, ensuring the fastest reaction. In the remaining time, the heartbeat status is transferred via a more power-efficient interface. The multi-RAT solution can also serve as an aggregation unit. Multiple on-body sensors equipped with different technologies communicate with the multi-RAT aggregation unit, which wraps the sensor data and transfers them to the cloud application. Thus the sensors may use only short-range communication technologies having reduced power consumption compared to long-range aggregation units. Finally, a combination of multiple technologies in multi-RAT solutions provides ultra-reliable communication [83, 85, 86].

3 LPWA Propagation Models

At this point, it is clear that mMTC will become a key player in the emerging 5G and beyond systems. Compared to H2H communication, mMTC services have drastically different design goals requiring a new approach to designing communication infrastructure. More specifically, mMTC involves deploying new radio access technologies referred to as LPWA, see Section 2.2. However, extended coverage for various indoor and outdoor applications together with capacity requirements, making the LPWA systems deployment a challenging task [59, 87]. Therefore, to accurately capture/predict the coverage and communication performance, the propagation models represent a vital tool for network planning (i.e., the location of both BSs and EDs). However, the abundance of such models differing in their structure, intended propagation environments, and other factors hampering the clear conclusion about their use for particular technologies. This fact has a vast impact specifically on the complex city-scale urban LPWA network deployments. With the ultimate goal of finding the best propagation model, this work covers the whole spectrum of primary sources, including standardization bodies, vendors/operators, and academia. The most commonly referenced models (in literature) are supposed to provide an accurate prediction in the whole LPWA technologies operating spectrum (predominantly sub-GHz) were selected from each group [59, 88–90].

Since the accuracy of empirical propagation models heavily depends on the propagation environment, this work aims to improve models' accuracy for LPWA deployments in urban city scenarios. First, the selected models are fine-tuned using the data from a large-scale measurement campaign from the city of Brno in the Czech Republic. Finally, these enhanced models' accuracy is cross-validated with the data from the second measurement campaign conducted in the Czech town Ostrava [59].

3.1 Models Requirements

Based on the way how the resulting path loss is derived, the propagation models can be divided into three main categories: (i) deterministic, (ii) stochastic, and (iii) empirical [91]. Deterministic models are the most precise but often require a 3D map of propagation environments and a lot of computing power. On the opposite side of computational demand lies stochastic models using a series of random variables to model the environment. Logically these models are the least accurate. Based on observations and measurements, empirical models lie between these two extremes providing a trade-off between accuracy and computational demands. Also, this works focuses solely on empirical models [59].

Notably, this work covers three well-known LPWA technologies: (i) Sigfox, (ii) LoRaWAN, and (iii) NB-IoT, occupying frequency bands ranging from 433 up to 2100 MHz. The lower bound of this range is delineated by LoRaWAN technology, whereas NB-IoT bounds the upper limit. Although NB-IoT supports frequency bands over 2 GHz, the real deployments usually use sub-GHz spectrum due to better signal propagation, which is the crucial requirement of LPWA networks. Therefore, selected models must provide accurate results in the whole operational spectrum of the LPWA technologies mentioned above. Considering the channel bandwidth, it has a particular impact on signal propagation similar to operational frequency. However, narrow bandwidth (< 200 kHz in most cases) of selected LPWA technologies compared to carrier frequencies usually leads to frequency flat-fading. For this reason, the channel bandwidth parameter can be omitted, and only the carrier frequency is considered [59, 87].

Aside from the frequency and channel bandwidth, also the physical layout of LPWA networks must be considered. Like most of the LPWA standards, selected technologies rely upon a star topology (in the case of Sigfox and LoRaWAN, star-of-stars) with the EDs directly communicating with the BS/eNodeB. In a typical deployment, the EDs are positioned slightly above the ground level, albeit below ground, or high-rise constructions/building deployments are also possible. Contrary, the BSs antennas are often located high above the ground to provide the most extensive communication range [59].

3.2 Selected Models

The analysis covered five extensively used propagation models from all three primary sources, summarized in Table 3.1. The 3GPP Urban and European Cooperation in Science and Technology (COST) 231 Walfish-Ikegami (WI) models represent the standardization group [92, 93]. Further, the Ericsson 9999 propagation model is an example of a vendor's group [94]. Finally, academia is represented by Okumura-Hata and Stanford University Interim (SUI) models [90, 91].

Tab. 3.1: Basic parameters of selected propagation models [59].

Model	Frequency	BS Ht.	ED Ht.	BS-ED Dist.
3GPP Urban	< 2600 MHz	0-50 m[*]	-	< 8 km
COST 231	150-2000 MHz	4-50 m	1-3 m	0.2-50 km
SUI	< 11000 MHz	15-40 m	2-10 m	< 10 km
Okumura-Hata	150-1900 MHz	30-200 m	1-10 m	1-20 km
Ericsson Urban	150-1900 MHz	20-200 m	1-5 m	0.2-100 km

[*] Above average rooftop level.

3.2.1 3GPP Macrocell

This propagation model is specifically designed for macro cells in urban and sub-urban areas outside the high-rise cores, with the buildings characterized by nearly uniform height. The resulting mean path loss is calculated as:

$$L = 40 \left(1 - 4 \cdot 10^{-3} h_b\right) \log_{10}(d) - 18 \log_{10}(h_b) + 21 \log_{10}(f) + 80, \qquad (3.1)$$

where d is the separation distance between BS and ED, f denotes carrier frequency in MHz, and h_b is the BS height above the average rooftop level. The h_b may range from 0 to 50 meters with BS-ED distance from a few hundred meters to kilometers. Unfortunately, the model is not particularly accurate for shorter distances ($< 200\,\mathrm{m}$) [59, 92].

3.2.2 COST 231 Walfish-Ikegami

This propagation model represents the joint effort of the COST association. At its core, the model combines the Walfish-Bertoni model and the final building path loss of the Ikegami model [95]. The model is intended for macro cells in urban and suburban environments. It can be used for carrier frequencies ranging from 800 up to 2000 MHz with a BS height interval from 4 to 50 m. On the other hand, the expected ED height is between 1 and 3 m. From the perspective of inter BS-ED distance, the model provides accurate results in a range from 0.2 to 50 km [59, 93]. Considering the Line-of-Sight (LoS) conditions, the mean path loss is calculated as:

$$L_0 = 32.4 + 20 \log_{10}(d) + 20 \log_{10}(f), \qquad (3.2)$$

where d is the distance between BS and ED, and f denotes the carrier frequency. For Non-Line-of-Sight (NLoS) propagation, the combination of free-space loss L_0, roof-to-street loss L_{rts}, and multiscreen diffraction loss L_{msd} connotes the resulting path loss. The basic propagation loss formula is given by:

$$L = \begin{cases} L_0 + L_{rts} + L_{msd}, & L_{rts} + L_{msd} > 0 \\ L_0, & L_{rts} + L_{msd} \leq 0 \end{cases}, \qquad (3.3)$$

where L_{rts} is calculated based on the Ikegami model as:

$$L_{rts} = -8.2 - 10 \log_{10}(w) + 10 \log_{10}(f) + 20 \log(\Delta h_m) + L_{ori}. \qquad (3.4)$$

Here, the Δh_m stands for the difference between average rooftop level h_r and height of mobile station antenna h_m. The remaining parameter w denotes street width, and

L_{ori} defines correlation factor accounting for loss due to street orientation angle φ:

$$L_{ori} = \begin{cases} -10 + 0.354\varphi, & 0° \leq \varphi < 35° \\ 2.5 + 0.075(\varphi - 35), & 35° \leq \varphi < 55° \\ 4.0 - 0.114(\varphi - 55), & 55° \leq \varphi \leq 90° \end{cases} \quad . \tag{3.5}$$

Further, the multiscreen diffraction loss L_{msd} is calculated as:

$$L_{msd} = L_{bsh} + k_a + k_d \log_{10}(d) + k_f \log_{10}(f) - 9 \log_{10}(b), \tag{3.6}$$

where b is the mean separation distance between buildings, and L_{bsh} value depends on the difference between BS height h_b and average rooftop level h_r:

$$L_{bsh} = \begin{cases} -18 \log_{10}(1 + \Delta h_b) & \text{for} \quad h_b > h_r \\ 0 & \text{for} \quad h_b \leq h_r \end{cases} \quad . \tag{3.7}$$

Finally, the coefficients k_a, k_d, and k_f are defined as follows:

$$k_a = \begin{cases} 54, & h_b > h_r \\ 54 - 0.8\Delta h_b, & h_b \leq h_r,\ d \geq 0.5\,\text{km} \\ 54 - 0.8\Delta h_b \frac{d}{0.5}, & h_b \leq h_r,\ d < 0.5\,\text{km} \end{cases} \quad , \tag{3.8}$$

$$k_d = \begin{cases} 18, & h_b > h_r \\ 18 - 15\frac{\Delta h_b}{h_r}, & h_b \leq h_r \end{cases} \quad , \tag{3.9}$$

$$k_f = \begin{cases} -4 + 0.7\left(\frac{f}{925} - 1\right), & \text{Medium cities} \\ -4 + 1.5\left(\frac{f}{925} - 1\right), & \text{Metropolitan centers} \end{cases} \quad . \tag{3.10}$$

3.2.3   Stanford University Interim

Based on an extensive measurement campaign conducted at Stanford University, the SUI propagation model represents the extension of the Erceg model developed by the AT&T Wireless group [96]. The SUI model divides the propagation environment into three categories based on terrain morphology to calculate the mean path loss value. Category A displays the highest path loss values describing the hilly environment with high tree density. On the contrary, Category C predicts the lowest path loss referring to flat terrain with minimal tree density. However, Category B intended for the hilly environment with rare vegetation producing intermediate path loss levels has been selected for this work.

Considering SUI model operational conditions, it is suitable for cells with a diameter of up to 10 km and BS antenna heights ranging from 15 to 40 m. For the ED, the antenna can vary from 2 to 10 m [59, 91]. Finally, the path loss formula is defined as:

$$L = \begin{cases} 20 \log_{10}\left(\frac{4\pi d}{\lambda}\right) & \text{for} \quad d \leq d_0' \\ A + 10\gamma \log_{10}\left(\frac{d}{d_0}\right) & \text{for} \quad d > d_0' \\ +_\Delta L_{bf} +_\Delta L_{bh} \end{cases}, \tag{3.11}$$

where d is the distance separating BS and ED, whereas d_0 represents the reference distance of 100 m with corresponding path loss value A. The signal wavelength is defined as λ, and γ denotes the path loss exponent. Further, the remaining parameters ΔL_{bf} and ΔL_{bh} represent frequency and antenna correction factors, respectively. In the extended form, the SUI model modifies the antenna correction factor ΔL_{bh}. It results in the introduction of a new formula for the calculation of reference distance d_0. This new reference distance, denoted as d_0', is derived as:

$$d_0' = d_0 10^{-\left(\frac{\Delta L_{bf} + \Delta L_{bh}}{10\gamma}\right)}. \tag{3.12}$$

The remaining parameters of the extended model are calculated as follows:

$$A = 20 \log_{10}\left(\frac{4\pi d_0'}{\lambda}\right), \quad \gamma = a - bh_b + \frac{c}{h_b}. \tag{3.13}$$

Here, h_b represents BS height, and variables a, b, c stands for constants dependent on the terrain category depicted in Table 3.2.

Lastly, the correction factors for the antenna height $h \leq 3$ m are defined as follows:

$$_\Delta L_{bf} = 6 \log_{10}\left(\frac{f}{2000}\right), \quad _\Delta L_{bh} = -10 \log_{10}\left(\frac{h}{3}\right). \tag{3.14}$$

Tab. 3.2: SUI model parameters [59].

	Category A	Category B	Category C
a	4.6	4.0	3.6
b	0.0075	0.0065	0.005
c	12.6	17.1	20

3.2.4 Okumura-Hata

This propagation model belongs among the most well-known representatives of academic efforts in this area. It is based on the extensive measurement campaign carried out in Tokyo during the 1960s. The Okumura-Hata model can be used for carrier frequencies from 150 to 1500 MHz with the BS-ED separation distance ranging between 1 and 20 km. Further, the module provides accurate results for BS antenna height in the range from 30 to 200 m with ED elevation between 1 and 10 m [59, 90, 97]. The model gives the median value of the propagation loss expressed as:

$$L_b = 69.55 + 26.16 \log_{10}(f) - 13.82 \log_{10}(h_b) - \\ - a(h_m) + (44.9 - 6.55 \log_{10}(h_b)) \log_{10}(d_m), \tag{3.15}$$

where f denotes the carrier frequency, h_b references to BS height, h_r is ED antenna height, and d stands for the inter-transceivers distance. Lastly, $a(h_m)$ represents the ED antenna correction factor. In the case of large cities with carrier frequency $f > 200$ MHz is computed as:

$$a(h_m) = 3.2 \log_{10}(11.75 h_m)^2 - 4.79. \tag{3.16}$$

Based on the formula mentioned above, the resulting path loss for urban areas can be simplified to:

$$L = L_b - 4.78 \log_{10}(f)^2 + 18.33 \log_{10}(f) - 40.94. \tag{3.17}$$

3.2.5 Ericsson 9999

At its core, Ericsson 9999 represents an improvement of the Okumura-Hata propagation model with adjustments for different morphology types. It makes the model optimal for macro sites with a cell radius from 0.2 to 100 km. On top of that, the model provides accurate results for the frequencies from 150 MHz up to 2 GHz. Further, the BS antenna height may range from 20 to 200 m with ED antenna elevation between 1 and 5 m [59, 94]. The resulting path loss is calculated as:

$$L = a_0 + a_1 \log_{10}(d) + a_2 \log_{10}(h_b) + a_3 \log_{10}(h_b) \times \\ \times \log_{10}(d) - 3.2 \log_{10}(11.75 h_r)^2 + g(f), \tag{3.18}$$

where h_b is BS antenna height, h_r denotes ED antenna height, f stands for carrier frequency, and d represents the distance between BS and ED. The parameters a_0–a_3, see Table 3.3, are constants dependent on the selected propagation environment.

Lastly, the frequency correction factor $g(f)$ is calculated as:

$$g(f) = 44.49 \log_{10}(f) - 4.78 \log_{10}(f)^2. \tag{3.19}$$

Tab. 3.3: Ericsson 9999 model constants [59].

Environment	a0	a1	a2	a3
Urban	36.2	30.2	-12	0.1
Suburban	43.2	68.93	-12	0.1
Rural	45.95	100.6	-12	0.1

3.3 Propagation Models Discussion

Side-by-side comparison of all considered propagation models with identical input parameters reveals significant diversity between their results. The most remarkable differences can be seen at shorter distances, where the divergence between the most optimistic and pessimistic model reaches up to 35 dB, see Fig. 3.1. However, this difference gradually decreases with the distance. At the 4 km mark, the disparity drops down to only 22 dB [59].
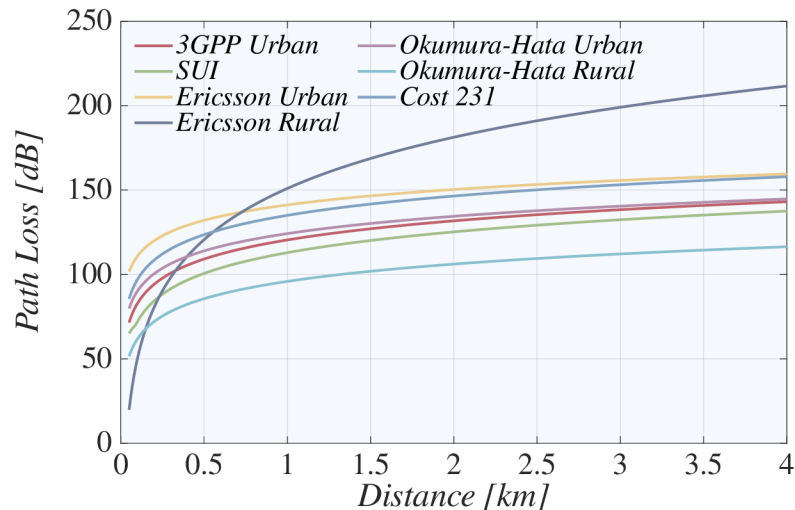

Fig. 3.1: Comparison of propagation models.

The results indicate that the SUI model provides the most optimistic path loss prediction. This is mainly caused by the selected terrain morphology type, as the category B is intended for suburban areas. Further, it is worth noting that the SUI model predictions follow the free space model characteristics up to a distance

of 0.09 km (d_0). However, this finding is not surprising as it is in line with the formula 3.11. Considering 3GPP and Okumura-Hata model, they perform comparably, especially for intermediate distances from 1 km. Nevertheless, on greater distances, the 3GPP model tends to predict more pessimistic values, i.e., higher path loss. For the COST 231 Walfish-Ikegami (WI) model, the additional losses due to building scattering can be seen [98]. It starts with the relatively optimistic predictions; however, the path loss value steeply rises even with the small distance increments. This behavior indicates dominant energy contribution over the rooftop diffraction, but it rapidly vanishes with increasing distance. As a result, the COST 231 WI model produces the steepest path loss curve. Finally, the most pessimistic predictions are present at the Ericsson Urban model. Nevertheless, these gloomy predictions are caused by high path loss at the initial point. Vice versa, the Ericsson Urban model curve rises least sharply [59].

It must be noted that all propagation models mentioned above are empirical, i.e., based on data from measurement campaigns. Empirical models are often tuned for a specific environment; thus, they might indicate inaccurate results in areas with different geographical locations or terrain morphology. It is the main reason why it is necessary to fine-tune the propagation models to achieve the most accurate results in specific environments. In what follows, the selected models are fine-tuned to data from Brno and cross-validated with measurement results from Ostrava [59].

3.4   Measurement Campaigns

The performed measurement campaigns included two mid-size cities in the Czech Republic, namely Brno and Ostrava. The test points wear spread throughout the cities and co-allocated with public transportation stop points. The first campaign conducted in the city of Brno covered over 300 unique test points, as depicted in Fig. 3.2. In comparison, the validation campaign organized in Ostrava included only 34 exclusive places [59].

At each location, all available statistics from LPWA modules were acquired. For Sigfox and LoRaWAN, the signal levels were reported only in the form of RSSI. Therefore, only this parameter can be used as the coverage quality indicator. NB-IoT, on the other hand, provides a variety of signal parameters, including RSSI but also Reference Signal Receive Power (RSRP). This work focuses on the latter mentioned RSRP, as it gives more accurate signal power estimation by excluding interference from other antenna sectors and synchronization channels [59].

(a) NB-IoT.
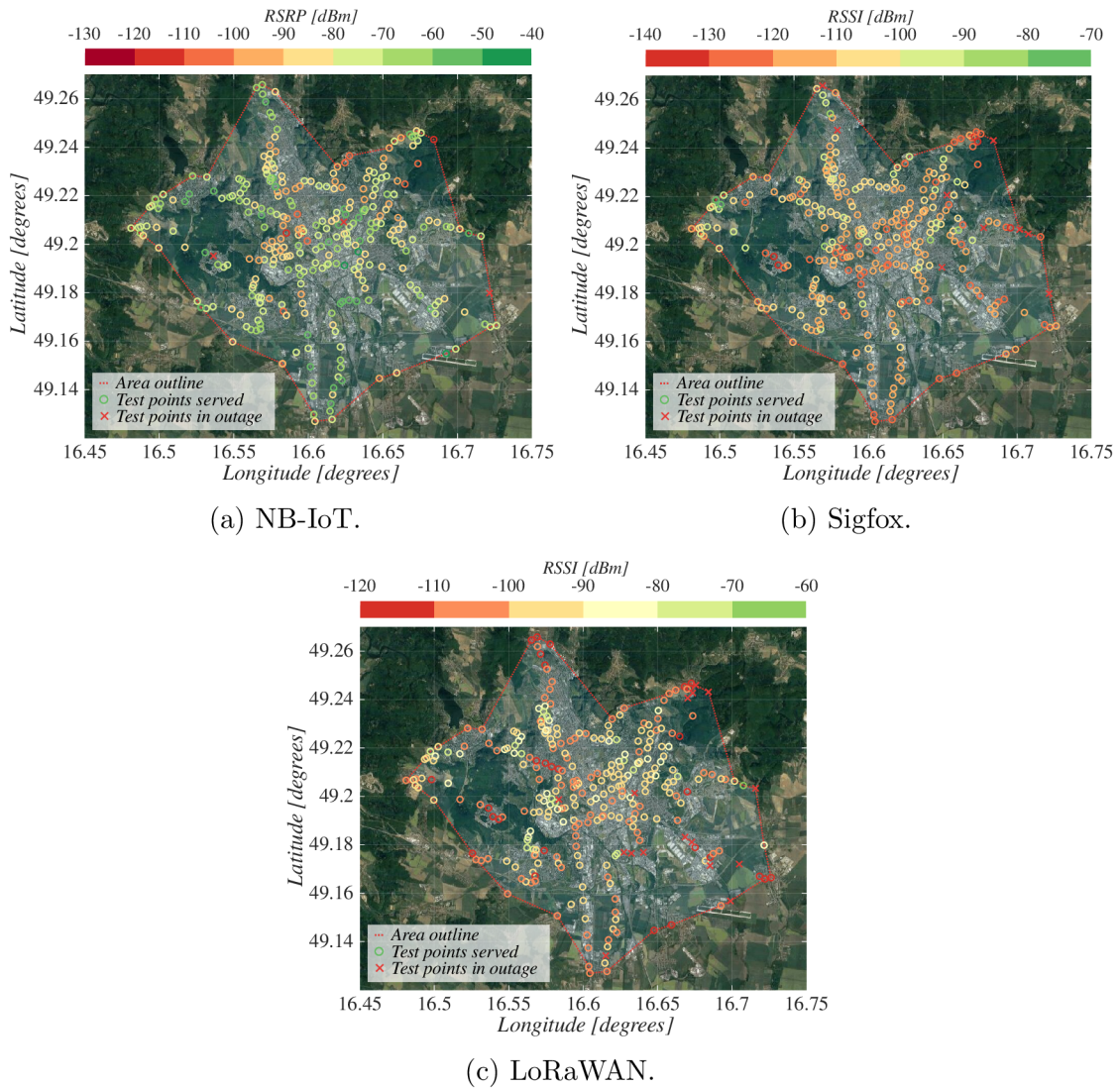
(b) Sigfox.

(c) LoRaWAN.

Fig. 3.2: Coverage by LPWA technologies in the city of Brno [59].

3.4.1 Measurement Equipment and Setup

For Sigfox and LoRaWAN coverage assessment, two commercial field network testers from the Adeunis company operating in an 868 MHz frequency band equipped with a 0 dBi omnidirectional antenna were used [99]. More precisely, the Sigfox tester designated as Adeunis ARF8121AA was set to utilize the maximum radiated power of 14 dBm (25 mW) to achieve the most extended communication range. In summary, it allowed achieving a sensitivity of up to -146 dBm with the standard SBS-T3 BS. In the case of LoRaWAN, the Adeunis ARF8123AA tester was used. The tester utilized the maximum radiated power of 14 dBm (25 mW) with the SF12 and CR set to 4/5 ensuring the sensitivity of -137 dBm. Even though this CR value did not provide the longest communication range, it was selected to satisfy the LoRaWAN specification requirements for the EU region [100]. However, the packet delivery

ratio should not be noticeably affected even with 4/5 CR as study [101] suggests. Contrary, the higher CR values such as 4/8 significantly increases the number of collisions. Based on the study conducted in [102], the difference may be as high as 20 %. For NB-IoT measurements, the testing device developed at Brno University of Technology (BUT) equipped with uBlox SARA N210 module was used [103]. The selected module supports only single-band operation in the 800 MHz (B20) spectrum with a maximum radiated power of 23 dBm (200 mW) and sensitivity of up to -135 dBm. Its output is further connected to the 2 dBi omnidirectional half-wave antenna. Specifically, it is a pentaband antenna by RF Solutions designated as ANT-PCB8121-FL [59].
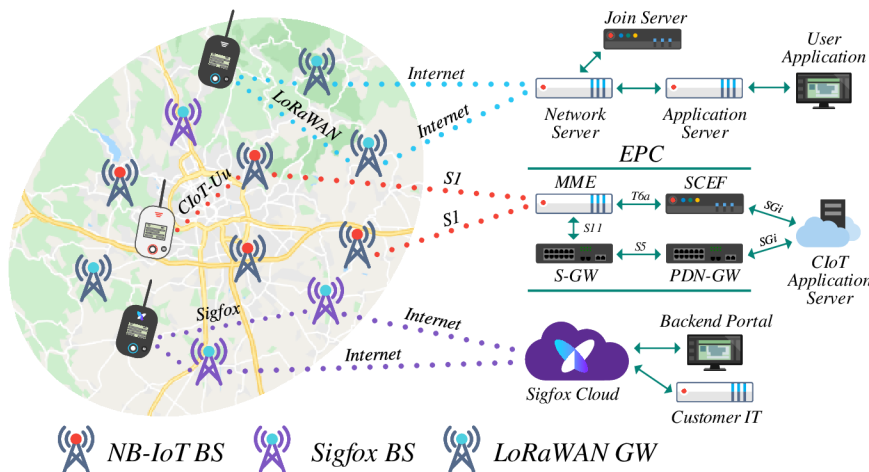
Fig. 3.3: Network architecture of considered LPWA technologies.

The actual measurements of all technologies in both cities followed the same pattern. The tester was transferred to the measured location and positioned approximately one meter above the ground level, apart from visible obstacles such as metal construction, high-rise buildings, and large trees. When the test devices started up, each of them transmitted 10 messages with 30 s period. It is worth mentioning that the testers were used sequentially to avoid interferences between LPWA technologies. Reflecting the limitation of Sigfox standard, the message size was limited to 12 B also for LoRaWAN and NB-IoT. The overall view on the measurement scenario and the path of each packet is depicted in Fig. 3.3. Once the measurements were finished, all available data were collected from the appropriate web management interfaces. Unfortunately, only the positions of LoRaWAN GWs are publicly available and accessible from the management interface. Therefore, it was necessary to enter into the non-disclosure agreement with network operators to acquire the locations of Sigfox and NB-IoT BSs. Thus, even though this information is known to the author, it can not be revealed publicly [59].

3.4.2 City-Scale Coverage

As mentioned several times, the measurement campaign included two mid-size cities situated in the Czech Republic. If geographical topology and urban development are considered, both cities share similar properties. Therefore, comparable signal propagation is also expected, which makes these cities perfect candidates for the independent cross-validation of the developed models [59].

Tab. 3.4: Parameters of the city coverage [59].

LPWA Technology	Avg. BS-ED distance [km][1]		Number of BS [-]		Avg. signal level [dBm]	
	Brno	*Ostrava*	*Brno*	*Ostrava*	*Brno*	*Ostrava*
NB-IoT	0.52	0.53	78	31	-76	-79
Sigfox	3.45	5.27	13	16	-112	-118
LoRaWAN	1.86	3.97	19	16	-98	-105

[1] It is considered the distance to the closest BS.

A side-by-side comparison of measurements in both cities reveals that the measurement campaign covered $150\,\text{km}^2$ in Brno and $140\,\text{km}^2$ in Ostrava, despite the tremendous difference in the number of measurements points. Brno's measurement campaign was more extensive, with 303 individual test points contrasting with only 34 locations in Ostrava. Due to the tremendous difference in the number of measurement points over the same area, it is expected that also the average distance to the closest BS is going to be influenced. Indeed, this difference is reflected in the average BS-ED distance for Sigfox and LoRaWAN; see Tab. 3.4. Naturally, the increased average length to the BS also influences the signal level. On the other hand, in the case of NB-IoT, only the number of utilized BS is affected. Ostrava's results include almost 50 % of BSs compared to the Brno data, with only one-tenth of the measurement points. For Sigfox and LoRaWAN, the difference is virtually negligible. The higher density of NB-IoT BSs and lower density of measurement points primarily causes this divergence as the ED connected to the unique BS at each testing point. For the competitors, with significantly less dense deployments, this fact has almost no effect on the number of used BS [59].

3.5 Evaluation of Propagation Models

This section introduces the steps needed for the derivation of the reference model, describes the proposed quantitative averaged metric, and discusses selected models'

accuracy. Further, the section reports on the propagation models' fine-tuning and cross-validation.

3.5.1 Methodology

The propagation models' fine-tuning from the acquired data sets from two cities can be divided into several steps. First, the reference models for each LPWA technology fitted to the measurement data are derived. To this aim, all available data from Brno's campaign are used. In the case of Sigfox and LoRaWAN technologies, it represents all packets received by reachable BSs, as multiple GWs can receive a single message. In the most extreme case, one message was received by 15 BSs. For NB-IoT, however, only the serving eNodeB can receive the data. Therefore, the input data set is smaller. Then, the accuracy of the verified models from Section 3.2 is compared to the fitted reference models, and those having the closest approximation are considered in the next steps. The selected propagation models are further fine-tuned to provide the highest accuracy for the fitted data by changing the floating intercept value. Finally, the tuned models' accuracy is cross-validated with results from Ostrava [59].

Reference Model Derivation

The measurement results represent a set of RSRP/RSSI samples, but the propagation models generally operate with path loss values. Hence, the conversion from the signal levels to path loss values is necessary. The respected path loss is derived as:

$$PL = SNR + P_{TX} + G - P_{RX}, \tag{3.20}$$

where SNR represents the signal-to-noise ratio, P_{RX} denotes the transmitter Effective Radiated Power (ERP), G stands for the sum of antennas gains, and P_{RX} is the value of received signal power (RSRP for NB-IoT, RSSI in the case of Sigfox and LoRaWAN). Then, the reference model for each LPWA technology is derived from the converted path loss data using the non-linear regression. This procedure's main output is the path loss exponent, later used as an input of the log-distance path loss model denoted by:

$$L = \overline{L}(d_0) + 10\gamma \log_{10}\left(\frac{d}{d_0}\right). \tag{3.21}$$

In this formula, $\overline{L}(d_0)$ represents the path loss value in the reference distance $d_0 = 0.1\,\mathrm{km}$, also known as floating intercept [104]. The letter γ identifies the

path loss exponent, and d represents the distance between BS and ED. The floating intercept value $\overline{L}(d_0)$ is derived from the free-space path loss formula with an additional $10\,\mathrm{dB}$ attenuation reflecting the losses caused by the propagation in the urban environment [59].

Propagation Models Fitting

When the reference propagation model is derived, the procedure can continue with the fine-tuning of the verified models from Section 3.2. This step includes two main phases. First, visual estimation is used to tune the models. In other words, the floating intercept of the verified propagation model is moved to be as close to the reference model as possible (such a model is then called fine-tuned). Further, the newly introduced cumulative deviation formula gives the numerical representation of the fine-tuned model accuracy. To achieve the maximum precision, as a next step, the fine-tuned model floating intercept is moved by a difference Δ, and the quality factor is recomputed. When the resulting quality factor is smaller than the previous one, the whole process is repeated. This process continues until the lowest deviation value is found [59].

This work proposes to use Mean Absolut Error (MAE) metric specifying the cumulative deviation providing a quantitative comparison between any two models under consideration (reference and fine-tuned) defined as:

$$Q = \frac{1}{N} \sum_{i=1}^{N} \left| R_i^{(1)} - R_i^{(2)} \right|. \tag{3.22}$$

Here, $R_i^{(1)}$ and $R_i^{(2)}$ represent the sample values of fitted and verified models at precisely the same point. Finally, N denotes the overall number of measurement points. Note that the modulus is used to account for positive and negative deviations. The MAE metric is also independent of the number of measurement points N as it produces the absolute deviation from the actual coverage averaged over all considered points [59].

Voronoi Tessellation

Even though the MAE metric represents the straight forward method for comparing two propagation models, it also includes subtasks of the measurement points derivation. First, the BSs locations serve as an input of the Voronoi diagram. Notably, the Voronoi's main property is that it partitions the plane into regions containing one generating point (BS), and each point in a given area is closer to its generating point than to any other. The resulting tessellated area of each LPWA technology can be seen in Fig. 3.4. The results further illustrate the tremendous difference

in the BS deployment density. The most pronounced divergence is visible between NB-IoT and Sigfox. It must be noted that the use of Voronoi tessellation may cause some discrepancies which are not in line with actual network coverage topology. For example, the ED message does not always have to be received by the closest BS, or in the case of Sigfox and LoRaWAN, it can be perceived by multiple BSs. However, these minor discrepancies do not significantly influence the results, and the ease of implementation makes Voronoi an optimal solution for this work.

Finally, the measurement points' locations are acquired in the last step by dividing the tessellated area into a regular grid with 50 m resolution. Also, the measurement point's distance to its closest BS is used as the reference and fine-tuned propagation models input parameter [59].

(a) NB-IoT.

(b) Sigfox.

(c) LoRaWAN.
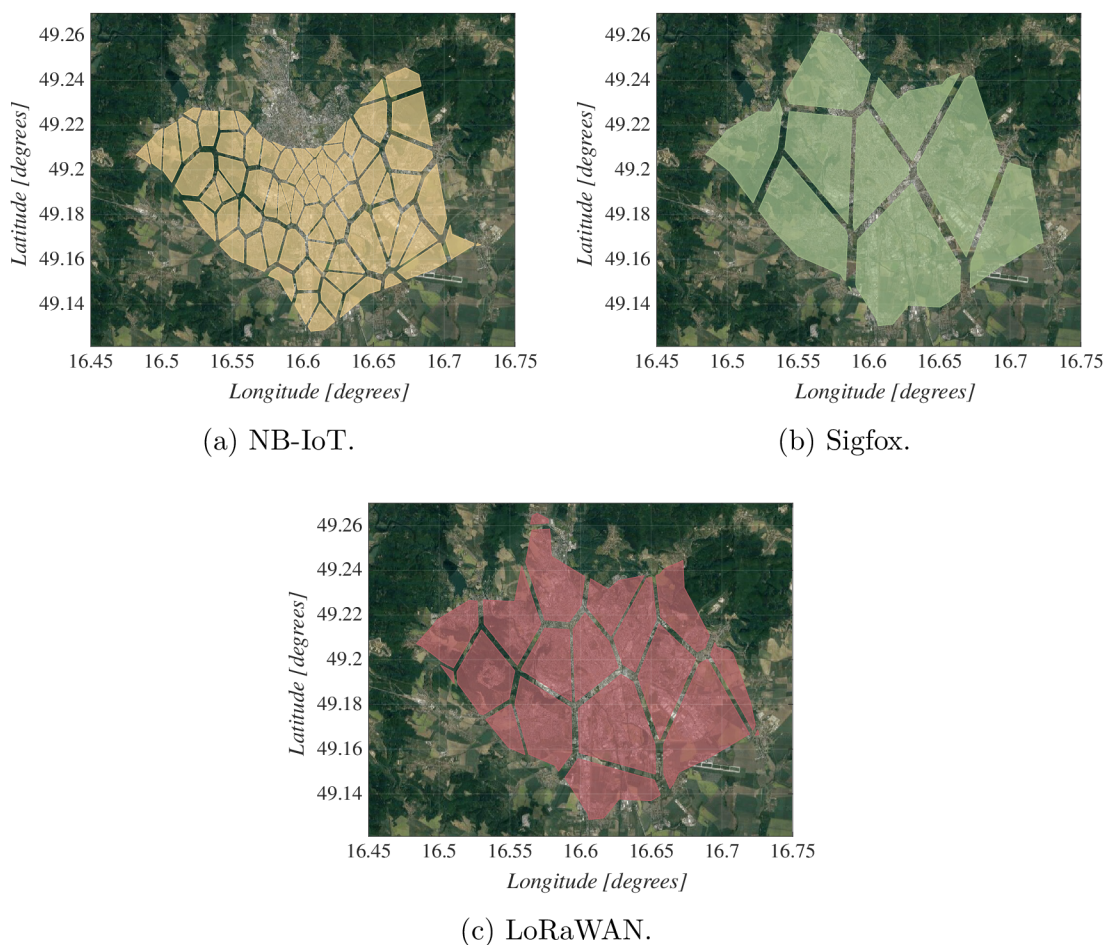
Fig. 3.4: Voronoi diagram of LPWA BSs in the city of Brno.

3.5.2 Models Fitting

The evaluation process can continue with the first two steps of the proposed methodology, i.e., selecting the most suitable propagation models and fine-tuning the models to Brno data.

To this aim, Fig. 3.5 displays the measurement samples acquired in Brno complemented by the verified propagation models from Section 3.2 together with the derived reference models. Based on the cursory visual analysis, it can be stated that 3GPP Urban, Okumura-Hata Urban, and SUI represent promising candidates for accurate approximation. The remaining COST 231 and Ericsson models significantly overestimate the path loss values. In order to certify the visual observation, quantitative MAE metric (3.22) is applied, giving the mean deviation between the reference models (fitted to measurement data) and the verified ones. The numerical results, depicted in Fig. 3.6, indeed match the visual observations. In its basic form, the SUI model provides the most accurate prediction for both NB-IoT and LoRaWAN technologies. In contrast, Sigfox is best characterized by the 3GPP Urban model. However, it is necessary to bear in mind that these results are gathered from the basic form models. Thus, the final results may differ [59].

(a) NB-IoT.

(b) Sigfox.

(c) LoRaWAN.
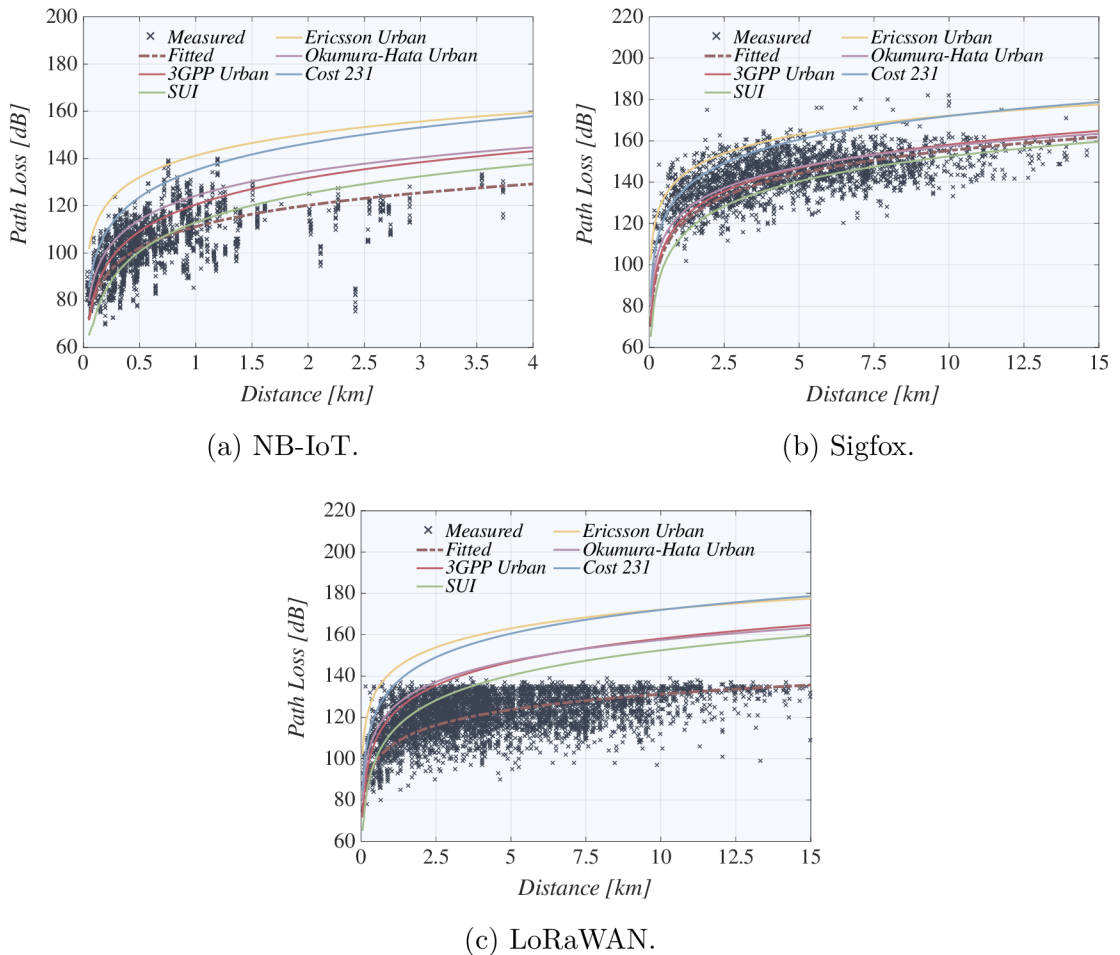
Fig. 3.5: Comparison of reference and standardized models in the city of Brno [59].

In the next step, the analysis continues by fine-tuning the verified propagation models. As a first step, the selected models are transformed into the generic
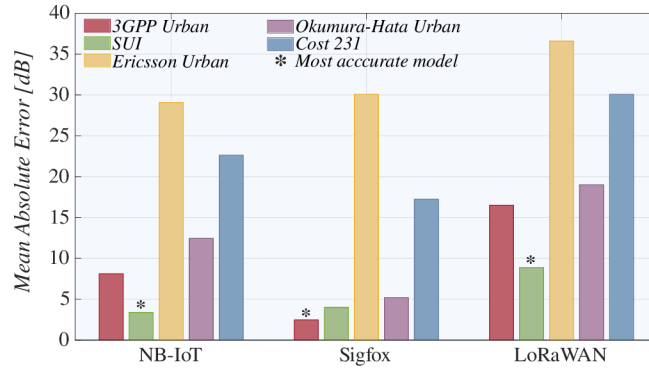
Fig. 3.6: Accuracy of verified models in the city of Brno [59].

(a) NB-IoT.

(b) Sigfox.

(c) LoRaWAN.
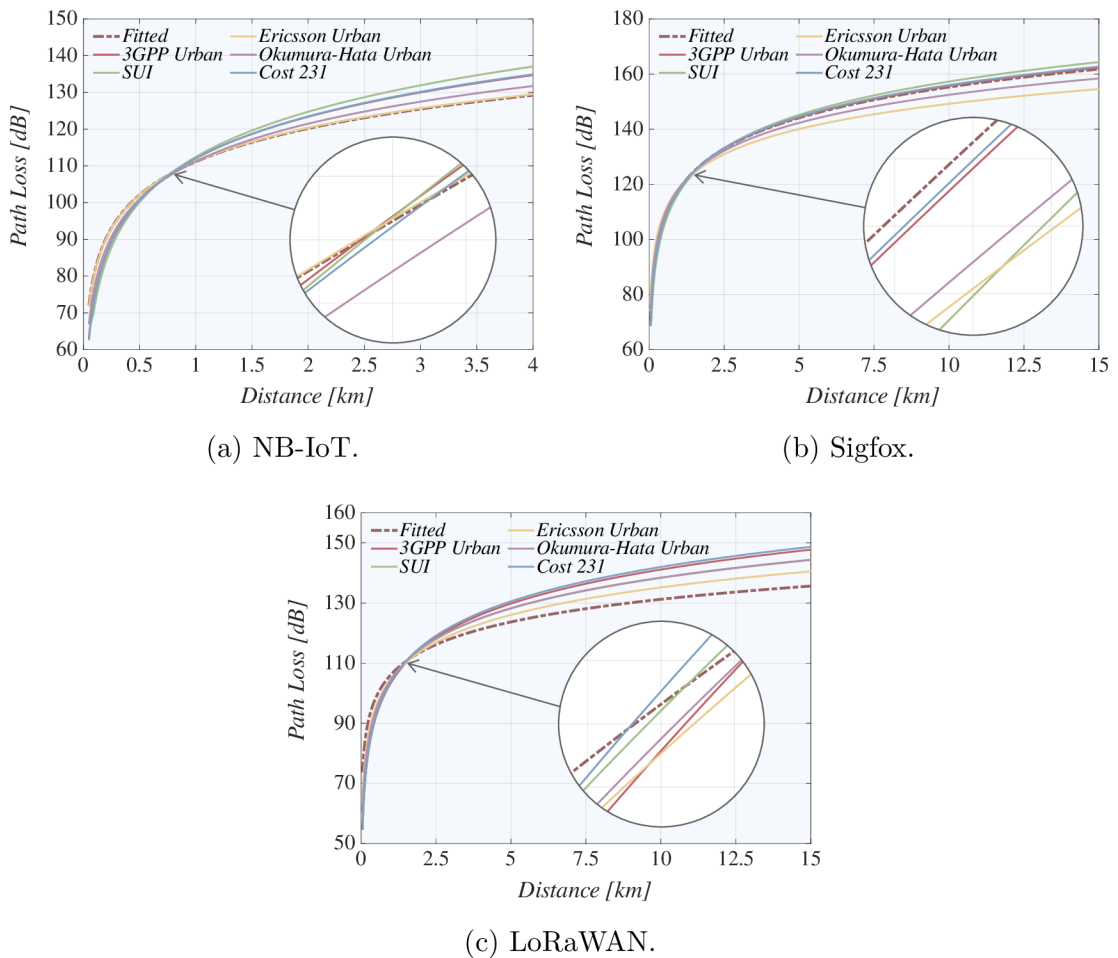
Fig. 3.7: Comparison of reference and fine-tuned models in the city of Brno [59].

log-distance path loss model (3.21), allowing for straightforward adjustment of the floating intercept value. The results of this fine-tuning operation are presented in Fig. 3.7. Visual analysis reveals that for NB-IoT and LoRaWAN technologies, the fitted models slightly deviate from the reference ones. This deviation tends to appear mainly for the more considerable BS-ED separation distances, i.e., larger than 1 km

for NB-IoT and 2.5 km for LoRaWAN. However, there is an exception of the Ericsson Urban model for NB-IoT that predicts accurate results for the whole considered BS-ED distances range. In the case of Sigfox, all 3GPP Urban, Okumura-Hata Urban, and COST 231 models provide impressive results, with the first-mentioned being the most accurate. Despite the visible divergence at the larger distances, the Ericsson Urban model captures the reference LoRaWAN model the best [59].

The fine-tuned models' accuracy is also assessed by employing the MAE integral metric, see Fig. 3.8. Indeed, the fine-tuned Ericsson Urban model drastically outperforms its competitors in the case of both NB-IoT and LoRaWAN technologies. Similarly, the 3GPP Urban model provides superior results for Sigfox technology. The exact parameters of the best performing models are highlighted in Tab. 3.5[1]. Side by side comparison of data in Fig. 3.6 and Fig. 3.8 also reveals that the fine-tuning shifted the Ericsson Urban from the least to the most accurate model considering NB-IoT and LoRaWAN. In terms of the actual numbers, it represents 400 and 36 times improvement for NB-IoT and LoRaWAN, respectively. For Sigfox, there is no such a bold change as the 3GPP Urban model provides the most accurate results in both cases; still, the fine-tuning procedure displays more than 20 fold precision improvement [59].

Tab. 3.5: Fine-tuned propagation models parameters [59].

Propagation Model	NB-IoT		Sigfox		LoraWAN	
	PL_{d0}	γ	PL_{d0}	γ	PL_{d0}	γ
3GPP	112.07	3.76	118.04	3.76	103.54	3.76
SUI	112.43	4.09	117.09	4.02	102.35	3.89
Ericsson	111.21	3.04	118.82	3.04	104.82	3.04
Okumura-Hata	111.22	3.41	118.33	3.38	104.69	3.33
COST 231	112.03	3.80	118.00	3.80	104.00	3.80

Finally, if the fine-tuned models' accuracy is compared to the best performing verified models (ones in the basic form), the fine-tuned models still clearly dominate. In the case of NB-IoT, the fine-tuned model provides 40 times improved accuracy over the best performing not-tuned one. For Sigfox and LoRaWAN, the change represents a 20 and 8 fold increase, respectively [59].

---

[1]For better traceability and repeatability, the fine-tuned models' underlying parameters are also listed. The parameters of the log-distance model represent the floating intercept PL_{d0} and path loss exponent γ.
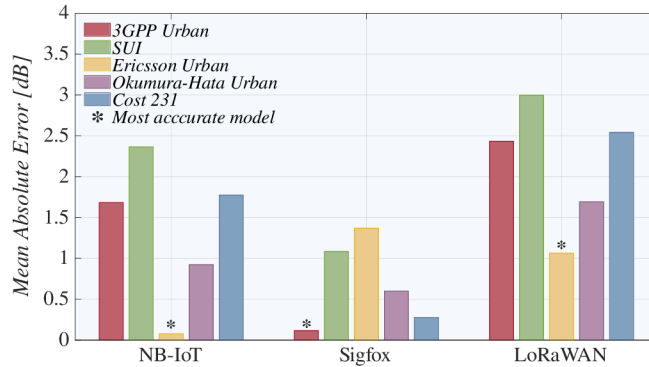
Fig. 3.8: Accuracy of fine-tuned models in the city of Brno [59].

3.5.3   Models Cross-Validation

The most crucial part of propagation model development is related to its applicability to other deployments. In this work, the accuracy of models fine-tuned on Brno data is verified using Ostrava's measurement results. As a first step of the cross-validation process, the Ostrava measurement results with the appropriate fitted reference model, as well as the Brno fine-tuned models are depicted in Fig. 3.9.

The cursory visual analysis shows that all the fine-tuned models (on Brno data) can potentially provide an accurate path loss approximation for Ostrava results. However, in the case of NB-IoT technology, the Ericsson Urban significantly outperforms the remaining competitors. For Sigfox and LoRaWAN, the fine-tuned models capture the path loss characteristics for shorter distances with substantially higher precision compared to more considerable BS-ED separation distances. In this regard, the Okumura-Hata Urban model provides the closest match for the Sigfox technology, faithfully capturing the path loss characteristics during the whole 15 km range. Unfortunately, in the case of LoRaWAN, all considered models indicate increased deviation. This divergence tends to grow with rising BS-ED separation distance. Nevertheless, among all models, Ericsson Urban catches the path loss characteristics the best [59].

In the next step, the fine-tuned models' accuracy with Ostrava data is numerically quantified by the MAE metric (3.22), see Fig. 3.10. Besides the Brno fine-tuned models, the figure also displays the best performing verified models in the raw form (i.e., not-tuned propagation models from Section 3.2). It is worth mentioning that for all selected LPWA technologies, the SUI model represents the most accurate verified model in the basic form. However, this finding is in line with the knowledge gained from Brno data, where the SUI model provides the best accuracy for NB-IoT and LoRaWAN and holds second place for Sigfox. The numerical analysis further verifies that, in general, the LoRaWAN approximation is less precise com-

55

(a) NB-IoT.

(b) Sigfox.

(c) LoRaWAN.
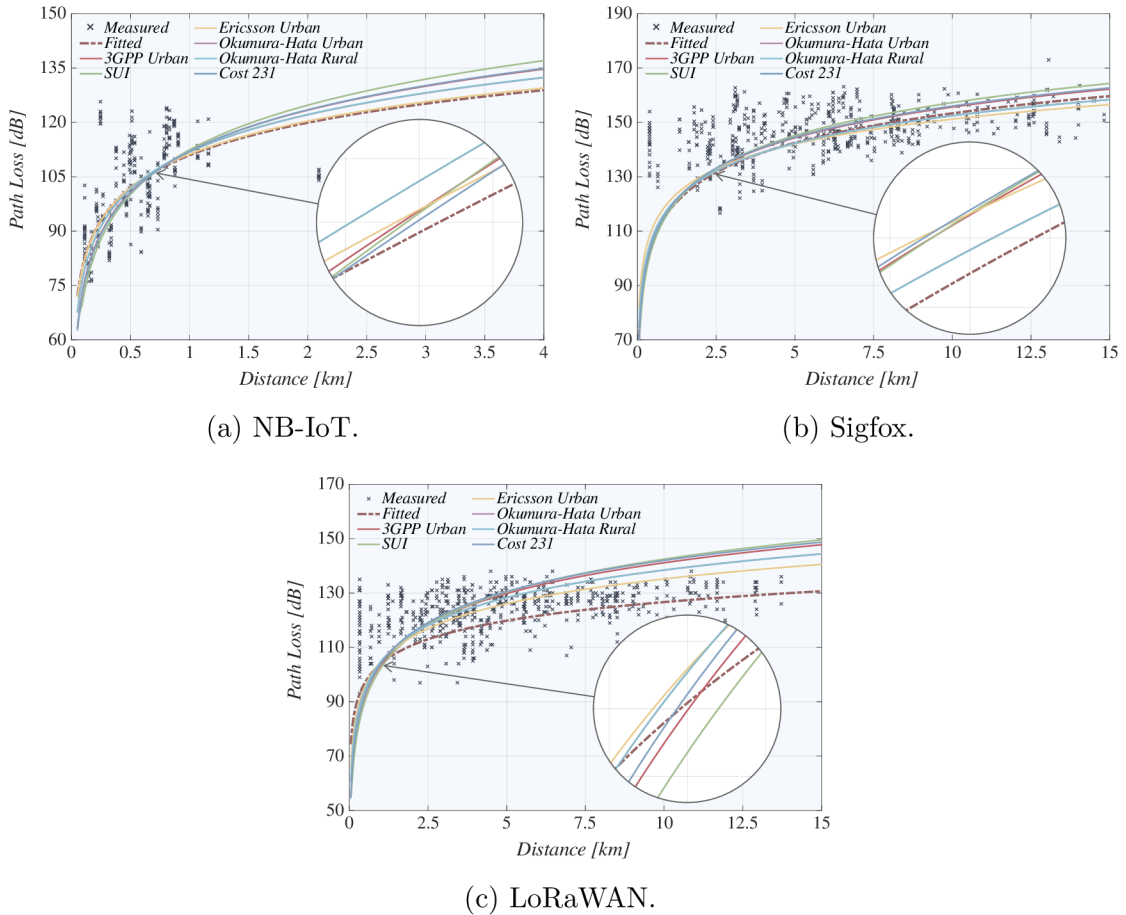
Fig. 3.9: Comparison of Ostrava reference model with Brno fine-tuned models [59].
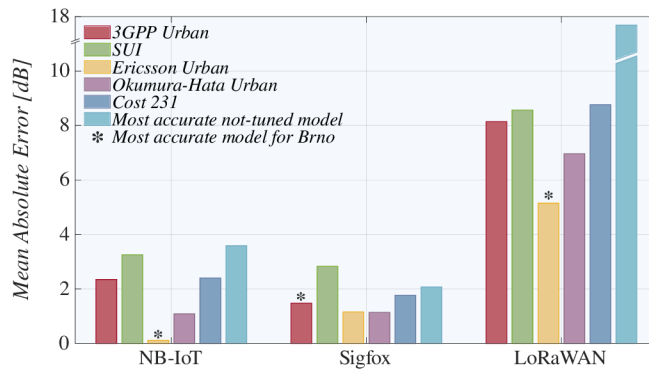
Fig. 3.10: Models cross-validation in the city of Ostrava [59].

pared to NB-IoT and Sigfox. For NB-IoT, even the worst-performing fine-tuned model provides more accurate results than the best performing verified model in the raw form. On top of that, the fine-tuned Ericsson Urban model (the most accurate one) displays a 30-fold accuracy increase over the best-performing model in the basic form. Unexpectedly, the most accurate fine-tuned model in Ostrava (Okumura-Hata

Urban) for Sigfox technology differs from Brno (3GPP Urban). Nevertheless, the difference is marginal with a value in the range of 0.3 dB (23 %). Still, the Brno fine-tuned models, except SUI, provide more precise predictions than the basic form verified model. Surprisingly, even with the increased inaccuracy of fine-tuned models for LoRaWAN technology, they still offer superior performance compared to the basic form verified model. Specifically, the most accurate fine-tuned model displays a 9 times lower approximation error than the best-performing verified model [59].

4 Coverage Assessment Planning

The deployment and maintenance of large-scale multi-BS wireless communication networks is a costly and extremely complex process requiring perfect knowledge of the propagation environment. To this aim, the network operators regularly conduct extensive measurement campaigns to create an accurate coverage map. However, the locations and the number of measurement points providing efficient and precise results are usually not known in advance. Therefore, this study proposes a new methodology for understanding the selection of measurement points balancing spent effort and achieved accuracy [105].

4.1 Background & Rationale

As mentioned before, the coverage assessment is a complex process that can be affected by various factors. These constraints may include non-technological aspects, including urban layout characteristics, legal issues, and the limited set of locations where the BS can be deployed. Usually, the decision on the BS location is made based upon three-dimensional city maps. This process may involve several iterations, where the measurement results are used to adjust the newly deployed BS locations. However, even after the deployment, network operators carry out regular inspections to understand whether the coverage characteristics and network performance change over time [105].

Dynamic fluctuations in the propagation environment over extended periods of time were also verified by related studies [106, 107]. One of the studies revealed that the variance could be as high as 40 dBm even for static deployments over the course of several-month period. It is worth noting that these changes are not utterly random, but they are represented by a small variation of samples oscillating around the mean value. However, these micro-scale fluctuations do not influence the overall propagation environment "picture" and are even smoothed by the propagation models, which predict the mean value. The rationale behind the more considerable changes is that the LPWA network operators may perform infrastructure updates or network reconfiguration. However, the propagation conditions may also change due to, e.g., seasonal changes or the build of a new construction intersecting the propagation path. Therefore, to maintain a relevant coverage map, the assessment must be conducted on a regular basis [105].

Usually, operators are willing to assess the network coverage at the highest number of locations possible (ideally in all areas), which is a time-consuming process. Notably, one of the most critical issues is selecting the optimal number of measurement points for accurate coverage assessment, as it is hard to determine in advance.

In practice, the decision is affected by multiple factors such as city deployment characteristics, selected technology, and carrier frequency. Moreover, this problem's complexity is even higher when the location of BSs is not known in advance, which may be the case of third-party companies aiming to assess the LPWA network coverage and signal quality [105].

4.2   Key Contribution

As its main output, this study proposes a new methodology of coverage assessment without the knowledge of BSs in LPWA networks. Specifically, the study addresses the signal quality estimation at points of interest in a specific area based on extensive measurement campaign results. Further, it provides a cumulative metric that quantifies how the number of measurement locations affects the assessment accuracy. In other words, how the selected interpolation algorithms perform under different thinning methods. Notably, the study considers three major LPWA technologies, namely, NB-IoT, Sigfox, and LoRaWAN. Further, the coverage assessment maps are created using five different interpolation methods, including Nearest-neighbor, Linear, Natural-neighbor, Inverse Distance Weighting (IDW), and Kriging. It is worth mentioning that the first thinning method is inherently random, whereas the second incorporates a more deterministic approach [105].

The primary outcomes of this work can be summarized as follows. In the first phase, the coverage map and reference model are derived using the measurement data and the knowledge of BSs locations. The reference model is not the main output of this work, but it is later used to compare the accuracy of the already available propagation models with the constructs produced by different interpolation algorithms. The study then proceeds by gradually reducing the number of generating (measurement) points via probabilistic and deterministic thinning. In combination with the interpolation method, these limited data sets are used to generate reduced coverage maps. Using the portion of the area covered with at least a signal level of (x dBm) and further employing the integral averaged metric, the assessment continues by comparing the reference model against the coverage maps produced utilizing the interpolations. Finally, the performance of the reference model and interpolation methods under thinning is compared with the actual measurement results. It allows assessing the accuracy of each considered approach in the most convenient manner. Using the proposed methodology, one can identify the number of measurement points required to produce a coverage assessment map with accuracy for a city environment similar to Brno [105].

4.3   Related Work

Large-scale measurement campaigns represent the most convenient tool for precise network coverage assessment. However, it is a challenging and complex task requiring a lot of effort and money. Therefore, by reducing the number of measurement points while adhering to a certain accuracy level, primary technological adopters can significantly reduce cost and time spent [105].

Unfortunately, the research question of assessing large-scale multi-BS LPWA networks without BSs location knowledge has not yet been sufficiently investigated. Therefore the following subsections are devoted to characterizing three main subtasks connected with this work. Subsection 4.3.1 features studies related to coverage assessment; then, state-of-the-art interpolation methods used for coverage estimation are overviewed in Subsection 4.3.2; finally, the Subsection 4.3.3 summarizes standard coverage metrics [105].

4.3.1   Coverage and Signal Quality Assessment

The coverage assessment of LPWA technologies with explicit knowledge of BSs locations was addressed in several research works. Mostly, standardized channel quality indicators such as RSRP, RSSI, or Signal to Interference plus Noise Ratio (SINR) are used to access the signal coverage/strength. Even though these indicators provide the most straight-forward signal strength/quality assessment, comparison between different works may be cumbersome [105].

The authors of the study [108] carried out an extensive measurement campaign focused on the coverage assessment of LPWA technologies LoRaWAN and Sigfox. The data acquired in the city of Antwerp in Belgium was used as an input for the developed localization framework. In terms of the number of BSs, Sigfox slightly exceeded LoRaWAN with 84 BSs distributed over an area of $52.97\,km^2$. The measurement campaign for Sigfox also included rural measurements between the cities Antwerp and Ghent. In total, the measurement campaign covered the area of $1068\,km^2$ served by 137 unique BSs. Unfortunately, this study does not provide any results from the NB-IoT measurement trial focused on the coverage and signal quality assessment [105].

In research [109], the authors characterized the distribution of LTE BSs in the city of Xian in northern China. The study captured real-world measurements offering the first-order look at the distribution and density of NB-IoT BSs. Though the campaign was focused only on LTE technology, it can also provide insight into the NB-IoT as they usually share network infrastructure. Concretely, in this urban scenario, the area of 3 km^2 was covered with 13 BSs. In terms of BSs density,

it is more than 4 BSs per km^2. Surprisingly, this value is almost identical to the NB-IoT measurement campaign results conducted by the author of this doctoral dissertation [105].

In some works, authors chose a different approach to this problem and used simulation tools to estimate the LPWA network coverage. The authors of the study [110] utilized real Telenor's cellular network structure to simulate the performance of three major LPWA technologies, namely NB-IoT, LoRaWAN, and Sigfox. Closer inspection of network infrastructure further showed that urban cells' density is five times higher in comparison with rural areas. The LPWA technologies also displayed their domination over the legacy GPRS technology in terms of the number of outages. The NB-IoT and Sigfox provided outages below 1 %, followed by LoRaWAN with 2 % messages loss. On the other hand, the legacy GPRS had the chance of message loss of around 8 % [105].

It must be noted that all studies mentioned above presume the full knowledge of BSs locations. Therefore, the operators can easily use the measurement results to assess and improve their network deployments. For third parties, however, this approach is not convenient as the locations of BSs are not publicly available [105].

4.3.2 Interpolation Methods

As it is nearly impossible to conduct a measurement campaign with an evenly spaced grid of testing point locations, the application of interpolation methods at the points where no data is readily available is needed. This principle of missing points approximation by applying interpolation methods was also discussed in several research studies. Notably, the authors of study [111] utilized IDW interpolation to predict LTE signal strength at the location with no measurement data available. However, the authors of this publication do not provide any assessment metric. It is the main reason why the accuracy of the results can not be verified since the predicted value is considered as "ground truth" [105].

To create a coverage map, authors in [112] employed Fixed Rank Kriging, predicting the signal levels in the region covered by a single BS. Interestingly, in terms of prediction accuracy, the Kriging interpolation surpassed even the derived propagation model. More precisely, the Root Mean Square Error (RMSE) of Fixed Rank Kriging (FRK) ranged between 3 and 5 dB. In the next research [109], the authors proposed a new coverage map construction method that uses Multi-Criteria Triangulation-induced Interpolation (MTI). However, it must be noted that this work focuses solely on predicting the covered area without closer specification of the expected signal levels. Finally, in [113], the authors proposed an RSS-based localization framework build upon interpolation and extrapolation methods to re-

construct signal fingerprints. Namely, the authors used Linear, Nearest-neighbor, and IDW interpolation schemes together with Minimum, Mean, Gradient, IDW, and Nearest-neighbor extrapolation. Among all of the selected interpolation methods, the Linear and IDW scheme provided the highest prediction accuracy, with the mean error ranging between 4.3 and 8 dB [105].

In summary, all research works mentioned above focus on signal levels prediction incorporating a single BS. Therefore, the results can not be directly compared with the results of this study, as the derivation of a multi-BS coverage map represents an incomparably more complex and challenging task [105].

4.3.3 Coverage Assessment Metrics

In order to have a convenient tool allowing for quantitative comparison of predicted values with the reference model, the coverage metric has to be defined. Generally, the quantitative metrics can be divided into two main groups, namely averaged and cumulative parameters. In the study [109], the authors used averaged assessment metric, defined as the ratio between misclassified regions to the total area. Such metric allows for a simple comparison of results using a single variable; however, it does not provide any measure for comparing signal levels accuracy. In practice, this metric focuses only on borders of the covered area, simplified to Boolean variable with true/false states [105].

The study [113] defined the cumulative assessment metric as the cumulative probability of RSS error. On top of that, the mean error as a function of removed fingerprints is used to initially verify the interpolated values. This mean error metric is similar to the approach used in this work but does not account for positive and negative deviations by using modulus. Further, in the study [112], the assessment metric is given as a Cumulative Distribution Function (CDF) of empirical errors between modeled and predicted values. Such a metric provides useful visual information about the distribution of the error in the area. Still, it does not allow for a simple comparison of deviations in the form of a single number [105].

Hence, this work combines two previous approaches from studies [112] and [113] with certain modifications. In contrast with the metric introduced in [112], this research utilizes a portion of the area covered with a signal level of at least x dBm. However, aside from the predicted values, this work also includes samples produced by the reference model. To this aim, the second metric provides a single value parameter in the form of mean deviation between the reference model and interpolated values or measured samples called MAE [105].

4.4 Proposed Methodology

This section's main idea is to propose a methodology for deciding on the minimum set of measurement points needed for coverage map construction. The procedure is tightly connected with the Chapter 3 as it utilizes the same input data acquired during the extensive measurement campaign. It also uses the proposed fine-tuned models from the previous chapter to create the baseline reference models used by this study. In the following stages, the selected interpolation methods and thinning algorithms are applied [105].

4.4.1 Assessment Procedure Steps

The whole process of identifying the minimal set of measurement points can be divided into four main tasks (i) reference model derivation, (ii) coverage estimation, (iii) quantitative comparison between the models, and (iv) accuracy assessment of the models against measured values. For a more granular depiction of the procedure in question, see Fig. 4.1 [105].
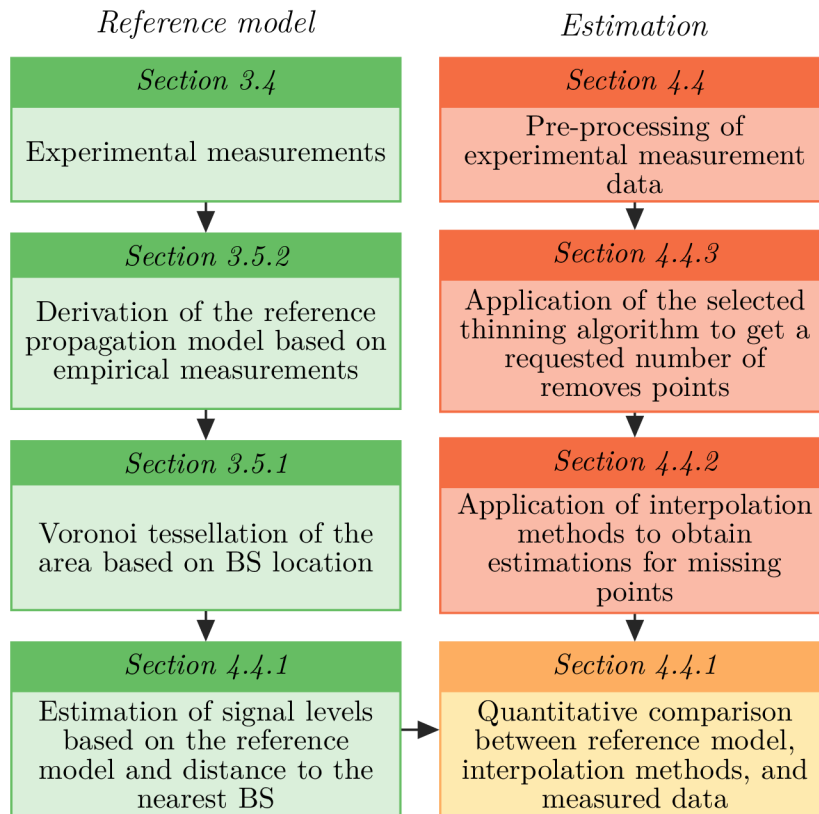

Fig. 4.1: Main steps of assessment process [105].

The knowledge of the exact BSs locations, in the first step of this process, is combined with the fine-tuned propagation models to derive a reference model for each

LPWA technology. In the second phase, the interpolation methods are employed to derive models without the explicit knowledge of BSs locations. To this aim, interpolation methods use measured RSRP values as the input dataset for NB-IoT, while Sigfox and LoRaWAN models are derived from RSSI. The RSRP provides a more accurate channel assessment as it measures only the R0 (also R1 when available) reference signal, thus excludes interferences from other antenna sectors and channels [56]. However, for Sigfox and LoRaWAN, this metric is not present as they use omnidirectional antennas without reference signals. It is the main reason why these technologies are limited to RSSI, which integrates power from the whole bandwidth [105].

Notably, two different point reducing methods are applied to identify the minimal set of measurement points for an accurate assessment. Namely, it is probabilistic and deterministic thinning. These algorithms significantly impact the selection of measurement locations, as the deterministic thinning tends to form measurement points in a regular grid. In contrast, the output of the probabilistic ones is inherently random. As a result, the selection of thinning algorithm is expected to affect coverage assessment accuracy. Both algorithms are consecutively applied to the input dataset until the required number of retained points is not achieved. In the next step, the MAE metric (3.22) is applied to quantitatively characterize the distance between interpolated data with a reduced input dataset (created without BSs location knowledge) and the reference model (derived using BSs locations knowledge). Finally, the accuracy of values predicted by the reference model and interpolation methods is assessed by side-by-side comparison with the measured samples. Based on these results, the decision on the minimal number of measurement points needed to derive a coverage map with a given maximal deviation is made [105].

Metrics of Interest

To provide a simple visual assessment of the derived coverage map, the probability that a certain fraction of the area is covered with a signal level of at least x dBm is employed. In what follows, this metric is applied to both the reference model and the interpolated values. First, the area of interest is divided into a regular grid. Then, the coverage quality is estimated by extracting RSRP/RSSI values at each grid point and putting them in a cumulative array. In other words, this assessment metric represents an inverse CDF of the sample values [105].

The inverse CDF metric allows for a straightforward comparison of the reference model with interpolated values, but it does not provide a quantitative comparison of the distance between these models. Hence, this work reuses the averaged MAE metric 3.22 defined in the previous chapter to facilitate the quantitative comparison

between models. Recall that the modulus is used to account for positive and negative deviations, and the resulting value is independent of the total number of sample points N [105].

Reference Model

The reference model's derivation represents the same procedure as defined in Section 3.5.1. It requires converting the RSRP/RSSI samples to the path loss values. Next, the non-linear regression is employed to derive the continuous path loss curve. This empirical model is then approximated by the verified propagation models as closely as possible, see Fig 4.2. For NB-IoT and LoRaWAN, the fine-tuned Ericsson Urban model provides the most accurate prediction as the mean deviation (based on the MAE formula 3.22) is not larger than 0.1 and 1.1 dB, respectively. In the case of Sigfox, 3GPP Urban represents the most accurate propagation model with the mean deviation not exceeding 0.2 dB.

In the last step, the knowledge of BSs locations is used to divide the area into the corresponding regions utilizing the Voronoi tessellation. It allows splitting the area into sections where all polygon points are closer to the appropriate BS than to any other seed. Notably, the measurement points are distributed over the area of interest in a regular grid with a spacing of 50 m. Finally, the fine-tuned propagation models are used to predict the expected signal levels at each cell of this grid. As an input parameter of these models, the point's distance to the closest BS is used. Such a generated coverage map represents a reference model used in the next steps of the accuracy assessment.

4.4.2   Interpolation Algorithms

In this work, the interpolation algorithms are essential to predict values at those points where the measurement data are not available. However, it must be noted that the measurement points are not evenly spaced over the whole area of interest, but they are grouped along the public transport lines stops. Such an input dataset requires the application of interpolation methods for scattered data. In this study, five well-known interpolation algorithms for arbitrarily spaced data are used. Namely, selected interpolations include (i) Nearest-neighbor, (ii) Linear, (iii) Natural-neighbor, (iv) IDW, and (v) Kriging. The algorithms listed above are sorted from the simplest Nearest-neighbor interpolation up to the most complex Kriging [105].

(a) NB-IoT.

(b) Sigfox.

(c) LoRaWAN.
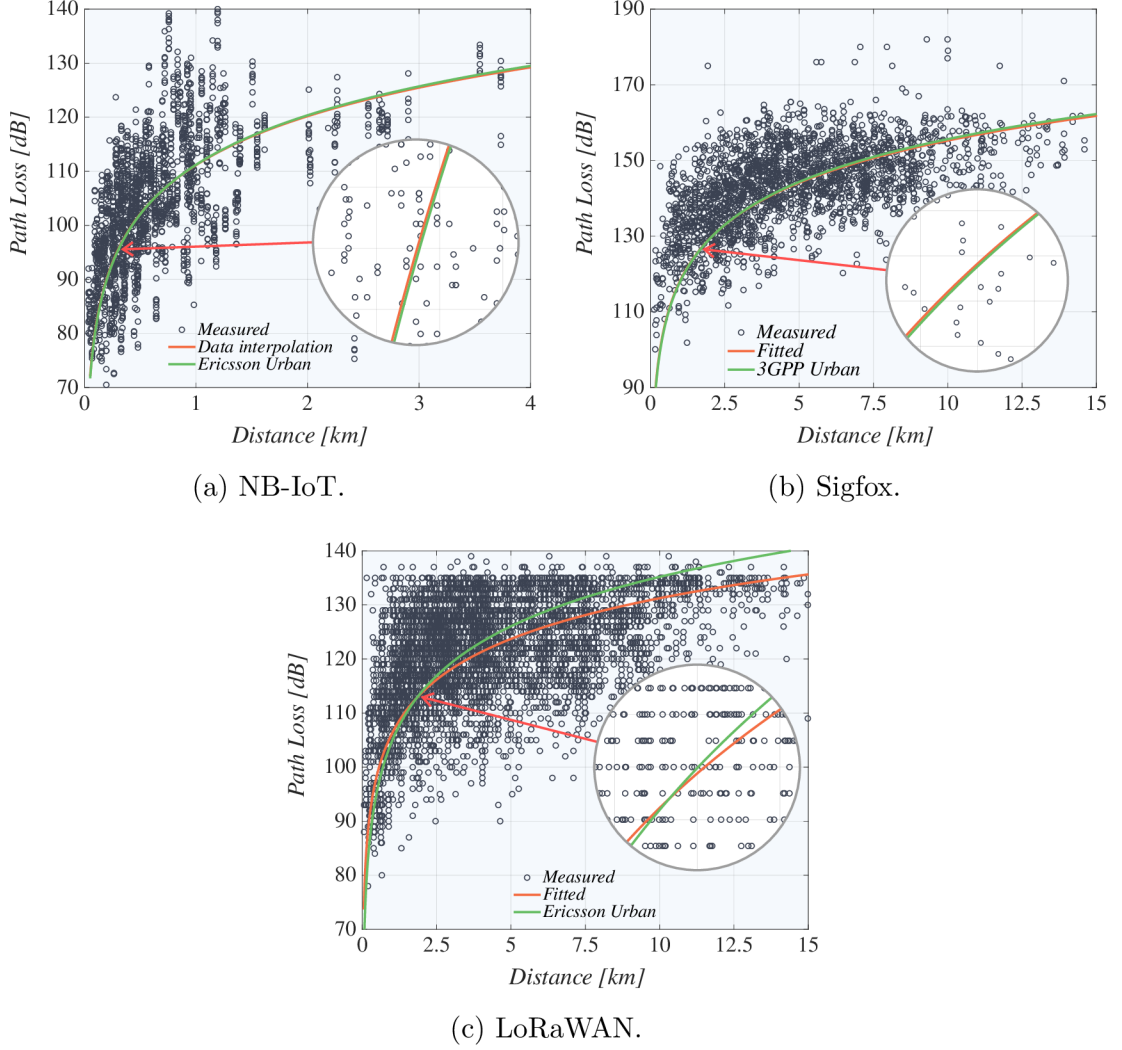
Fig. 4.2: Fitting of propagation model to measurement data [105].

Nearest-Neighbor

This method represents the most straightforward approach to data interpolation. At the first step, the Delaunay interpolation is applied to the input set of measurement (sample) points denoted as x. After the triangulation, each vertex is lifted by the magnitude V which corresponds to the sample point x value. Then, to acquire the value of the requested point x_q, the same lifting procedure is conducted. The requested point x_q is lifted until it does not intersect the corresponding triangle delineated by the sample points x. In other words, it involves traversing the triangulation structure to find the triangle enclosing the requested point. Finally, the nearest point x value is computed and reused in the requested point x_q [105,114,115].

Due to the simplicity of this method, the computational demands are low. However, this interpolation method accuracy is not the best as it does not predict new

values for the requested points x_q but only duplicates the existing ones. This property leads to the formation of sharp transitions between values at the edges of the neighboring cells [105, 114, 115].

Linear

The main principle of Linear interpolation is similar to approach used by the Nearest-neighbor method. The Delaunay triangulation tessellates the area of interest. Then, the vertices of the measurement points x are lifted by the magnitude V. However, contrary to the Nearest-neighbor algorithm, the requested points x_q are not duplicated from the closest sample point x. Instead, they are calculated as the weighted sum of all three vertices that constitute the enclosing triangle [105, 114].

Linear interpolation employs the Barycentric coordinates system to overcome the values prediction problem when the points lie directly on the vertices' connecting lines to provide the most accurate results [116]. When the requested point x_q is inserted into the triangle and connected to each vertex, the resulting diagram contains three separate triangles with the corresponding areas A_1, A_2, and A_3. If the whole area of the original triangle is denoted as A, the Barycentric coordinates α, β, and γ [117] are derived as

$$\alpha = \frac{A_1}{A}, \quad \beta = \frac{A_2}{A}, \quad \gamma = \frac{A_3}{A}. \tag{4.1}$$

The resulting sum of these coordinates must always be equal to one. Therefore, this knowledge can be used to speed up the third coordinate calculation by subtracting the sum of the first two parameters from one. The final value of the interpolated point is calculated as

$$x_q = \alpha V_a + \beta V_b + \gamma V_c, \tag{4.2}$$

where V_a, V_b, V_c represent the values of the appropriate triangles vertices and α, β, γ denote the Barycentric coordinates [105].

The main benefit of this interpolation is its relative simplicity and speed. It is still considerably slower than the Nearest-neighbor algorithm, as the calculation of Barycentric coordinates and the weighted sum requires additional computing time. However, compared to the Nearest-neighbor, the Linear interpolation provides C^0 smoothness [105, 115].

Natural-Neighbor

The Natural-neighbor interpolation builds upon a plane portioning structure called the Voronoi diagram. As an initial step, the known points x are used to tessellate the intended area. Each cell of the resulting figure consists of one generator point (known point x), which defines the entire polygon's value. Logically, the Voronoi tessellation is discontinuous, but the Natural-neighbor interpolation uses its useful characteristics. For example, each edge of the polygon represents a link between two generating (measurement) points. This property allows for easy identification of the corresponding neighbors for the interpolation [105, 118].

Similar to Linear interpolation, the requested point x_q is inserted into the Voronoi diagram in the next step. Consequently, the newly inserted point x_q produces a new polygon added to the resulting Voronoi structure. As a result, a portion of the neighboring polygons is consumed by the new polygon, and edges covered by the new cell are subsumed. The main goal of the next step is to calculate the area consumed by the inserted polygon from the surrounding cells. Each fraction of the area contributed by the neighbor cells represents the polygon weight, which, combined with its value, gives the resulting requested point x_q magnitude. The fractional weight of the polygon λ_i can be derived as

$$\lambda_i = \frac{A_i}{A}, \tag{4.3}$$

where A_i represents the area of the contributing cell i and A is the total area of the inserted polygon. As in the case of Linear interpolation, the sum of the weights is equals to one. In the last step, the requested point x_q value is calculated as

$$x_q = \sum_{i=0}^{N} \lambda_i \cdot z_i, \tag{4.4}$$

where N represents the number of neighboring cells, λ_i is the element weight, based on (4.3), and z_i stands for the sample point value [105, 119].

The main advantages of Natural-neighbor interpolation include relative simplicity, speed, and resilience to biases introduced by the clustering of the points. On the other hand, its slope discontinuity prevents C^1 continuity over the entire surface [105, 118, 119].

Inverse Distance Weighting

The main premise of IDW interpolation assumes that values of proximate points are more related than distant ones. In practice, it means that the interpolated value of the requested point x_q is calculated as a linearly weighted combination of known

sample points. The weight of each point is defined as an inverse function of distance. With this knowledge, the requested point value is derived as

$$x_q = \frac{\sum\limits_{i=o}^{n} d_i^{-p} \cdot z_i}{\sum\limits_{i=0}^{n} d_i^{-p}}, \tag{4.5}$$

where z_i denotes sample point value, d_i is the distance between the desired and known sample point. Finally, p represents the power parameter that controls the influence of the known point x on the interpolated value. The closest points have the largest impact on the resulting value of the requested point x_q. Notably, the power value p is not strictly defined and does not have any connection to the real-world process. Usually, the convention is to use the power of two, which is also employed in this work. The last parameter n determines the number of samples considered for interpolation of the requested point x_q. Typically values higher than three are recommended [105, 120].

The selection of these input arguments significantly influences the resulting behavior of IDW interpolation. On top of this, IDW provides additional flexibility in the selection of sampling points used for interpolation. Instead of the exact number of neighboring points, the interpolation may use a fixed search radius in which all the points contribute to the resulting predicted value. The search window does not have to be a perfect circle, but it can have an almost arbitrary shape. In the current study, the requested point x_q is interpolated from the five closest neighboring points [105, 121].

IDW represents an intuitive method of data interpolation, which is still computationally efficient. However, its accuracy significantly decreases with unevenly distributed measurement points. It also can not provide C^1 smoothness. Moreover, the selection of multiple input arguments is arbitrary without connection to the physical world, but it radically influences the interpolation behavior [105, 120].

Kriging

This interpolation method belongs to the geostatistical algorithms group build upon statistical models that incorporate autocorrelation properties (in the sense of mathematical relation between sample points). It allows these techniques to produce not only the predicted value but also offer accuracy assessment. Notably, the accuracy of Kriging is the highest when the input data is spatially correlated over the distance or contains a directional bias [105, 122].

The derivation of the interpolated value stems from an idea similar to the Natural-neighbor and IDW mechanisms, i.e., the requested point x_q value is cal-

culated as a weighted sum of neighboring points, see (4.3). However, the way how the individual weights are acquired differs drastically. Kriging weights are not derived solely from the distance to the sample point but also account for the measurement points' spatial arrangement. To this aim, Kriging follows a two-step process of (i) creating covariogram and covariance function, and (ii) unknown values prediction [105, 123].

In the initial step of Kriging, an experimental semi-variogram is derived as

$$\gamma(h) = \frac{1}{2N(h)} \sum_{i=1}^{N(h)} [z(x_i) - z(x_i + h)]^2, \tag{4.6}$$

where $N(h)$ represents the number of pairs separated by the distance h and $z(x_i)$ is the value of the sample point. Then, the experimental semi-variogram is fitted to one of the predefined empirical semi-variograms. This step is necessary because the experimental semi-variogram does not represent a continuous function, but it is only a set of individual points. A Spherical semi-variogram is used in this work as it provides the closest match with the experimental semi-variogram. The selected empirical semi-variogram is defined as

$$\gamma(h) = \begin{cases} c_o + c_1 \left[\frac{3h}{2a} - \frac{1}{2} \left(\frac{h}{a} \right)^3 \right] & \text{for} \quad 0 < h < a \\ c_o + c_1 & \text{for} \quad h \geq a \end{cases}, \tag{4.7}$$

where a is the range, c_0 denotes the nugget variance, and $c_0 + c_1$ represents the sill.

Further, in the last step, Kriging produces the prediction on the value of the requested point x_q. This work is based on Ordinary Kriging, but there are other variants of this algorithm [124]. For the Ordinary Kriging, the system is defined as

$$\begin{bmatrix} \lambda_1 \\ \vdots \\ \lambda_n \\ \mu \end{bmatrix} = \begin{bmatrix} C_{11} & \cdots & C_{1n} & 1 \\ \vdots & \ddots & \vdots & \vdots \\ C_{n1} & \cdots & C_{nn} & 1 \\ 1 & \cdots & 1 & 0 \end{bmatrix}^{-1} \begin{bmatrix} C_{10} \\ \vdots \\ C_{n0} \\ 1 \end{bmatrix}, \tag{4.8}$$

where μ is the Lagrange parameter, and C_{1n} denotes the covariance between the locations of sample points x_1 and x_n. The samples covariance is derived as

$$C_{1n} = Cov(x_1 - x_n) = C(0) - \gamma(x_1 - x_n), \tag{4.9}$$

where $C(0)$ is the semi-variogram sill, and γ represents the value generated by the semi-variogram for the joining points x_1 and x_n. Finally, the acquired weights λ_n are used to predict the value of the requested point x_q according to (4.4) [105].

The main benefit of Ordinary Kriging over the deterministic methods is that the information about spatial relations is readily included in weight calculation. On the other hand, Kriging is computationally demanding. Notably, the derivation of sample points weights represents computationally complex task [105, 122].

4.4.3 Thinning Algorithms

In theory, the accuracy of the interpolation algorithms under thinning should depend on the way how the points are selected. This study, therefore, discusses two different approaches to this issue. The first method is entirely random, whereas the second algorithm uses a semi-deterministic principle [105].

Probabilistic Thinning

Probabilistic thinning represents a straightforward approach, which has an important feature that is directly translated into the selection of the measurement points when planning a measurement campaign. In probabilistic thinning, the choice of the removed elements is entirely random, and individual points are selected independently [105].

Deterministic Thinning

The most accurate predictions should be provided when the measurement locations are densely and evenly spread over the entire area. To this aim, the deterministic thinning ensures that for a given number of the retained points, they reside as far from each other as possible [105].

Deterministic thinning follows these steps to acquire the measurement points' locations from a random dataset. It (i) specifies $M \times M$ grid defining the squares on the coverage map, (ii) estimates number the number of in each resulting square and sort them in descending order. The algorithm further (iii) determines how many points need to be removed, and (iv) removes the measurement points from the square with the highest number of elements in a way that the number of retained points equal to the number of points in the second largest cluster (based on the number of points). The thinning continues (v) with removing the items from two squares having the highest number of points until they do not contain the same number of points as the third-largest cluster. This process finishes when (vi) the required number of points has been removed [105].

For all considered interpolation methods, a similar procedure of identifying the set of measurement points that characterize the coverage quality with a particular deviation is employed. Namely, $10\,\%$ of measurement points are removed at

each round, and the coverage estimation metrics are calculated. The application of probabilistic thinning is straightforward and does not requires additional discussion. However, it must be noted that the latter approach is naturally deterministic only on the $M \times M$ grid level. The points in individual squares are removed randomly, which leads to the probabilistic behavior on the cluster level [105].

Artificial Points

The thinning procedure is also tightly connected with the addition of artificial points to the corners of the interpolated area. Without this step, extrapolation would be necessary in the cases of a large number of removed points. However, such behavior is unwanted. Each artificial point value is set to LPWA technologies minimum sensitivity, which is a value around -140 dBm. However, the utilization of artificial points is reduced as much as possible to mitigate influence on the interpolation results. These points are inserted into the input dataset only when the area delineated by the measurement pints can not be fully interpolated (interpolation returns undefined values). This approach has been proven reliable, as the interpolation is influenced only in the extreme cases of removed points (more than 97 %) [105].

4.5 Numerical Results

This section summarizes numerical results and evaluates the considered coverage assessment strategies. The main goal is to assess the accuracy of selected interpolation methods with different densities of measurement points in the propagation environment where the BSs locations remain hidden. To this aim, two assessment metrics defined in Subsection 4.4.1 are employed. Notably, the comparison of interpolated values with the reference model should be considered as a comparison of two models rather than an accuracy assessment of the interpolations with the "ground truth". The comparison of both interpolated samples and reference model with actually measured values is employed to this aim. This approach allows the most accurate comparison of interpolation algorithms with the "ground truth" data [105].

4.5.1 Comparison of Interpolation Methods

Before assessing the constructed coverage maps' accuracy with a limited number of measurement points using different thinning algorithms, the performance of selected interpolation methods is analyzed. To this end, the candidate interpolation methods are applied on the scattered input dataset with the ultimate goal of producing a regularly spaced grid of predicted values. The interpolation algorithms' performance

is directly compared with the reference model described in Subsection 4.4.1 using both inverse CDF and integral MAE metric [105].

The visual comparison of interpolation methods for all three LPWA technologies with the reference models employing the inverse CDF metric is depicted in Fig. 4.3. Recall that this metric is defined as the cumulative percentage of the area featuring the RSRP/RSSI level of at least x dBm. As one may observe, none of the considered interpolation algorithms provide a perfect match with the reference model. Nevertheless, some of the algorithms give significantly better results than the others. Notably, the Nearest-Neighbor algorithm is characterized by the significant deviations from the reference model in the regions of low and high RSRP/RSSI values [105].

In the case of NB-IoT, the IDW algorithm does not provide satisfactory results, especially in the area around the median value of RSRP. Generally, the performance

(a) NB-IoT.
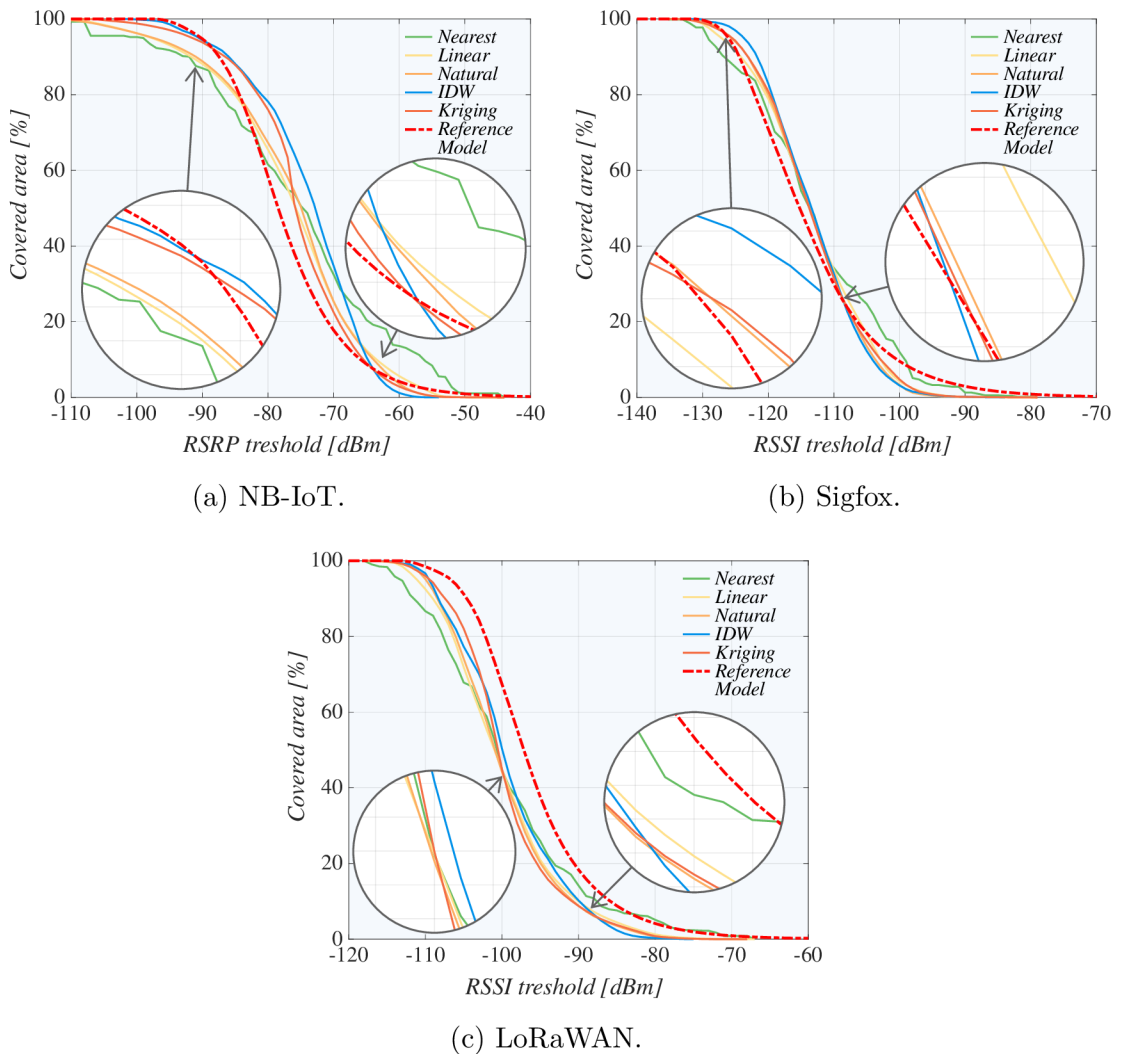
(b) Sigfox.

(c) LoRaWAN.

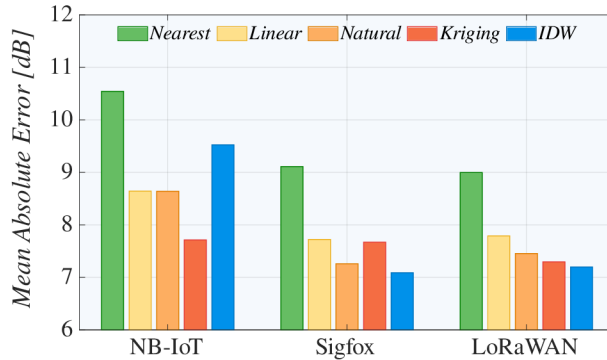Fig. 4.3: Comparing interpolation methods with reference model [105].

Fig. 4.4: Mean deviation for interpolation methods [105].

of individual interpolation algorithms indicates the most significant differences for NB-IoT. Mainly, this phenomenon is caused by two factors. In comparison with Sigfox and LoRaWAN, the density of NB-IoT BSs deployment is significantly higher. Hence, measurement point interpolation in such a system represents a more challenging task. It also explains why individual algorithms differ significantly, as each method relies on a different approach to value predictions. The second reason is that the majority of measurement points lie in a short-range of RSRP values oscillating around -75 dBm. Therefore, the borderline samples have to be interpolated using points with less related values resulting in a higher prediction error. For Sigfox and LoRaWAN, the differences between individual interpolation methods are significantly smaller [105].

For the numerical quantification of the interpolation method's performance, Fig. 4.4 delivers a comparison with the reference model by employing the MAE assesment metric (3.22). This parameter can be interpreted as a deviation of predicted RSRP/RSSI values from the reference model averaged over the number of points in the area of interest (points in the regular grid). As one may observe, the average metric results confirm the conclusions drawn from the visual analysis. Notably, the Nearest-neighbor algorithm indicates the highest deviation from the reference model for all considered LPWA technologies [105].

Surprisingly, IDW, the second-worst interpolation for NB-IoT, provides the lowest deviation from the reference model of all interpolation methods for Sigfox and LoRaWAN. By contrast, the Kriging, being the best performing algorithm for NB-IoT, performs as the second-worst in the case of Sigfox and LoRaWAN. The remaining methods, i.e., Linear and Natural-neighbor interpolations, provide satisfactory results for all LPWA technologies. Still, the more complex Natural-neighbor algorithm slightly outperforms the Linear interpolation. In summary, all intended algorithms' results are comparable despite having different approaches to deriving the predicted value [105].

The next important finding is connected with the prediction quality concerning the BSs deployment density. Analyzing data presented in Fig. 4.4, it is clear that the highest deviation is observed for the NB-IoT, which also posses the highest BSs density of all considered technologies. Contrary, the prediction for Sigfox and LoRaWAN indicates noticeably better results – this also confirms the visual observation gained from Fig. 4.3. In conclusion, the NB-IoT deviation from the reference model is around 8.5 dB and approximately 7.4 dB for Sigfox and LoRaWAN [105].

4.5.2 Comparison of Models under Thinning

Once the baseline performance of interpolation methods is evaluated, the study proceeds with assessing the algorithms' performance under thinning. To this aim, two different point removal approaches introduced in Subsection 4.4.3 are employed. By employing the thinning methods, the study addresses how interpolation methods' accuracy degrades with varying percentages of excluded measurement points. Also, the influence of different thinning approaches on predicted values and the selection of retained points is discussed. Notably, this work targets the dynamic environments where the radio conditions may change at each measurement location. Due to this fact, even the fine-tuned models may provide inaccurate results, and the interpolated values can provide higher accuracy. Thus these results should be considered as a comparison of differences between two models rather than an accuracy assessment [105].

In Fig. 4.5, the performance of the two most accurate interpolation algorithms (Natural-neighbor and Kriging) for NB-IoT technology is displayed. The results cover both probabilistic and deterministic thinning, gradually retracting 10, 30, and 70 % of measurement points. Notably, the figure illustrates the portion of the area covered with a given RSRP value, representing the inverse CDF metric from Subsection 4.4.1. The NB-IoT technology is selected because it indicates the highest deviation from the reference model for all intended interpolation methods. Also, the disparity between individual interpolations algorithms is highest for NB-IoT. The results display output of 30 subsequent algorithm runs to provide statistically consistent data. Accordingly, the resulting curves represent the results' median value, while the translucent areas denote the 5th and 95th percentile [105].

The first essential conclusion is that the difference among the median values between thinning algorithms is nearly negligible for a low number of retracted measurement points, i.e., 10 % (30 out of 300) and 30 % (90 out of 300). However, the variance of the probabilistic thinning results is significantly higher as it is represented by a wider translucent area surrounding the median value curve. The difference is even more pronounced with the larger portion of removed points, i.e.,
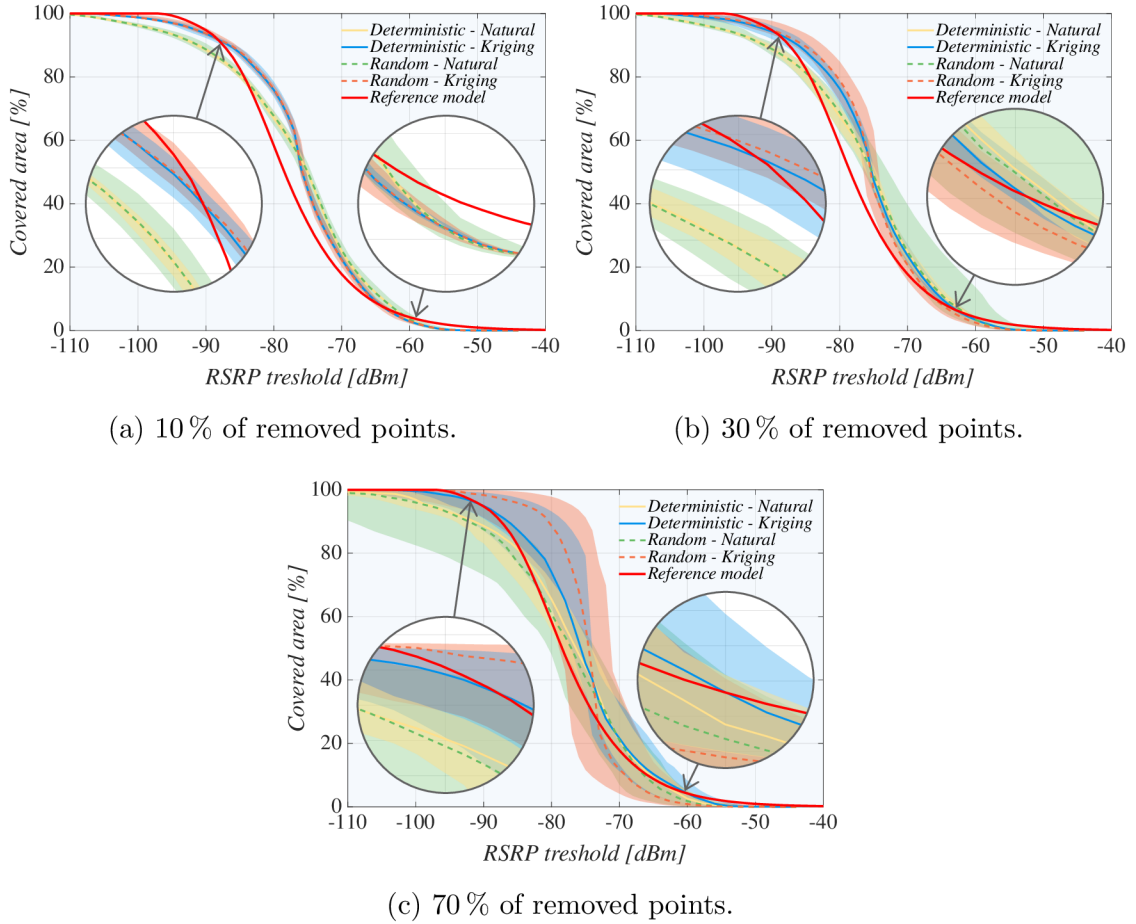
(a) 10 % of removed points.

(b) 30 % of removed points.

(c) 70 % of removed points.

Fig. 4.5: Comparison of interpolation methods under thinning for NB-IoT [105].

70 % (210 out of 300). At this point, both thinning algorithms indicate increased results variation; however, the fluctuation of the deterministic algorithm is still two times smaller. Surprisingly, the median value difference between probabilistic and deterministic thinning is significantly lower for Natural-neighbor interpolation. On the other hand, Kriging indicates significant differences, especially for RSRP values between -90 and -75 dBm. It is probably caused by the Kriging algorithm's covariogram range, limiting the influence of the sampling point on the interpolated value. Thus, with the more considerable separation distances between measurement points, the Kriging algorithm produces bounded areas surrounding the sampling points and settles on the average value for the rest of the plane. In summary, the visual observation reveals that a regular structure such as a grid for planning the coverage assessment allows decreasing the variance of the results significantly. It is even more important for a lower number of sampling points. Notably, these conclusions are not valid only for NB-IoT, but similar behavior has been observed for Sigfox and LoRaWAN deployments [105].
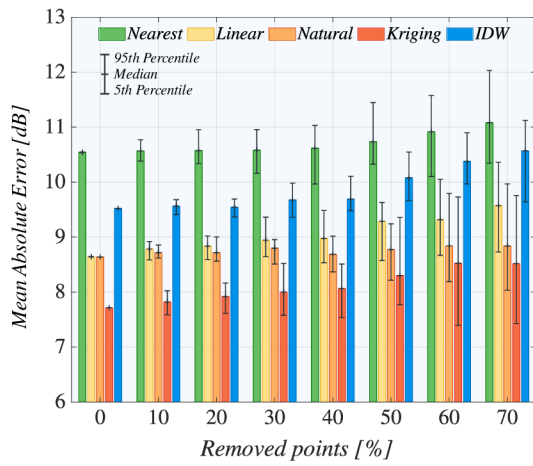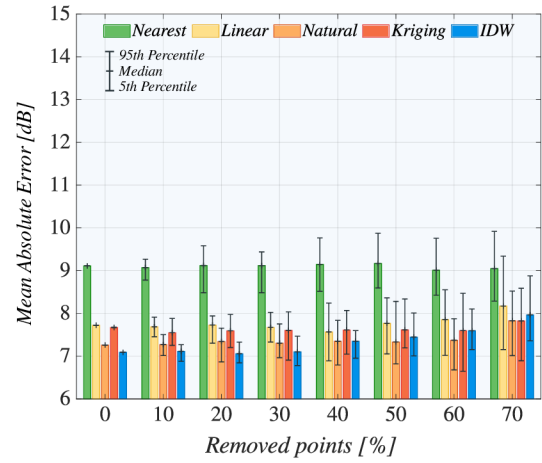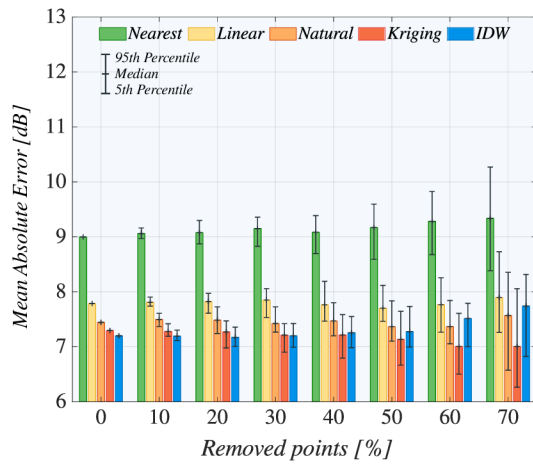
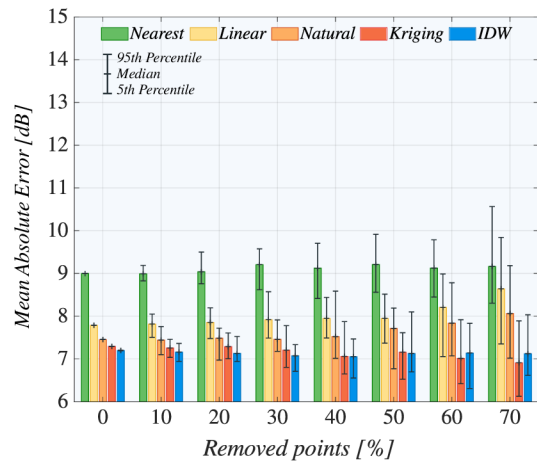(a) NB-IoT, Deterministic.
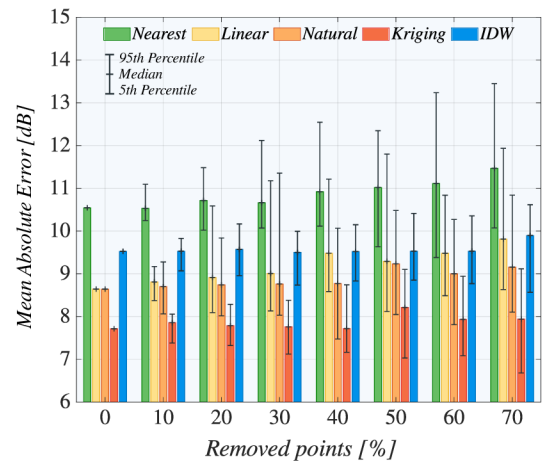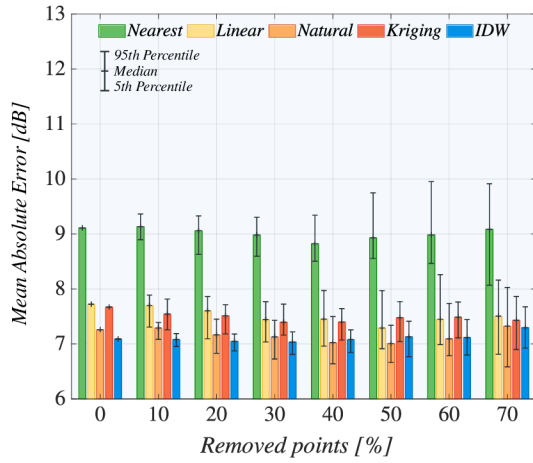
(b) NB-IoT, Probabilistic.

(c) Sigfox, Deterministic.

(d) Sigfox, Probabilistic.

(e) LoRaWAN, Deterministic.

(f) LoRaWAN, Probabilistic.

Fig. 4.6: Coverage accuracy assessment for interpolated data under thinning [105].

In the next step, the interpolation performance under thinning is ranked based on the integral MAE metric defined in (3.22). Fig. 4.6 illustrates the mean deviation of considered LPWA technologies for deterministic and probabilistic thinning, respectively. Similar to the previous case, the results summarize the output of 30 procedure runs. The barplot's head represents the median value, while the error bars delineate the 5th and 95th percentile [105].

Concentrating on NB-IoT, it is clear that the Kriging interpolation provides the best predictions for both thinning approaches. Moreover, the closer analysis shows that the median values of the mean deviation for deterministic and probabilistic thinning are nearly identical. The probabilistic thinning even provides smaller deviation error on several occasions, however, only by a narrow margin (in order of tenths of percents). In the case of the prediction variance, the deterministic thinning provides more coherent results. As expected, this difference raises proportionally with the number of removed points. On average, the variance of probabilistic thinning is two times higher regardless of the interpolation method. This finding concludes that by using deterministic thinning, one can expect more consistent results, even though they can be slightly biased by the selection of the sampling points locations. The influence of the biased points selection is most visible for the IDW interpolation in the cases of more than 50 % removed points. From this point, the probabilistic thinning displays superior results over the deterministic method. The IDW predicts the interpolated values from the five closest neighboring points; thus, there is a higher chance of nearby points clustering when probabilistic thinning is applied. Conversely, the deterministic thinning tends to spread the measurement points more evenly. Thus the interpolation has to select more remote points with weaker mutual coherence [105].

Surprisingly, for Sigfox and LoRaWAN, the IDW provides significantly lower values of MAE for both thinning approaches. Until 40 % of removed points, IDW even displays the smallest deviation from the reference model for both LPWA technologies and thinning methods. For more than 50 % of removed points, IDW represents the second best performing interpolation method for Sigfox, while the Natural-neighbor holds first place. With 70 % of removed points, the situation changes, as IDW again represents the best performing algorithm for deterministic thinning. However, in the case of probabilistic thinning, the IDW holds third place after Natural-neighbor and Kriging. For LoRaWAN, the Kriging is superior to all other interpolation methods for both deterministic and probabilistic thinning from 40 % of removed points [105].

The next important conclusion one can draw from the presented results is that the thinning method selection is not a deciding factor for the sparse deployments. For Sigfox, which has six times sparser BSs deployment compared to NB-IoT, the difference between 5th and 95th percentile variation under deterministic and proba-

bilistic thinning is nearly negligible. Conversely, for NB-IoT with higher deployment density, the variance of MAE values is almost two times higher for probabilistic thinning [105].

In conclusion, the results presented in Fig. 4.6 share common properties valid for all technologies, interpolation methods, and thinning algorithms. As one may observe, by decreasing the number of measurement points, the mean deviation and the variance of the results rise, reducing the statistical confidence in obtained results. However, the denser deployments represented by NB-IoT indicate higher mean deviation. Also, the performance of thinning algorithms is influenced by the deployment density. For sparser deployments, the selected thinning method has only a marginal impact on the results, e.g., median and variation. In the case of these sparse deployments, such as Sigfox and LoRaWAN, the IDW interpolation represents the best choice for up to 40 % of removed points (1.2 points per km^2). For dense cells (e.g., NB-IoT), Kriging provides the lowest MAE values throughout the whole range of removed points and thinning methods. On the opposite side stands the Nearest-neighbor algorithm, which produces the highest deviation from the reference predictions in all situations. Finally, the mean deviation metric does not indicate any sharp increase in the whole range of retracted points from 10 % (1.8 points per km^2) to 70 % (0.6 points per km^2) [105].

### 4.5.3   Lower Bound on Number of Measurements

As the previous experiments retracting up to 70 % (0.6 points per km^2) of measurement points did not identify any particular point where the MAE deviation sharply increases, the whole procedure is relaunched in the range of 95 % (0.1 points per km^2) to 99 % (0.02 points per km^2) of removed points. This step's primary goal is to find a lower bound on the number of required measurement points. The resulting integral metric characterizing the average deviation from the reference model is depicted in Fig. 4.7 [105].

For NB-IoT, one can see the similar characteristics of thinning algorithms as in the case of Fig. 4.6. The deterministic thinning provides more consistent results compared to the probabilistic approach. Surprisingly, the IDW interpolation under deterministic thinning indicates a better approximation of the reference model. In this case, it is the second-best performing prediction algorithm after Kriging. However, the Nearest-neighbor and Linear interpolation methods show two times higher MAE values than the initial state of zero removed points. The most exciting findings are connected with Kriging and Nearest-Neighbor interpolation methods. These algorithms show only a marginal increase of mean deviation even for 98 % of removed points. It means that the Delaunay triangulation used by Nearest-neighbor
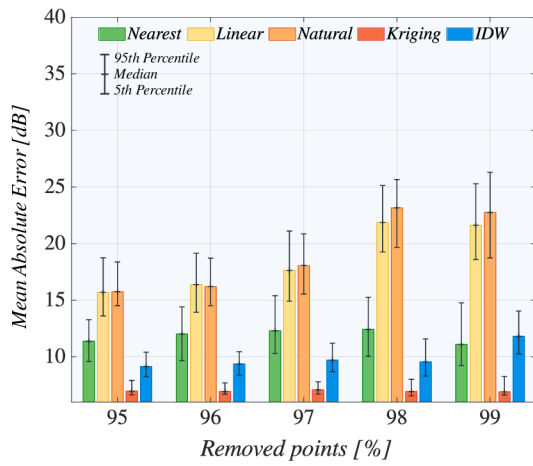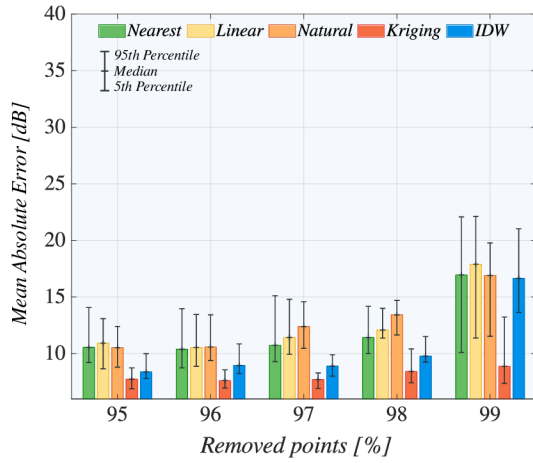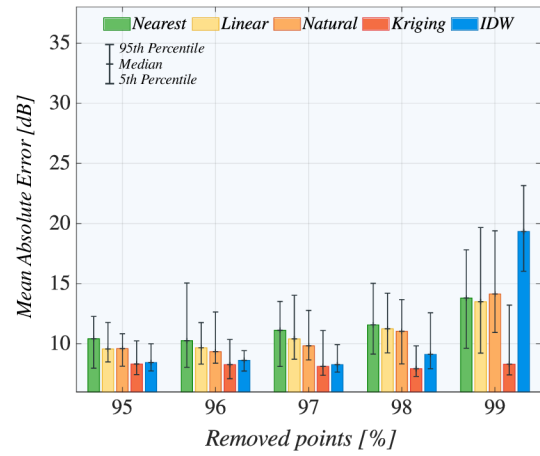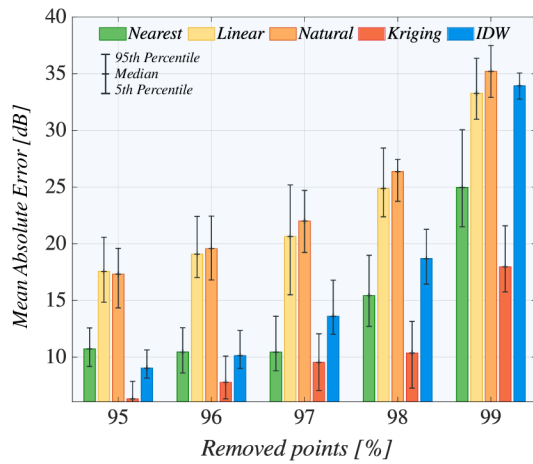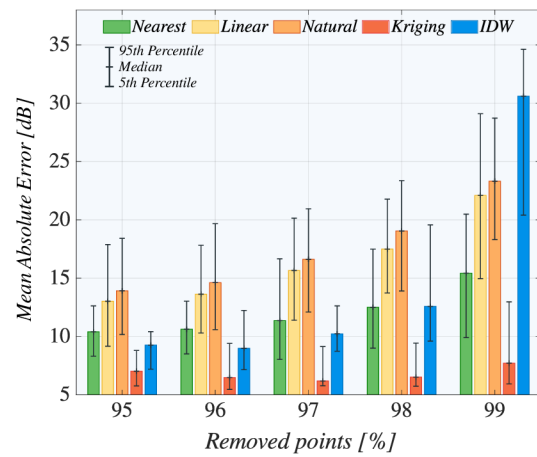
(a) NB-IoT, Deterministic.
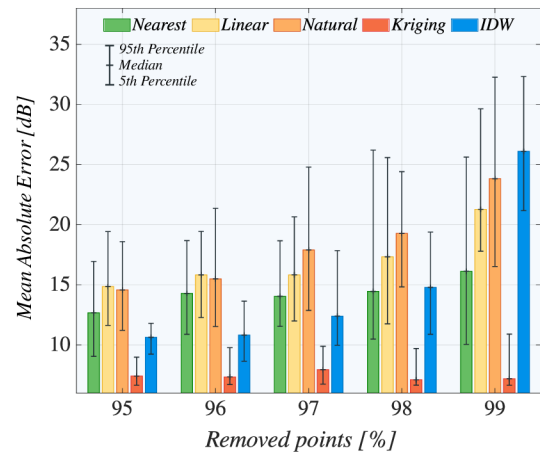
(b) NB-IoT, Probabilistic.

(c) Sigfox, Deterministic.

(d) Sigfox, Probabilistic.

(e) LoRaWAN, Deterministic.

(f) LoRaWAN, Probabilistic.

Fig. 4.7: Coverage accuracy assessment on lower bound of measurement points [105].

with a constant value in each cell provides a better approximation of the reference model than Linear and Natural-neighbor interpolations based on the weighted average. In the case of Kriging, the interpolated values are influenced mainly by the variogram range. For the longer distances, Kriging slowly settles to the samples' median value [105].

Conclusions similar to NB-IoT can also be drawn from LoRaWAN and Sigfox results. The Linear and Natural-neighbor interpolations are characterized by the highest deviation of all methods, while the Nearest-neighbor provides surprisingly consistent results. Further, Sigfox indicates the most balanced outcomes for all interpolation methods and thinning algorithms. It confirms the premise of deployment density influence on the prediction accuracy. A thorough analysis of the results further shows that the largest increase in mean deviation is visible from 98 % of removed points. However, this increase is connected with the influence of the artificial sample points on the interpolation [105].

4.5.4   Accuracy Comparison with Measurement Data

Previous evaluations showed that the difference between the reference models and interpolation methods. However, these values reflect only the differences between the two models. Therefore, in the last step of the numerical evaluation, the accuracy of reference and interpolated models is evaluated against the real measurement results. Such an approach represents the only way how of comparing the predicted values with the "ground truth" data. The comparison process is straightforward and follows principles similar to the previous steps. In each round of the thinning procedure, retracted points' values are compared to those predicted by the interpolation methods and reference model. Predictions accuracy is assessed based on the MAE metric defined in (3.22). It must be noted that only the values of removed points are considered for the accuracy assessment as the interpolation methods retain the values of generating points even for the predicted samples. It would create an unwanted bias for the interpolation methods if all points were considered [105].

As in the previous cases, the comparison of MAE for both thinning procedures depicted in Fig. 4.8 confirms the influence of network deployment density on the prediction accuracy. On average, the MAE values for the NB-IoT technology which is characterized by the highest deployment density, are increased by about 2-3 dB. Both deterministic and probabilistic thinning methods independently verify these findings. However, the most unexpected finding is related to the performance of the reference model in comparison with the interpolation methods. In all cases, at least one interpolation method (often most of them) displays significantly better prediction accuracy than the fine-tuned propagation (reference) model. As expected,
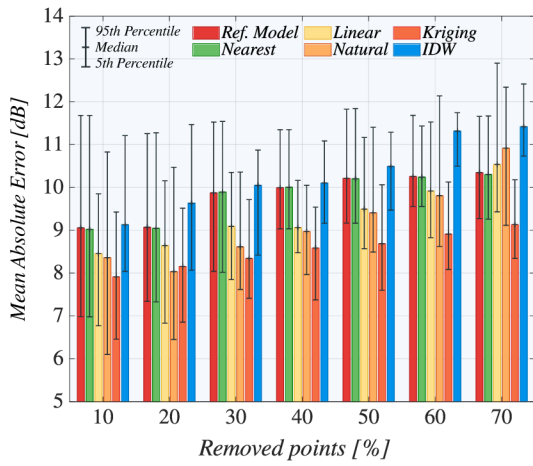
(a) NB-IoT, Deterministic.
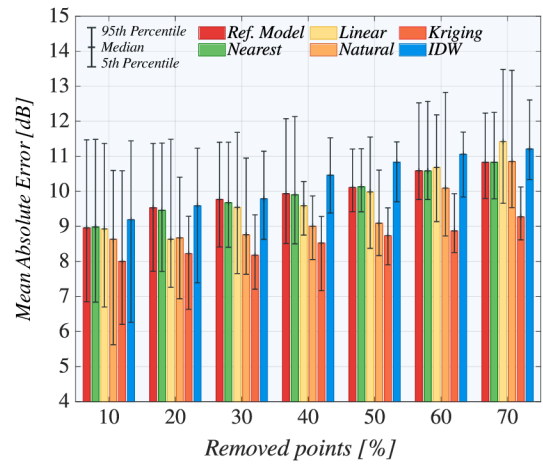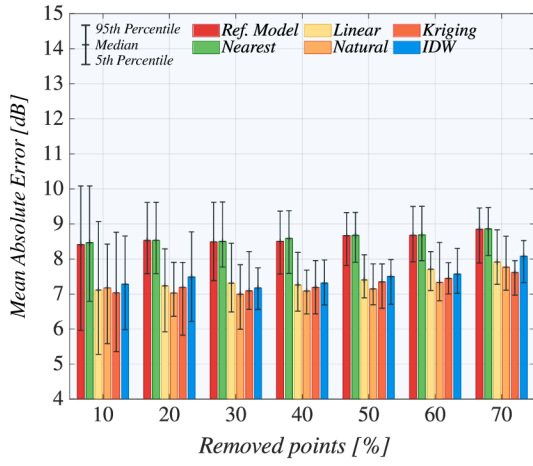
(b) NB-IoT, Probabilistic.

(c) Sigfox, Deterministic.

(d) Sigfox, Probabilistic.

(e) LoRaWAN, Deterministic.
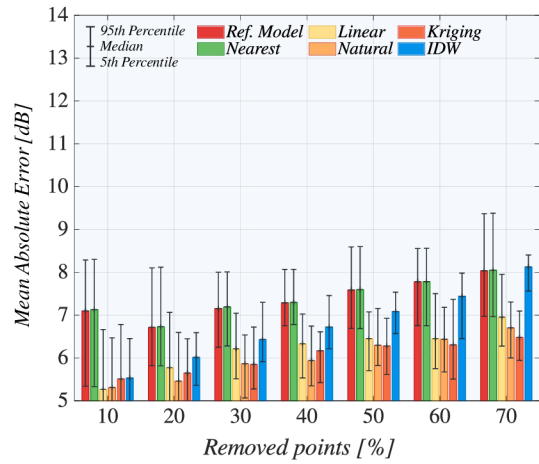
(f) LoRaWAN, Probabilistic.

Fig. 4.8: Coverage accuracy assessment for interpolated data under thinning [105].

the interpolation method providing the worst approximation is the simple Nearest-neighbor algorithm. However, for NB-IoT, the IDW interpolation provides the most inaccurate results. Although the IDW performance for LoRaWAN is not convincing, in the case of Sigfox, it can keep up with other methods. For deterministic thinning, it is even one of the most accurate interpolation. These observations suggest that IDW is a good choice for the technologies with a lower density of BSs [105].

However, the Kriging represents the most versatile interpolation method providing accurate results independent of selected communication technology, thinning procedure, or a number of retracted measurement points. In summary, the result also suggests that the influence of thinning algorithms is negligible. Contrary to the previous comparison of interpolated values with the reference model, the MAE, in this case, is nearly identical for both deterministic and probabilistic thinning. Also, the results' dispersion is comparable for both methods; only the LoRaWAN under deterministic thinning breaks this rule. In this case, the deviation linearly increases with the number of retracted points. For the rest, the MAE is almost constant from $10\,\%$ (1.8 points per km^2) up to $70\,\%$ (0.6 points per km^2) of removed points [105].

4.5.5   Lower Bound on Number of Measurement Points

As in the case of reference and interpolated model comparison, the previous experiment did not reveal any particular point where the accuracy starts to deteriorate dramatically. Hence, the whole procedure is repeated for an extreme number of retracted points, i.e., from $95\,\%$ (0.1 points per km^2) up to $99\,\%$ (0.02 points per km^2). The ultimate goal of this step is to identify a lower bound on the required number of measurement points that is capable of producing accurate predictions. As usual, the MAE metric defining the absolute deviation from measured values for both thinning methods is depicted in Fig. 4.9 [105].

Just a brief look at the results reveals that the prediction accuracy for different LPWA technologies is enormous. The NB-IoT results confirm the previous findings related to the relation between deployment density and the prediction error. Numerically, the MAE of NB-IoT is almost two times higher compared to both Sigfox and LoRaWAN. Notably, this finding is valid for both deterministic and probabilistic thinning. Clearly, the Kriging algorithm still holds first place as the most accurate interpolation for all considered LPWA technologies. It also provides significantly higher accuracy compared to the reference model. However, the most surprising finding is connected with the Nearest-neighbor interpolation. For the extreme number of removed pints, i.e., $98\,\%$ and $99\,\%$, the presence of artificial corner points most probably causes the increased inaccuracy of Linear and Natural-neighbor interpolation methods. But in the case of the lower number of removed points, the natural
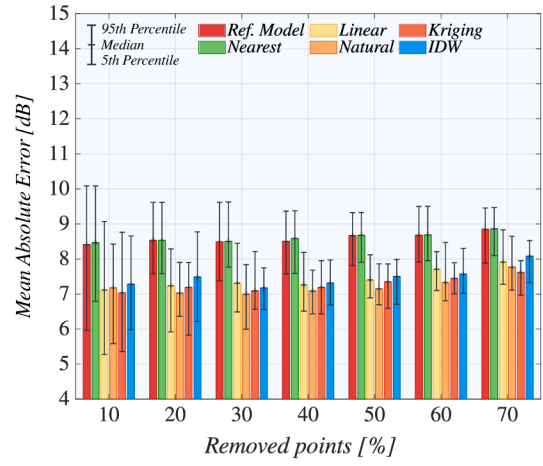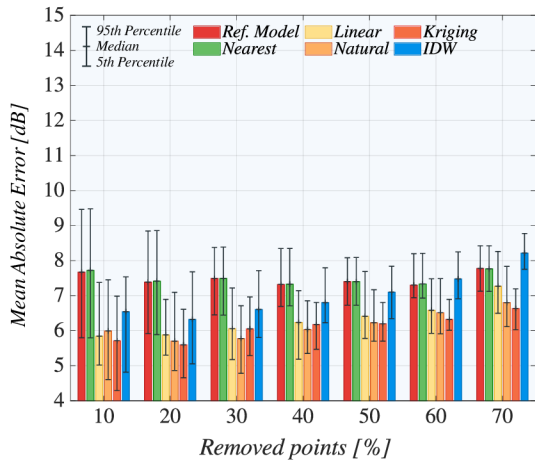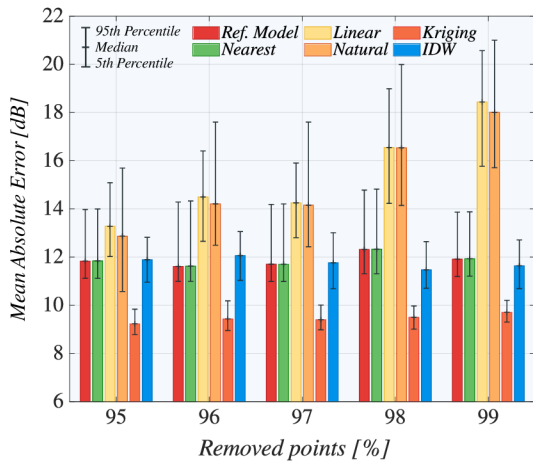
(a) NB-IoT, Deterministic.
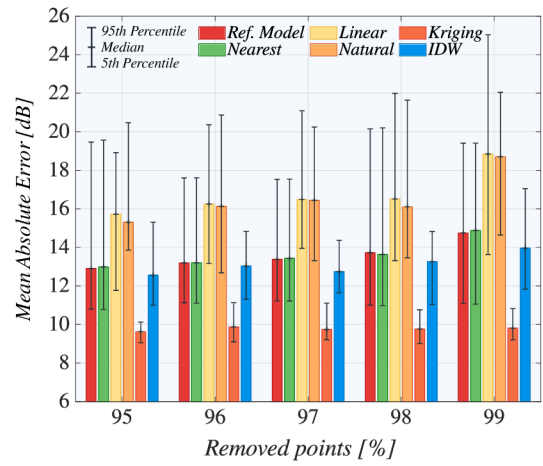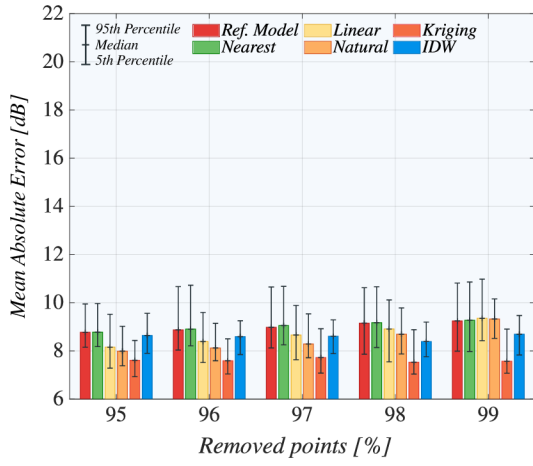
(b) NB-IoT, Probabilistic.

(c) Sigfox, Deterministic.
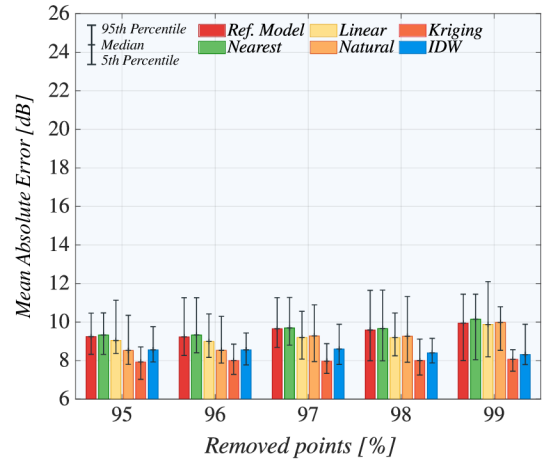
(d) Sigfox, Probabilistic.
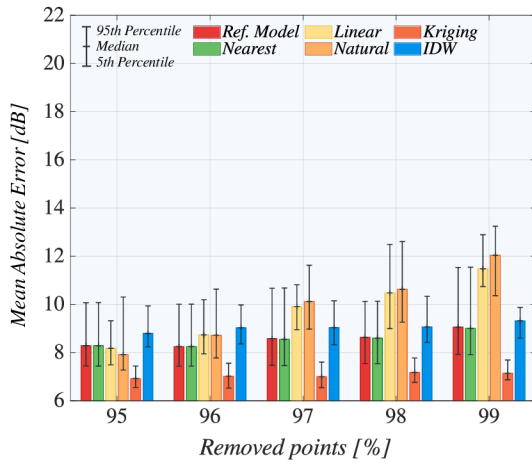
(e) LoRaWAN, Deterministic.
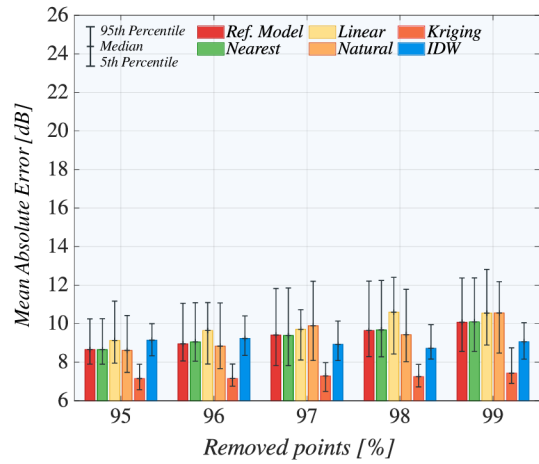
(f) LoRaWAN, Probabilistic.

Fig. 4.9: Coverage accuracy assessment on lower bound of measurement points [105].

behavior of these algorithms must cause the increased inaccuracy. Notably, Linear and Natural-neighbor algorithms cannot adequately capture the relation between far-distant points. Thus the Kriging algorithm, specifically designed for this type of correlation, shows superior results [105].

5 Multi-RAT Solution for mMTC Scenarios

The usual consensus on modern MTC communication is that it can be divided into two main groups [125]. The first category, also known as mMTC, is characterized by extreme densities of EDs without strict requirements on communication delay and data loss. Nowadays, the LPWA technologies are the most known representatives of this category. With M.2412 requirements in mind, LPWA systems are designed to deliver 90 % of messages with a radio interface delay of less than 10 s. On the other hand, the second group poses extremely low latency requirements with values under 5 ms. The 3GPP is currently working on the standardization of these URLLC technologies as a part of the 5G NR interface [126].

However, a plethora of newly emerging mMTC applications stand between these two extremes. The typical representatives are assets tracking, health monitoring, condition-based monitoring, and smart metering. These applications require much stricter delay requirements than mMTC but are still more relaxed than the ones given by URLLC. Also, reliability and availability are becoming more critical. One of the options to solve this issue is to develop a new RAT supporting these applications, for example Digital Enhanced Cordless Telecommunications (DECT)-2020 mMTC initiative. The different approach to this issue is to adapt current technologies to fulfill the stringent application requirements. These changes can be implemented on the ED utilizing a sophisticated transmission scheme, multi-RAT interface, or handover detection mechanism [75, 127, 128].

This work investigates the concept of combining multiple LPWA technologies into one multi-RAT device addressing the issues mentioned above. The proposed research's premise is that the radio channel conditions between ED and BS may change dramatically over the device lifetime. The radio conditions can be affected by various environmental changes such as weather conditions, construction works, and infrastructural updates. Notably, the timescale of these events may differ significantly from seconds to years. In the time of deployment, the prediction of such phenomena is difficult, and the effect on the radio channel is not easy to assess beforehand. Hence, despite the higher complexity of the multi-RAT solution, it may positively impact the ED lifetime [75].

The main aim of this research study is to utilize a multi-RAT solution with dynamic switching to the best technology based on the propagation conditions. As the radio channel conditions are not known in advance, the selection of the most suitable technology is conducted automatically in response to the environmental changes. Currently, the system employs a RL mechanism that automatically selects the radio interface with the ultimate goal of achieving the highest reward. In the case of this study, it is to maximize the ED battery life [107].

5.1 Time Dependent Modeling

Implementation of advanced mechanisms such as the multi-RAT transmission requires full knowledge of the propagation channel, which is subject to variation even for static deployments of EDs. Therefore to facilitate the development of a radio interface selection algorithm with the ultimate goal of minimizing power consumption, a substantial understanding of the time-dependent characteristics of the propagation environment is crucial [106].

To this aim, a long-term measurement campaign capturing the received signal characteristics (RSRP/RSSI) of the stationary EDs was conducted. The measurement results show that signal characteristics are subject to drastic changes that may influence the ED communication performance. Hence, the first- and second-order properties of these radio channel parameters are analyzed and modeled. For this purpose, a doubly-stochastic Markov chain modeling framework is used. The designed model can serve as a building block of analytical or simulation-based systems-level studies requiring the long traces of samples that faithfully capture time-dependent characteristics [106].

5.1.1 Measurement Campaign

To capture long-term time-dependent characteristics of the radio channel in the urban environment multi-RAT evaluation board was designed. The prototype is equipped with communication modules for three major LPWA technologies, namely NB-IoT, Sigfox, and LoRaWAN. As the technologies operate in neighboring frequency bands (for Sigfox and LoRaWAN 868 MHz, NB-IoT 800 MHz), the device is set to perform sequentially to reduce the possibility of interferences [107].

The measurement campaign took place in the city of Brno during the two months period. In total, two evaluation boards were deployed to capture the time-dependent characteristics in different types of urban deployment. The first prototype has been deployed on the university building roof, whereas the second board was located in the apartment close to the city center. Both devices were configured identically to convey 12 B messages with one hour period. The identical datagrams were sent through all radio interfaces, and the available statistics were stored for subsequent analysis. For each LPWA technology and deployed sensor, more than 1400 messages were acquired. All tests were conducted in commercial networks with a multi-gateway setup, reflecting real-world conditions of production deployment. As in the case of previous research, RSSI is used as a signal quality indicator for Sigfox and LoRaWAN, whereas NB-IoT relies on the RSRP as it potentially excludes interferences with other sectors [107].

5.1.2 Statistical Data Analysis

This section discusses the time-dependent properties of acquired RSSI/RSRP samples experienced by the two ED in the urban environment. One is placed on top of the BUT building (BUT sensor) while the second is situated in the apartment in the Brno city center (Brno city center (BCC)). On top of that, first- and second-order characteristics, as well as the ergodicity and stationarity needed for the modeling, are covered [107].

RSSI/RSRP Time-Series

The main goal of this study is to design simple yet accurate models for time-dependent channel modeling. The main research area lies in the class of covariance stationary ergodic stochastic process to balance between the mathematical traceability and the modeling accuracy. Notably, the stationary covariance process is fully characterized by the distribution of its single section and Autocorrelation Function (ACF) [129]. Hence, the RSSI/RSRP properties as well as first- and second-order characteristics have to be analyzed before selecting the suitable time-dependent model. These properties are represented by the histogram of relative frequencies and the ACF of empirical data [106].

Based on the visual analysis of a long time RSSI/RSRP measurements depicted in Fig. 5.1, important conclusions can be drawn. First, there are indeed significant variations of signal levels caused by environmental changes in both considered locations. Surprisingly, the BUT sensor's rooftop placement indicates better overall signal strength, as expected, but shows a higher variation of results. Only the NB-IoT displays expected results as the signal fluctuation for rooftop placement is minimal. Naturally, the number of interferences and obstacles is minimal for the rooftop deployment. However, Sigfox and LoRaWAN results do not hold up to this premise. It is also visible that the BCC sensor situated inside the apartment shows an additional 10 up to 15 dB attenuation compared to the BUT deployment [107].

Further, one can observe that it is possible to apply the "hidden states" notion to demonstrate the signal behavior. The RSSI/RSRP samples shift their values between a set of "levels" characterized by a long duration of samples around the mean level. Moreover, the fluctuations within each group appear stochastically similar to the external observer. All these findings support the primary idea that the target model should differentiate between states with unique stochastic properties [107].

First and Second Order Characteristics

The first-order characteristics of the RSSI/RSRP process are depicted in Fig. 5.2 using histogram of relative frequencies. It can be seen that the histogram has multiple
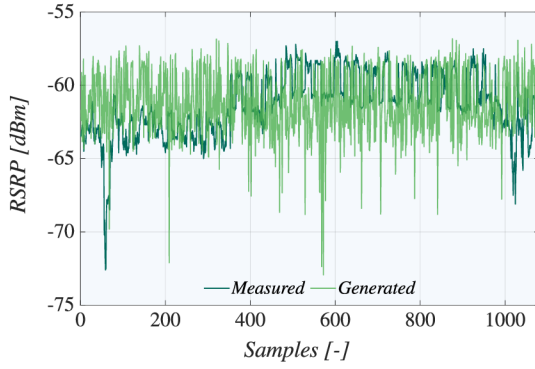
(a) NB-IoT, BUT.
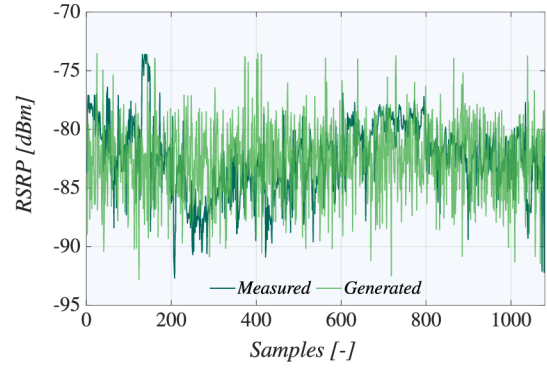
(b) NB-IoT, BCC.
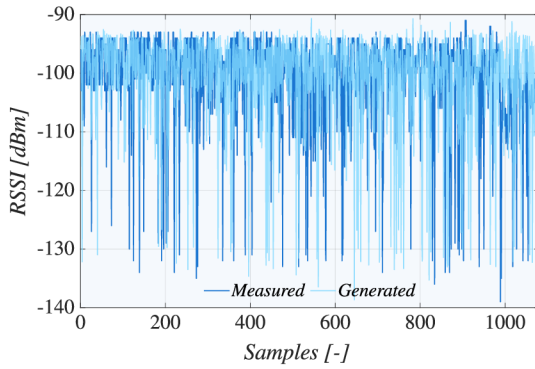
(c) Sigfox, BUT.
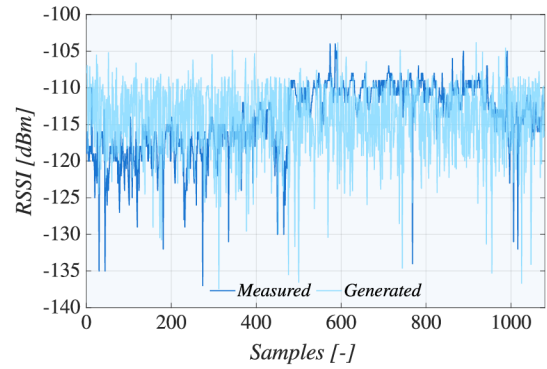
(d) Sigfox, BCC.
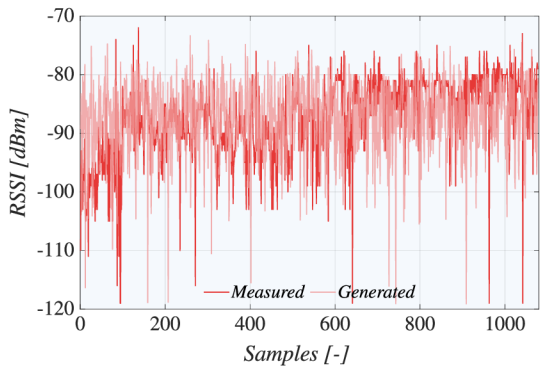
(e) LoRaWAN, BUT.
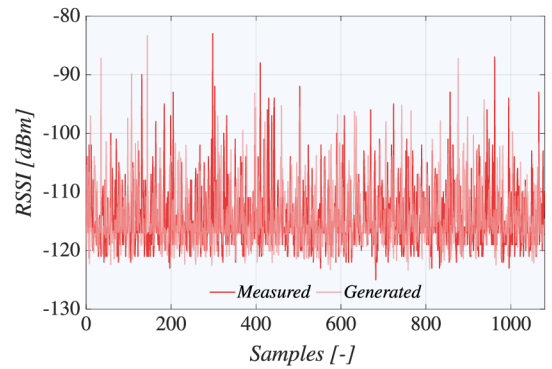
(f) LoRaWAN, BCC.

Fig. 5.1: Comparison of RSRP/RSSI samples [107].

peaks, which characterize the mean value of different states. Therefore, this finding implies that the original premise of state-based behavior is indeed confirmed [107].

The normalized ACF depicted in Fig. 5.3 represents the second-order characteristics of the propagation environment. The confidence intervals defined by the dashed line confirming the relation at lag x are calculated based on the rule of thumb

(a) NB-IoT, BUT.
(b) LoRaWAN, BUT.
(c) Sigfox, BUT.

(d) NB-IoT, BCC.
(e) Sigfox, BCC.
(f) LoRaWAN, BCC.
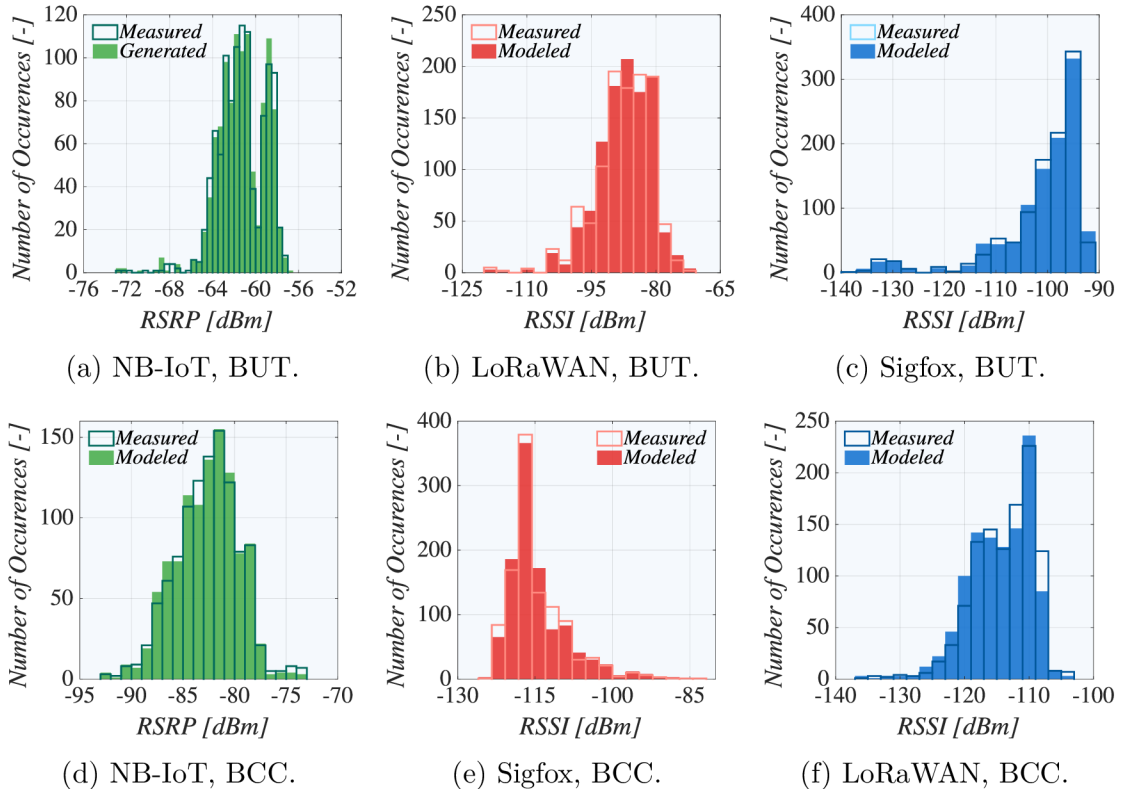
Fig. 5.2: Histogram of relative frequencies [107].

[130] confirming the relation at lag i as

$$|\overline{\rho_i}| \geq 2/\sqrt{n}, \tag{5.1}$$

where n is the number of lags. Further, the constant 2 approximates the value 1.96, which corresponds to the confidence limit of $\alpha = 0.05$. Notably, the ACF of empirical data is often prone to outliers and ACF estimation's initial point. Therefore, the only qualitative conclusions drawn from the visual analysis of ACF are related to its structure, as discussed in [131]. One of the critical conclusions is that the ACFs for all considered LPWA technologies are characterized by exponentially decaying behavior. It implies that such a process can be accurately captured by using stochastic models with short-term memory [107].

Ergodicity and Stationarity

The ergodicity of the process must be tested to verify if the considered properties are, in fact, representative. Notably, the sufficient condition of ergodicity is $K(n) \to \infty$, where $K(n)$ is n-lag ACF of the process. Based on the analysis of ACF depicted in Fig. 5.3, one may conclude that this condition does hold for all three LPWA technologies in both locations. This finding implies that it is safe to use the histogram
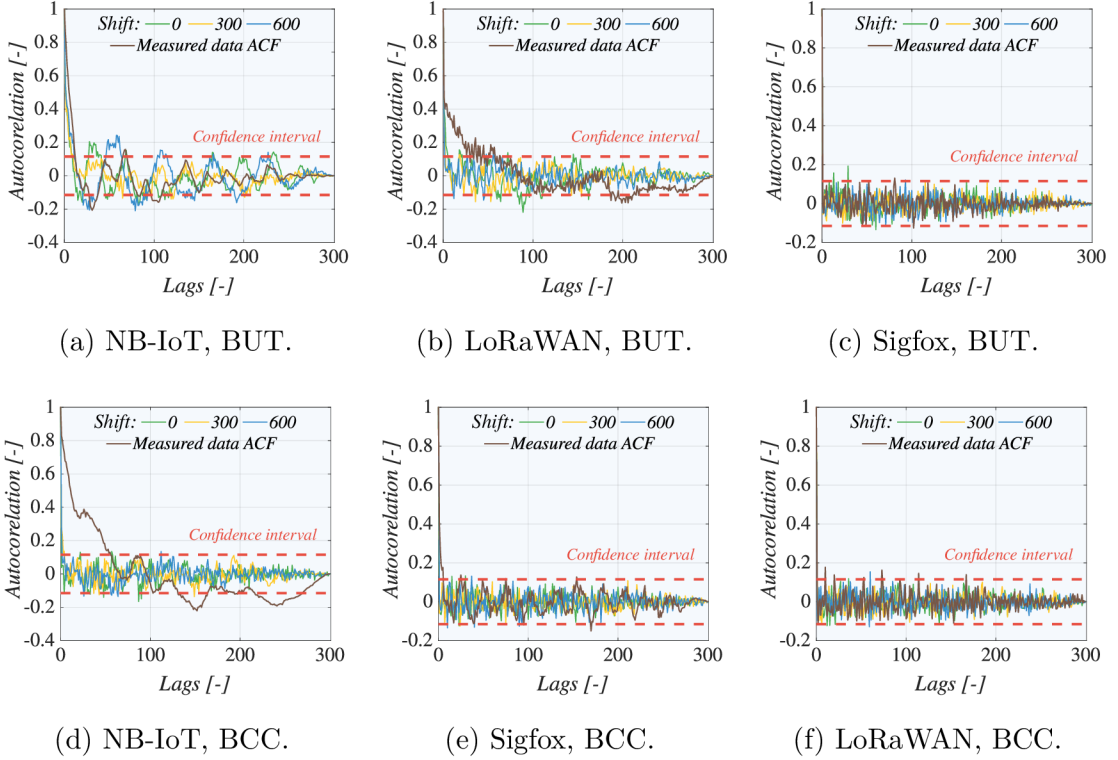
Fig. 5.3: Comparison of ACFs [107].

of relative frequencies and the ACF of a single trace as representative characteristics of RSSI/RSRP processes in the analyzed environment.

5.1.3 Doubly-Stochastic RSSI/RSRP Modeling

The RSSI/RSRP process analysis revealed that a generic shape characterizes its histogram of relative frequencies while the ACF has a distinct exponential diminution. Such properties are specific for the doubly-stochastic Markov chains (also known as hidden Markov chains) that have been frequently used in the past as a convenient tool for modeling traffic dynamics in packet networks. Notably, these models can be used either in mathematical and simulation-based studies of LPWA technologies as this type of model retains its analytical traceability [106, 132–135].

The doubly-stochastic Markov models can be fitted using several generic algorithms, including those based on the expectation-minimization technique [136] or maximum likelihood estimation adaptation [137]. Nevertheless, these techniques are beneficial only when the Markov modulating chain's internal structure is not clearly observable, and the Markov chain consists of many states or a combination of both. In the case of this study, where the number of states is low, more straightforward techniques can be employed. The whole process of constructing the

doubly-stochastic Markov chain consists of three main steps. First, the number of states N must be determined. Then one needs to estimate the transition probabilities $p_{ij}, i, j = 1, 2, \ldots, N$ and the conditional Probability Mass Function (PMF) associated with each state, $f_i(j), i = 1, 2, \ldots, N, j \geq 0$.

The Kernel Density Estimation (KDE) clusterization algorithm is applied to input data to determine the number of states N in the modulating Markov chain [138, 139]. This process consists of two steps: (i) estimation of Probability Density Function (PDF) and (ii) data clusterization based on the local maxima. The samples' PDF is derived as

$$\hat{f}(x) = \frac{1}{nh} \sum_{i=1}^{n} K \left(\frac{x - x_i}{h} \right), \tag{5.2}$$

where n is the sample size, h denotes the bandwidth, x stands for the actual value, and x_i represents the input samples. The kernel smoothing function K uses a PDF with a normal distribution. The bandwidth of the kernel smoothing function heavily impacts the resulting approximation tightness. Therefore, to obtain the optimally smoothed KDE, the bandwidth is calculated according to

$$h = \sigma \left(\frac{4}{3N} \right)^{1/5}. \tag{5.3}$$

In this case, the σ is the standard deviation, and N represents the sample size [106].

Finally, the states of the Markov chain are derived from the local maxima of the resulting KDE. Each local maxima on the resulting KDE curve represent a boundary of the Markov chain state. Two remaining Markov chain state bounds are derived from the minimum and maximum RSSI/RSRP values of the input data set[106].

When the number of states N is acquired, it is necessary to determine the transition probabilities $p_{ij}, i, j = 1, 2 \ldots, N$ and PMFs associated with each state $f_i(j), i = 1, 2, \ldots, N, j \geq 0$. These values are gained using conventional statistical methods. First, the state boundaries between the states are defined, and the number of state changes for particular values of i and j (current and previous trace values) is divided by the number of samples in the entire trace [106].

5.1.4 Numerical Assessment

Visual comparison of measured values with the samples generated by the doubly-stochastic Markov chain depicted in Fig. 5.1, verifies that the main characteristics of the empirical traces are adequately captured. Notably, the Markovian process's memoryless nature does not allow to follow the input data sequence with each value change precisely. Recall that the decision on transition to the next state (which

state will be selected) does not depend on the previous state but only on the current one. Hence, the probability of transition to the appropriate future state is solely decided by the transition probability matrix of the particular state [106].

Visual analysis of the histogram of relative frequencies depicted in Fig. 5.2 verifies that the first-order characteristics are captured accurately. Also, χ^2 statistical test for the heterogeneity of the samples was performed to support these visual observations. The test shows that both samples belong to the same distribution with the $\alpha = 0.05$ level of significance [106].

As expected, the comparison of ACF on Fig. 5.3 reveals no perfect match between the ACFs, as they are heavily dependent on the selection of the initial estimation point. Nevertheless, the accuracy of the proposed doubly-stochastic Markov model can be confirmed by additional statistical tests. To this aim, the Box-Ljung test for correlation of the first M lags is employed [140]. The test shows that empirical and modeled traces have a statistically confirmed correlation up to the lag $n = 10$ [106].

5.2 Learning-Aided MR-mMTC Implementation

This study's ultimate goal is to improve the battery life of the LPWA Multi Radio (MR)-RAT devices, which is negatively impacted by the use of multiple radio interfaces. Therefore, the "selective" multi-RAT functionality is considered as it utilizes only a single radio interface at a time (even though the device is equipped with multiple communication technologies). The main challenge of this approach is how to select the best interface at each time [107].

The solution to the interface selection problem proposed in this work involves reinforcement learning, a subclass of Machine Learning (ML) algorithms. The RL algorithms focus primarily on the MAB problem with the primary goal of achieving the highest reward by pulling the right arms. To this aim, the selected MAB policies in this study cover (i) ε-greedy, (ii) weighted average, (iii) Upper Confidence Bound (UCB), and (iv) Thompson sampling algorithms [107].

5.2.1 Power Consumption Characterization

The prediction of multi-RAT device battery life requires full knowledge of each technology power consumption in all operating modes. Therefore, an extensive measurement campaign in the laboratory environment was conducted. The laboratory setup depicted in Fig. 5.4 allows for power consumption measurements of LPWA modules for signal levels ranging from -68 to -133 dBm. In the case of NB-IoT, such a wide range covers all Enhanced Coverage Level (ECL) classes from ECL0 to ECL2 [107, 141].
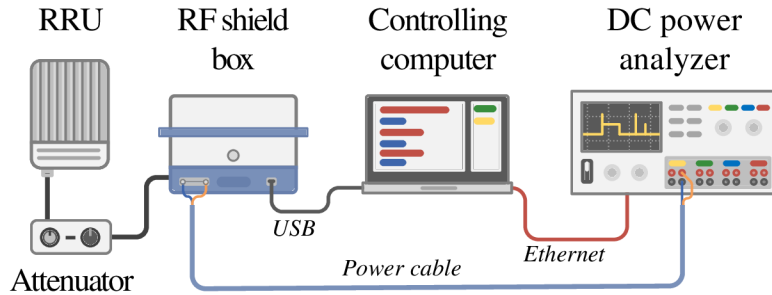
Fig. 5.4: Power consumption measurements workplace [107].

The desired signal levels can be set via the step attenuator connected between the Remote Radio Unit (RRU) and the measured NB-IoT module placed in the Radio Frequency (RF) shield box. The actual current consumption is measured by the power analyzer Agilent N6705A with a sampling period of 0.0248 ms. Due to the Sigfox technology limitation, the power consumption is measured only for 12 B message transmission. All measurements at each signal level (12 in total) are repeated ten times to gain sufficient confidence bounds. Notably, Sigfox and LoRaWAN measurements are simplified as these technologies do not require any registration nor signalization before UL message transmission. Hence, the power consumption is independent of signal strength level. It also allows moving the modules from the shielding box during the measurements [107].

It must be noted that the NB-IoT technology is represented by the uBlox SARA N210 communication module implementing the Rel. 13 of the 3GPP standard with support for single communication band B20. In the case of LoRaWAN, the communication module from company Microchip designated as RN2483 is used. Finally, as Sigfox technological enabler, sub-GHz communication module S2-LP produced by ST Microelectronics company is employed [107].

Measurement Results

The power measurement results depicted in Fig. 5.5 clearly illustrate that for NB-IoT operating in ECL0, the current consumption is nearly constant in the whole range from -68 to -108 dBm. The first noticeable increase in power consumption is present in ECL1 for -113 and -118 dBm. However, the most significant growth is visible for ECL2 starting from -121 dBm. A side-by-side comparison of NB-IoT reveals that the power consumption in ECL2 can be up to 15 times higher compared to ECL0. Also, the variation of measurement results, i.e., 5th and 95th percentile represented by the error bars, is significantly higher in ECL2 [107].

The message retransmissions primarily cause this difference, as it is one method of improving the ling budget heavily used in NB-IoT. The number of retransmission
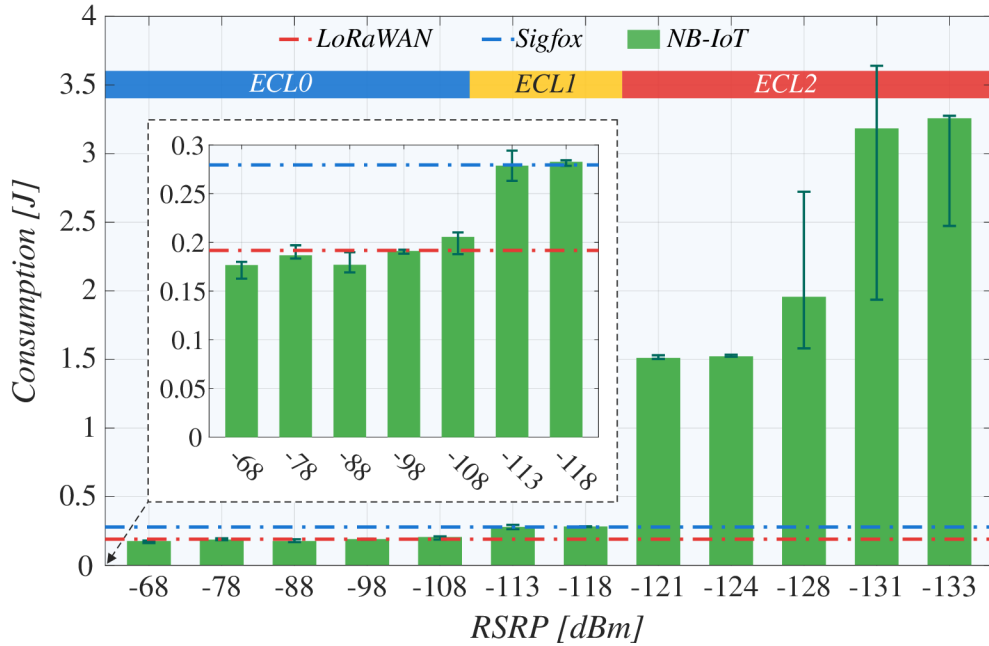
Fig. 5.5: Results of power consumption measurements [107].

may vary significantly, which is also the main reason for the results variation. For LoRaWAN, the consumption of data transmission with SF12 is comparable with NB-IoT operating in ECL0. Surprisingly, Sigfox results show the most significant resemblance with the ECL1 class of NB-IoT [107].

5.2.2 Reinforcement Learning Policies

Even though the primary goal of all RL policies is identical, i.e., achieve the highest average rewards by pulling the right arms, they differ in how the arm is selected. The simplest methods use a purely probabilistic approach without any preferences in exploration phases. However, more advanced algorithms prefer arms with greater chances of getting optimal results. Notably, this problem is also connected with the exploration-exploitation dilemma, i.e., when to choose between the different arms and when it is better to exploit the current one [107].

E-Greedy

The ε-greedy is the most straightforward approach to the exploration-exploitation problem. During the exploration phase, the arms are pulled randomly without any preferences among them. This approach helps ε-greedy policy to overcome issues with the local-optimum solution and discover the arm with the actual highest rewards. Notably, the exploration phase probability is defined by the ε parameter. The rest of the time $(1 - \varepsilon)$, the algorithm operates in the exploitation mode, i.e.,

attempts to gain the highest reward from each action by pulling the same arm. To be able to select the best arm, the algorithm tracks the average rewards from each arm and keeps internal statistics. The average rewards statistics are computed incrementally in order to keep the computational demands low. With this in mind, the value of $k + 1$ action Q_{k+1} is derived as

$$Q_{k+1} = Q_k + \frac{1}{k+1}[r_{k+1} - Q_k], \tag{5.4}$$

where k represents the number of rewards (number of previous steps) in the current action, r_{k+1} is the reward of the actual stage, and Q_k denotes the average of the first k rewards [142].

Weighted Average

The previous ε-greedy greedy algorithm treats all samples as equals, which is suitable for stationary bandits. However, if the environment changes over time (non-stationary problem), the ε-greedy approach performs poorly as all samples have an identical impact on the mean value (internal statistics). For a non-stationary environment, it is reasonable to increase the importance of recent samples over the old ones. To this aim, the weighted average policy introduces a constant step-size parameter that controls how much to weigh the next update of the function. With this modification, the average mean Q_{k+1} is calculated as

$$Q_{k+1} = Q_k + \alpha[r_{k+1} - Q_k], \tag{5.5}$$

where $\alpha(0 < \alpha \leq 1)$ is the step-size constant, r_{k+1} represents actual reward, and Q_k denotes the average of the first k rewards [142].

Upper Confidence Bound

The indiscriminate selection of the arms with the uniform probability distribution employed by the e-greedy algorithm may lead to inefficient exploration. The UCB, on the other hand, favors the exploration of actions with higher potential to reach the optimal value. It follows the principle of optimism, which implies that one should optimistically assume that is the right action in the face of uncertainty. In other words, among the several actions, UCB will optimistically select the action with the highest upper bound of the confidence interval. Initially, UCB explores more to reduce uncertainty systematically, but the exploration decreases over time. By this decision, the UCB obtains, on average, a greater reward than other policies such as ε-greedy or weighted average. The UCB actions use uncertainty in the estimates to

drive exploration according to formula

$$Q_{k+1} = Q_k + c\sqrt{\frac{\ln k}{N_k}},$$ (5.6)

where Q_k represents the current estimate for action at time k, and N_k denotes the number of times action has been triggered before time k. Finally,the exploration phase is driven by the parameter $c > 0$, which controls its degree [143].

The parameter Q_k represents the exploitation part. In this phase, the action with currently the highest estimated reward will be the chosen action. Conversely, the second part describes the exploration phase driven by the parameter c. If the action has not been selected often or not at all, the parameter N_k will be small. As a result, it will lead to significant uncertainty, making this action more likely to be chosen. However, the uncertainty decreases with each selection, making it less likely to be chosen in the exploration phase. Notably, when the action is not selected, its uncertainty will grow slowly due to logarithmic dependency. Conversely, with each selection, the certainty proliferates as the increase in N_k is linear. Thus, as time progress, the exploration gradually decreases as the second part of the equation decreases to zero [143, 144].

Thompson Sampling

The Thompson sampling, similarly to UCB, utilizes advanced methods of arm selection to increase exploration efficiency. Accordingly, Thompson sampling draws from the posterior predictive Beta distribution for each choice employing a random variable with uniform distribution. It allows for sampling of non-optimal distribution with varying frequency. As the certainty of distribution increases, the probability of choice being made dynamically decreases, simultaneously balancing the need for more information by creating a currently optimal choice [145].

The value of $k + 1$ action Q_{k+1} is sampled from the Beta distribution defined as

$$Q_{k+1} = \beta(N_k^1 + 1, N_k^0 + 1),$$ (5.7)

where N_k^1 is the number of times the action got a successful reward prior actual state, whereas N_k^0 denotes the opposite cases, i.e. when the reward was zero. This approach allows the Thomson sampling to balance the exploration-exploitation dilemma. Hence, arms that are not explored as often have a wider variance, increasing their chances of being selected based on stochastic sampling [145].

5.2.3 Average Rewards

As the average rewards are the primary performance metric of RL policies, this study focuses on this parameter in its first phase. In total, each RL policy has been launched 200 times on the input data set containing 5000 samples. These samples are derived from the proposed doubly-stochastic Markov model, which relies on the measurement samples from the conducted measurement campaign (see section 5.1.1). The samples generated by the model are further employed to construct the matrix of rewards for each LPWA technology. In each row, the best performing technology gains the maximum reward of 1. The technology with the second-lowest power consumption is rewarded with the value of 0.5, and, finally, the technology with the highest consumption receives 0 value. This process is conducted for both deployed boards, i.e., module at BUT campus and prototype near the BCC [107].
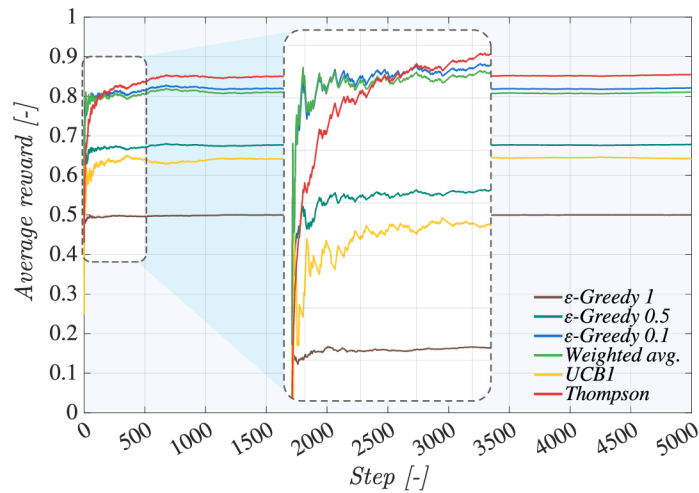
(a) BUT.
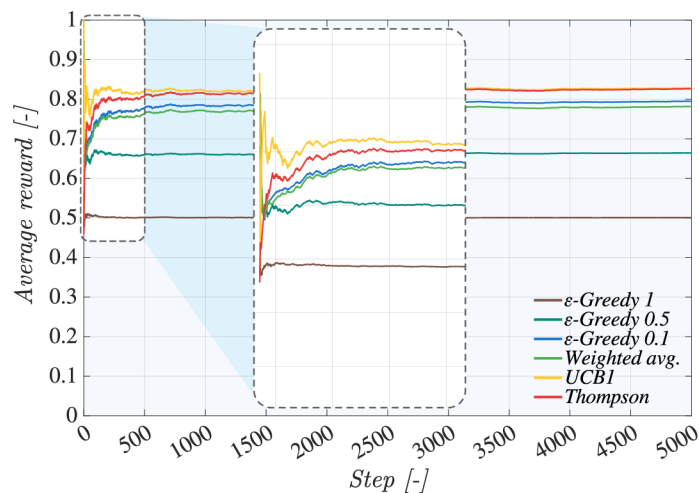
(b) BCC.

Fig. 5.6: Average rewards of reinforcement learning policies [107].

The average rewards for both modules are depicted in Fig. 5.6. In the case of BUT dataset, Thompson sampling indicates the best results of all RL policies. Surprisingly, the UCB algorithm performance is far from the expected values as the average reward is only about 0.63. The main reason for the unsatisfying UCB results is probably the exploitation of local minimum solution as the exploration is reduced over time. The only algorithm which performs worse is the ε-greedy with exploration mode ($\varepsilon = 1$), achieving the expected value of 0.5 rewards on average. Notably, the simple ε-greedy ($\varepsilon = 0.1$, preference for exploitation) policy earns a second place with value of 0.8 average reward. Moreover, the ε-greedy 0.5 shows slightly better results than the UCB policy as well. It suggests that exploitation is a better choice for the current scenario than exploration. Further, the weighted average RL policy with $\alpha = 0.2$ provides satisfactory results as it holds third place with average rewards of more than 0.8 in its steady-state [107].

On the other hand, in the case of the BCC sensor, the UCB policy provides the best performance of all algorithms. By a small margin, the Thompson sampling holds second place, making this policy a reliable option for both scenarios. The remaining technique order is the same as in the case of BUT sensor but the average rewards values are slightly smaller. Surprisingly, the UCB and weighted average policies indicate overshoots in the initial phase of the algorithm runs (first 100 steps). The UCB even achieves the average reward of 1, which represents the maximum achievable value. This behavior is most likely caused by the exploration phase with a certain level of the serendipity of selecting the correct radio interface. However, with subsequent selections, the average rewards decrease to expected levels. Notably, the best performing RL policies, i.e., Thompson sampling and UCB, can exploit up to 85 % of the theoretical gains. Impressively, each RL policy is able to achieve 90 % of its maximum rewards during the initial phase with less than 50 messages. In the case of the UCB algorithm, this phase is even reduced to only 25 samples. Such a short convergence time is especially beneficial for battery-powered devices [107].

5.2.4 Battery Life Expectancy

In the final step of the RL policies assessment, the multi-RAT devices expected battery life is evaluated. To this aim, results of the power consumption characteristics in combination with the extended traces are used. The samples are extended to equal the nominal capacity of the selected battery. For this study, a commonly used lithium thionyl chloride battery (Li/SOCl$_2$) SAFT LS 14500 with the capacity of 2600 mAh (33696 J) is considered [146]. Notably, the intended scenario operates only with the number of transmitted messages. Other influences, such as battery self-discharge, are not considered, although they impact battery life too [107].
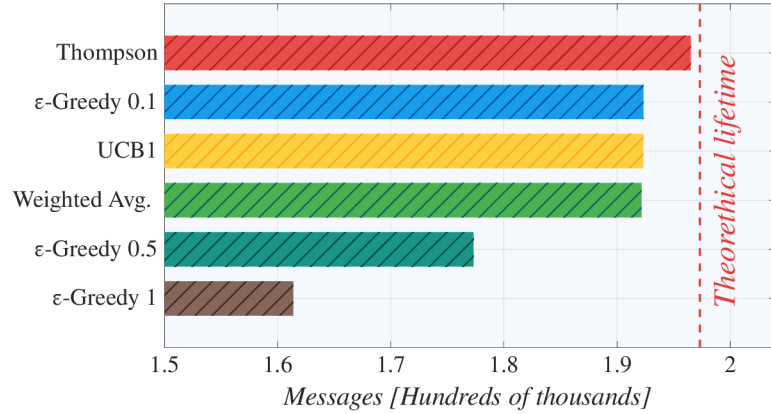
(a) BUT.
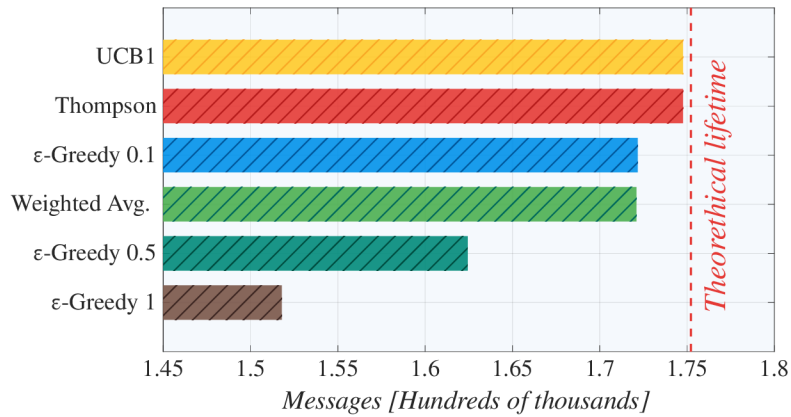
(b) BCC.

Fig. 5.7: Battery life expectancy of reinforcement learning policies [107].

In the case of BUT sensor, it is clear that Thompson sampling provides the most extended battery life, as depicted in Fig. 5.7. Compared to the theoretical maximum when in each step the best performing technology is selected, Thompson sampling is only about 0.5 % worse. The next three policies, i.e., UCB, ε-greedy with ε=0.1, and weighted average, display similar performance by only losing 5-10 % to the theoretical limit. However, not all average rewards characteristics are not directly translated into the predicted battery life. The position of UCB and e-greedy 0.1 are kept, but the remaining UCB, weighted average, and ε-greedy 0.5 policies are interchanged. Notably, the second-worst UCB policy in terms of average rewards occupies third place in predicted battery life. Conversely, the weighted average and ε-greedy 0.5 performance are underwhelming, which may seem counter-intuitive. Nevertheless, a more detailed analysis of the results reveals the reasons for such behavior [107].

Although the UCB average rewards are not the highest, it still manages to select the suboptimal interface represented by the LoRaWAN technology. Since LoRaWAN

consumption is similar to the NB-IoT technology, it creates only a tiny gap between them. Hence, by selecting the LoRaWAN interface in most cases, UCB penalization of low rewards almost vanishes. On the other hand, more straightforward policies such as ε-greedy and weighted average select the radio interfaces in the exploration phase randomly, levering the Sigfox arm, which displays the highest power consumption. This blind selection is the main reason for the performance drop of these two policies in terms of battery life [107].

Recalling the BCC sensor average rewards, the first place of best performing RL policy is held by the UCB algorithm. This fact is also reflected in the expected battery life when it even outperforms the second-best Thompson sampling by a small margin of 500 messages. The generally positive results of Thompson sampling making this policy a promising candidate for deploying in multi-RAT devices [107].

In summary, the results show that for the ε-greedy algorithm, the choice of ε value plays a crucial role. For both sensors, the epsilon values preferring exploitation (closer to zero) indicate far superior results than exploration-focused ones (ε closer to 1). Further, it is also clear that the UCB performance depends heavily on the input data as it provides uneven results. Hence, the non-parametric Thompson sampling, which allows achieving more than $99\,\%$ of a theoretical lifetime in both scenarios, is a preferred option [107].

6 Conclusion

The unprecedented growth of smart devices connected to the Internet providing sensing, monitoring, and actuating sets the stage for the major wireless/cellular evolution towards the mMTC and URLLC as a part of 5G NR. The central pillar of 5G was to bring an enhanced Mobile Broadband (eMBB) to the end customer for the most time. However, the last releases of the 3GPP standard (Rel. 17, Dec. 2020) are finally progressing in the standardization of mMTC. In this regard, LPWA technologies cooperating with the 5G core are considered as an optimal enabler for mMTC. The question of the suitability of these technologies for modern applications is answered in this doctoral thesis via several measurement campaigns and newly proposed evaluation schemes. On top of that, this thesis proposes new propagation models, a coverage assessment metric of LPWA technologies, and discusses the possibility of multi-RAT LPWA operations.

Concerning the propagation models for LPWA technologies, Chapter 3 shows that none of the well-known radio propagation models is capable of capturing the LPWA signal propagation characteristics. On the other hand, proposed fine-tuned models provide significantly improved accuracy compared to the original ones. For NB-IoT, the best performing fine-tuned model provides 40 times improved accuracy over the model in rudimentary form. Even for the LoRaWAN technology, where the accuracy increase is the lowest, the fine-tuned model indicates 9 times better results. To further verify the suitability of newly developed propagation models, their performance is evaluated on the data from the second city of comparable size and geographical constitution. Also, in this experiment, the fine-tuned models show superior performance over the original ones. Notably, the models fine-tuned on measurement data provide almost 40 times more accurate results for NB-IoT and nearly 3 times better values for LoRaWAN. The lowest improvement is visible for Sigfox, with only (but still impressive) 50 % accuracy increase.

In Chapter 4, the new coverage assessment approach is proposed and evaluated. The idea of predicting the signal coverage utilizing sparse data combined with interpolation algorithms is not entirely new, but all previous works were limited only to a single location. Contrary to the mentioned works, the proposed solution is not limited to a single BS estimation but allows multi-cell coverage prediction. On top of that, most of the considered interpolation methods even outperform the fine-tuned propagation models from Chapter 3. Especially the Kriging interpolation provides superior performance in almost all situations. Compared with the propagation models, the developed interpolation-based solution allows dynamically reacting to the changes in the propagation environment and controlling the surface steepness based on the input values.

Further, Chapter 5 consists of three subsequent subtasks. First, it was verified that the long-term characteristics of the radio channel indicate the level-based behavior. It allowed the development of a time doubly-stochastic channel model based on the Markov chains. The main benefit of this model is that it retains analytical traceability. Hence, it can be used either for mathematical or simulation-based studies of LPWA technologies. Next, the power consumption of LPWA modules in various radio conditions was evaluated. This data represents a unique insight into the LPWA module's internal processes. Notably, the NB-IoT repetition scheme in severe radio conditions provides valuable information about the expectable battery life and communication delay in different extended coverage level classes.

Finally, the radio interface selection mechanism for multi-RAT LPWA devices based on RL is implemented. The best performing Thompson sampling and UCB policies can exploit up to 85 % of the theoretical gains, i.e., selecting the wrong interface for transmission only in 15 % of cases. More impressively, these RL policies are able to achieve 90 % of the maximum rewards during the initial phase with less than 50 messages. It allows the multi-RAT device to provide power consumption comparable to a single-RAT solution. In the case of the BCC sensor, the multi-RAT offers even better battery life than the single radio interface device. However, the results are heavily dependent on the input dataset. Because the difference between technologies is only marginal (from the power consumption perspective), the potential benefit of a multi-RAT solution is also limited.

Recall that the main goals of this doctoral thesis cover (i) LPWA technologies propagation models development, (ii) coverage assessment planning, and (iii) multi-RAT solutions for mMTC scenarios. Based on the results mentioned above, it can be stated that the primary goals are successfully accomplished.

Bibliography

[1] T. M. Behera, S. K. Mohapatra, U. C. Samal, M. S. Khan, M. Daneshmand, and A. H. Gandomi, "I-SEP: An Improved Routing Protocol for Heterogeneous WSN for IoT-Based Environmental Monitoring," *IEEE Internet of Things Journal*, vol. 7, no. 1, pp. 710–717, 2020.

[2] K. Shafique, B. A. Khawaja, F. Sabir, S. Qazi, and M. Mustaqim, "Internet of Things (IoT) for Next-Generation Smart Systems: A Review of Current Challenges, Future Trends and Prospects for Emerging 5G-IoT Scenarios," *IEEE Access*, vol. 8, pp. 23022–23040, 2020.

[3] P. Masek, J. Hosek, K. Zeman, M. Stusek, D. Kovac, P. Cika, J. Masek, S. Andreev, and F. Kröpfl, "Implementation of True IoT Vision: Survey on Enabling Protocols and Hands-On Experience," *International Journal of Distributed Sensor Networks*, vol. 12, no. 4, p. 8160282, 2016.

[4] Q. M. Qadir, T. A. Rashid, N. K. Al-Salihi, B. Ismael, A. A. Kist, and Z. Zhang, "Low Power Wide Area Networks: A Survey of Enabling Technologies, Applications and Interoperability Needs," *IEEE Access*, vol. 6, pp. 77454–77473, 2018.

[5] K. Lounis and M. Zulkernine, "Attacks and Defenses in Short-Range Wireless Technologies for IoT," *IEEE Access*, vol. 8, pp. 88892–88932, 2020.

[6] T. Qiu, N. Chen, K. Li, M. Atiquzzaman, and W. Zhao, "How Can Heterogeneous Internet of Things Build Our Future: A Survey," *IEEE Communications Surveys Tutorials*, vol. 20, no. 3, pp. 2011–2027, 2018.

[7] L. Chettri and R. Bera, "A Comprehensive Survey on Internet of Things (IoT) Toward 5G Wireless Systems," *IEEE Internet of Things Journal*, vol. 7, no. 1, pp. 16–32, 2020.

[8] M. Noori, S. Rahimian, and M. Ardakani, "Capacity Region of ALOHA Protocol for Heterogeneous IoT Networks," *IEEE Internet of Things Journal*, vol. 6, no. 5, pp. 8228–8236, 2019.

[9] L. P. Verma and M. Kumar, "An IoT based Congestion Control Algorithm," *Internet of Things*, vol. 9, p. 100157, 2020.

[10] X. Luo, L. Yin, C. Li, C. Wang, F. Fang, C. Zhu, and Z. Tian, "A Lightweight Privacy-Preserving Communication Protocol for Heterogeneous IoT Environment," *IEEE Access*, vol. 8, pp. 67192–67204, 2020.

[11] Cisco, "Cisco Annual Internet Report (2018–2023)," White paper Cisco public, Cisco, March 2020.

[12] B. Foubert and N. Mitton, "Long-Range Wireless Radio Technologies: A Survey," *Future Internet*, vol. 12, no. 1, 2020.

[13] U. Raza, P. Kulkarni, and M. Sooriyabandara, "Low Power Wide Area Networks: An Overview," *IEEE Communications Surveys Tutorials*, vol. 19, pp. 855–873, Secondquarter 2017.

[14] L. Labs, "A Comprehensive Look at Low Power, Wide Area Networks," For 'Internet of Things' Engineers and Decision Makers, Link Labs, 01 2016.

[15] Sigfox, "Sigfox Connected Objects: Radio Specifications," Ref.: EP-SPECS, Rev.: 1.5, Sigfox, February 2020.

[16] N. Naik, "LPWAN Technologies for IoT Systems: Choice Between Ultra Narrow Band and Spread Spectrum," in *2018 IEEE International Systems Engineering Symposium (ISSE)*, pp. 1–8, 2018.

[17] S. D. Antón, D. Fraunholz, C. Lipps, F. Pohl, M. Zimmermann, and H. D. Schotten, "Two Decades of SCADA Exploitation: A Brief History," in *2017 IEEE Conference on Application, Information and Network Security (AINS)*, pp. 98–104, 2017.

[18] H. Kim, "Security and Vulnerability of SCADA Systems over IP-Based Wireless Sensor Networks," *International Journal of Distributed Sensor Networks*, vol. 8, no. 11, p. 268478, 2012.

[19] P. Ilgner, M. Stusek, P. Cika, and M. Sikora, "SCADA-based Message Generator for Multi-Vendor Smart Grids: Integration and Verification of TASE.2," in *2020 12th International Congress on Ultra Modern Telecommunications and Control Systems and Workshops (ICUMT)*, pp. 47–51, 2020.

[20] B. Buurman, J. Kamruzzaman, G. Karmakar, and S. Islam, "Low-Power Wide-Area Networks: Design Goals, Architecture, Suitability to Use Cases and Research Challenges," *IEEE Access*, vol. 8, pp. 17179–17220, 2020.

[21] P. Cerwall, A. Lundvall, P. Jonsson, and S. Carson, "Ericsson Mobility Report," Ericsson White Paper, Ericsson, June 2020.

[22] F. Tounquet and C. Alaton, *Benchmarking Smart Metering Deployment in the EU-28*. Brussels: European Commission, 1 ed., 2019.

[23] DLMS User Association, "COSEM Interface Classes and OBIS Object Identification System," Blue Book Edition 14, DLMS, August 2020.

[24] DLMS User Association, "DLMS/COSEM Architecture and Protocols," Green Book Edition 10, DLMS, August 2020.

[25] ETSI, "5G; Study on Scenarios and Requirements for Next Generation Access Technologies (3GPP TR 38.913 version 15.0.0 Release 15) ," Technical Report v 15.0.0, ETSI, Sophia Antipolis Cedex, September 2018.

[26] S. R. Pokhrel, J. Ding, J. Park, O. S. Park, and J. Choi, "Towards Enabling Critical mMTC: A Review of URLLC Within mMTC," *IEEE Access*, vol. 8, pp. 131796–131813, 2020.

[27] S. Lien, K. Chen, and Y. Lin, "Toward Ubiquitous Massive Accesses in 3GPP Machine-to-Machine Communications," *IEEE Communications Magazine*, vol. 49, no. 4, pp. 66–74, 2011.

[28] A. Kunz, H. Kim, L. Kim, and S. S. Husain, "Machine type communications in 3GPP: From release 10 to release 12," in *2012 IEEE Globecom Workshops*, pp. 1747–1752, 2012.

[29] S. Ahmadi, *5G NR: Architecture, Technology, Implementation, and Operation of 3GPP New Radio Standards*. Academic Press, 2019.

[30] C. Kuhlins, B. Rathonyi, A. Zaidi, and M. Hogan, "Cellular networks for Massive IoT," Ericsson White Paper, Ericsson, January 2020.

[31] I. Poole, "What is 3GPP? An overview." `https://www.electronics-notes.com/`, 2020, (Accessed on 2020-11-23).

[32] R. Ratasuk, N. Mangalvedhe, and A. Ghosh, "Overview of LTE enhancements for cellular IoT," in *2015 IEEE 26th Annual International Symposium on Personal, Indoor, and Mobile Radio Communications (PIMRC)*, pp. 2293–2297, 2015.

[33] S. Chen, R. Ma, H. Chen, H. Zhang, W. Meng, and J. Liu, "Machine-to-Machine Communications in Ultra-Dense Networks—A Survey," *IEEE Communications Surveys Tutorials*, vol. 19, no. 3, pp. 1478–1503, 2017.

[34] H. Holma, A. Toskala, and J. Reunanen, *LTE Small Cell Optimization: 3GPP Evolution to Release 13*. John Wiley & Sons, 2016.

[35] M. Saily, G. Sebire, and E. Riddington, *GSM/EDGE: Evolution and Performance*. John Wiley & Sons, 2011.

[36] T. Halonen, J. Romero, and J. Melero, *GSM, GPRS and EDGE Performance: Evolution Towards 3G/UMTS*. John Wiley & Sons, 2004.

[37] J. Lee, Y. Kim, Y. Kwak, J. Zhang, A. Papasakellariou, T. Novlan, C. Sun, and Y. Li, "LTE-advanced in 3GPP Rel -13/14: an evolution toward 5G," *IEEE Communications Magazine*, vol. 54, no. 3, pp. 36–42, 2016.

[38] A. Hoglund, J. Bergman, X. Lin, O. Liberg, A. Ratilainen, H. S. Razaghi, T. Tirronen, and E. A. Yavuz, "Overview of 3GPP Release 14 Further Enhanced MTC," *IEEE Communications Standards Magazine*, vol. 2, no. 2, pp. 84–89, 2018.

[39] A. Ghosh, A. Maeder, M. Baker, and D. Chandramouli, "5G Evolution: A View on 5G Cellular Technology Beyond 3GPP Release 15," *IEEE Access*, vol. 7, pp. 127639–127651, 2019.

[40] K. Flynn, "Progress on 5G Releases 16/17 in 3GPP," *IEEE Communications Standards Magazine*, vol. 4, no. 2, pp. 4–5, 2020.

[41] 3GPP, "About 3GPP." `https://www.3gpp.org/about-3gpp`, 2020, (Accessed on 2020-11-23).

[42] L. Casaccia, "Understanding 3GPP – Starting With the Basics." `https://www.qualcomm.com/`, 2017, (Accessed on 2020-11-23).

[43] M. Condoluci and T. Mahmoodi, ""softwarization and virtualization in 5g mobile networks: Benefits, trends and challenges"," *Computer Networks*, vol. 146, pp. 65 – 84, 2018.

[44] E. Dahlman, S. Parkvall, and J. Skold, *4G: LTE/LTE-advanced for Mobile Broadband*. Academic press, 2013.

[45] M. Floeck, A. Papageorgiou, A. Schuelke, and J. Song, "Horizontal M2M Platforms Boost Vertical Industry: Effectiveness Study for Building Energy Management Systems," in *2014 IEEE World Forum on Internet of Things (WF-IoT)*, pp. 15–20, 2014.

[46] C. Gomez and J. Paradells, "Wireless home automation networks: A survey of architectures and technologies," *IEEE Communications Magazine*, vol. 48, no. 6, pp. 92–101, 2010.

[47] M. Bouzidi, Y. Dalveren, F. A. Cheikh, and M. Derawi, "Use of the IQRF Technology in Internet-of-Things-Based Smart Cities," *IEEE Access*, vol. 8, pp. 56615–56629, 2020.

[48] A.-B. Garca-Hernando, J.-F. Martnez-Ortega, J.-M. Lpez-Navarro, A. Prayati, and L. Redondo-Lpez, *Problem Solving for Wireless Sensor Networks.* Springer Publishing Company, Incorporated, 1 ed., 2008.

[49] P. Seflova, V. Sulc, J. Pos, and R. Spinar, "IQRF wireless technology utilizing IQMESH protocol," in *2012 35th International Conference on Telecommunications and Signal Processing (TSP)*, pp. 101–104, 2012.

[50] P. Masek, D. Hudec, J. Krejci, A. Ometov, J. Hosek, S. Andreev, F. Kroepfl, and Y. Koucheryavy, "Advanced Wireless M-Bus Platform for Intensive Field Testing in Industry 4.0-Based Systems," in *European Wireless 2018; 24th European Wireless Conference*, pp. 1–6, 2018.

[51] K. Zeman, P. Masek, J. Krejci, A. Ometov, J. Hosek, S. Andreev, and F. Kroepfl, "Wireless M-BUS in Industrial IoT: Technology Overview and Prototype Implementation," in *European Wireless 2017; 23th European Wireless Conference*, pp. 1–6, 2017.

[52] S. Spinsante, M. Pizzichini, M. Mencarelli, S. Squartini, and E. Gambi, "Evaluation of the Wireless M-Bus Standard for Future Smart Water Grids," in *2013 9th International Wireless Communications and Mobile Computing Conference (IWCMC)*, pp. 1382–1387, 2013.

[53] P. Masek, M. Stusek, K. Zeman, R. Mozny, A. Ometov, and J. Hosek, "A Perspective on Wireless M-Bus for Smart Electricity Grids," in *2019 42nd International Conference on Telecommunications and Signal Processing (TSP)*, pp. 730–735, 2019.

[54] Radiocrafts, "Wireless M-Bus Products." `https://radiocrafts.com/`, 2020, (Accessed on 2020-11-23).

[55] Coronis, "Wavefront™ A Cost-Optimized Wavenis™ RF Front-End for OEM Integration." `https://www.elster.com/`, 2010, (Accessed on 2020-11-23).

[56] O. Liberg, M. Sundberg, Y.-P. E. Wang, J. Bergman, J. Sachs, and G. Wikström, *Cellular Internet of Things.* Academic Press, second edition ed., 2020.

[57] GSMA, "NB-IoT Deployment Guide to Basic Feature set Requirements," White Paper, GSMA, June 2019.

[58] GSMA, "LTE-M Deployment Guide to Basic Feature Set Requirements," White Paper, GSMA, June 2019.

[59] M. Stusek, D. Moltchanov, P. Masek, K. Mikhaylov, O. Zeman, M. Roubicek, Y. Koucheryavy, and J. Hosek, "Accuracy Assessment and Cross-Validation of LPWAN Propagation Models in Urban Scenarios," *IEEE Access*, vol. 8, pp. 154625–154636, 2020.

[60] K. Mikhaylov, M. Stusek, P. Masek, R. Fujdiak, R. Mozny, S. Andreev, and J. Hosek, "Communication Performance of a Real-Life Wide-Area Low-Power Network Based on Sigfox Technology," in *ICC 2020 - 2020 IEEE International Conference on Communications (ICC)*, pp. 1–6, 2020.

[61] LoRa Alliance Technical Committee, "LoRaWAN® L2 1.0.4 Specification (TS001-1.0.4)," L2 1.0.4 Specification, LoRa Alliance, October 2020.

[62] K. Mikhaylov, M. Stusek, P. Masek, R. Fujdiak, R. Mozny, S. Andreev, and J. Hosek, "On the Performance of Multi-Gateway LoRaWAN Deployments: An Experimental Study," in *2020 IEEE Wireless Communications and Networking Conference (WCNC)*, pp. 1–6, 2020.

[63] D. Poluektov, M. Polovov, P. Kharin, M. Stusek, K. Zeman, P. Masek, I. Gudkova, J. Hosek, and K. Samouylov, ""on the performance of lorawan in smart city: End-device design and communication coverage"," in *Distributed Computer and Communication Networks* (V. M. Vishnevskiy, K. E. Samouylov, and D. V. Kozyrev, eds.), (Cham), pp. 15–29, Springer International Publishing, 2019.

[64] P. Masek, M. Stusek, K. Zeman, J. Hosek, K. Mikhaylov, S. Andreev, Y. Koucheryavy, O. Zeman, J. Votapek, and M. Roubicek, "Tailoring NB-IoT for Mass Market Applications: A Mobile Operator's Perspective," in *2018 IEEE Globecom Workshops (GC Wkshps)*, pp. 1–7, 2018.

[65] C. Bockelmann, N. K. Pratas, G. Wunder, S. Saur, M. Navarro, D. Gregoratti, G. Vivier, E. De Carvalho, Y. Ji, Č. Stefanović, P. Popovski, Q. Wang, M. Schellmann, E. Kosmatos, P. Demestichas, M. Raceala-Motoc, P. Jung, S. Stanczak, and A. Dekorsy, "Towards Massive Connectivity Support for Scalable mMTC Communications in 5G Networks," *IEEE Access*, vol. 6, pp. 28969–28992, 2018.

[66] R. S. Sinha, Y. Wei, and S.-H. Hwang, "A survey on LPWA technology: LoRa and NB-IoT," *ICT Express*, vol. 3, no. 1, pp. 14 – 21, 2017.

[67] M. Stusek, K. Zeman, P. Masek, J. Sedova, and J. Hosek, "IoT Protocols for Low-power Massive IoT: A Communication Perspective," in *2019 11th International Congress on Ultra Modern Telecommunications and Control Systems and Workshops (ICUMT)*, pp. 1–7, 2019.

[68] R. Fujdiak, K. Mikhaylov, M. Stusek, P. Masek, I. Ahmad, L. Malina, P. Porambage, M. Voznak, A. Pouttu, and P. Mlynek, ""17 - security in low-power wide-area networks: state-of-the-art and development toward the 5g"," in *LPWAN Technologies for IoT and M2M Applications* (B. S. Chaudhari and M. Zennaro, eds.), pp. 373 – 396, Academic Press, 2020.

[69] Sigfox, "Introducing 0G Network." `https://www.sigfox.com/`, 2020, (Accessed on 2020-11-24).

[70] S. Popli, R. K. Jha, and S. Jain, "A Survey on Energy Efficient Narrowband Internet of Things (NBIoT): Architecture, Application and Challenges," *IEEE Access*, vol. 7, pp. 16739–16776, 2019.

[71] J. L. Aufranc, "A Look at LoRaWAN and NB-IoT Power Consumption." `https://www.cnx-software.com/`, 2018, (Accessed on 2020-11-24).

[72] Sierra Wireless, "Coverage Analysis of LTE-M Category-M1," White Paper, Sierra Wireless, January 2017.

[73] P. Masek, M. Stusek, K. Zeman, R. Drapela, A. Ometov, and J. Hosek, "Implementation of 3GPP LTE Cat-M1 Technology in NS-3: System Simulation and Performance," in *2019 11th International Congress on Ultra Modern Telecommunications and Control Systems and Workshops (ICUMT)*, pp. 1–7, 2019.

[74] R. M. Sandoval, S. Canovas-Carrasco, A. Garcia-Sanchez, and J. Garcia-Haro, "A Reinforcement Learning-Based Framework for the Exploitation of Multiple RATs in the IoT," *IEEE Access*, vol. 7, pp. 123341–123354, 2019.

[75] K. Mikhaylov, V. Petrov, R. Gupta, M. A. Lema, O. Galinina, S. Andreev, Y. Koucheryavy, M. Valkama, A. Pouttu, and M. Dohler, "Energy Efficiency of Multi-Radio Massive Machine-Type Communication (MR-MMTC): Applications, Challenges, and Solutions," *IEEE Communications Magazine*, vol. 57, no. 6, pp. 100–106, 2019.

[76] Y. Lu, M. Gerasimenko, R. Kovalchukov, M. Stusek, J. Urama, J. Hosek, M. Valkama, and E. S. Lohan, "Feasibility of Location-Aware Handover for Autonomous Vehicles in Industrial Multi-Radio Environments," *Sensors*, vol. 20, no. 21, 2020.

[77] A. Kirimtat, O. Krejcar, A. Kertesz, and M. F. Tasgetiren, "Future Trends and Current State of Smart City Concepts: A Survey," *IEEE Access*, vol. 8, pp. 86448–86467, 2020.

[78] N. H. Mahmood, S. Böcker, A. Munari, F. Clazzer, I. Moerman, K. Mikhaylov, O. Lopez, O.-S. Park, E. Mercier, H. Bartz, *et al.*, "White Paper on Critical and Massive Machine Type Communication Towards 6G," *arXiv preprint arXiv:2004.14146*, 2020.

[79] T. M. Ho, T. D. Tran, T. T. Nguyen, S. M. A. Kazmi, L. B. Le, C. S. Hong, and L. Hanzo, "Next-generation Wireless Solutions for the Smart Factory, Smart Vehicles, the Smart Grid and Smart Cities," 2019.

[80] R. Mozny, M. Stusek, P. Masek, K. Mikhaylov, and J. Hosek, "Unifying Multi-Radio Communication Technologies to Enable mMTC Applications in B5G Networks," in *2020 2nd 6G Wireless Summit (6G SUMMIT)*, pp. 1–5, 2020.

[81] J. Lianghai, A. Weinand, B. Han, and H. D. Schotten, "Multi-RATs Support to Improve V2X Communication," in *2018 IEEE Wireless Communications and Networking Conference (WCNC)*, pp. 1–6, 2018.

[82] J. Urama, M. Gerasimenko, M. Stusek, P. Masek, S. Andreev, J. Hosek, and Y. Koucheryavy, "A Multi-Purpose Automated Vehicular Platform with Multi-Radio Connectivity Capabilities," in *2018 IEEE 87th Vehicular Technology Conference (VTC Spring)*, pp. 1–7, 2018.

[83] K. Mikhaylov, M. Stusek, P. Masek, V. Petrov, J. Petajajarvi, S. Andreev, J. Pokorny, J. Hosek, A. Pouttu, and Y. Koucheryavy, "Multi-RAT LPWAN in Smart Cities: Trial of LoRaWAN and NB-IoT Integration," in *2018 IEEE International Conference on Communications (ICC)*, pp. 1–6, 2018.

[84] H. C. Leligou, T. Zahariadis, L. Sarakis, E. Tsampasis, A. Voulkidis, and T. E. Velivassaki, "Smart Grid: a Demanding Use Case for 5G Technologies," in *2018 IEEE International Conference on Pervasive Computing and Communications Workshops (PerCom Workshops)*, pp. 215–220, 2018.

[85] R. Diba, E. Yaacoub, M. Al-Husseini, H. Noura, K. Abualsaud, T. Khattab, and M. Guizani, "A Simple Approach for Securing IoT Data Transmitted over Multi-RATs," in *2018 14th International Wireless Communications Mobile Computing Conference (IWCMC)*, pp. 249–254, 2018.

[86] S. Saafi, J. Hosek, and A. Kolackova, "Cellular-enabled Wearables in Public Safety Networks: State of the Art and Performance Evaluation," in *2020*

12th International Congress on Ultra Modern Telecommunications and Control Systems and Workshops (ICUMT), pp. 201–207, 2020.

[87] K. Mekki and E. Bajic and F. Chaxel and F. Meyer, "A Comparative Study of LPWAN Technologies for Large-Scale IoT Deployment," *ICT Express*, vol. 5, no. 1, pp. 1–7, 2019. Available from: `http://www.sciencedirect.com/science/article/pii/S2405959517302953`.

[88] R. El Chall, S. Lahoud, and M. El Helou, "LoRaWAN Network: Radio Propagation Models and Performance Evaluation in Various Environments in Lebanon," *IEEE Internet of Things Journal*, vol. 6, no. 2, pp. 2366–2378, 2019.

[89] E. Teng, J. Falcao, C. Ruiz, F. Mokaya, P. Zhang, and B. Iannucci, "Aerial Sensing and Characterization of Three-Dimensional RF Fields," in *Second International Workshop on Robotic Sensor Networks*, 04 2015.

[90] E. Harinda, S. Hosseinzadeh, H. Larijani, and R. M. Gibson, "Comparative Performance Analysis of Empirical Propagation Models for LoRaWAN 868 MHz in an Urban Scenario," in *2019 IEEE 5th World Forum on Internet of Things (WF-IoT)*, pp. 154–159, April 2019.

[91] V. S. Abhayawardhana, I. J. Wassell, D. Crosby, M. P. Sellars, and M. G. Brown, "Comparison of Empirical Propagation Path Loss Models for Fixed Wireless Access Systems," in *2005 IEEE 61st Vehicular Technology Conference*, vol. 1, pp. 73–77 Vol. 1, May 2005.

[92] 3GPP, "LTE; Evolved Universal Terrestrial Radio Access (E-UTRA); Radio Frequency (RF) System Scenarios (3GPP TR 36.942 version 15.0.0 Release 15)," ETSI TR 136 942 V15.0.0, 3GPP, July 2018.

[93] E. Damosso, *Digital Mobile Radio Towards Future Generation Systems*. Brussels,: Directorate-General Telecommunications, Information society, Information Market, and Exploitation of Research, 1 ed., 1999.

[94] A. El-Nashar, M. El-Saidny, and M. Sherif, *Design, Deployment and Performance of 4G-LTE Networks: A Practical Approach*. Wiley Publishing, 1st ed., 2014.

[95] L. M. Correia, "A View of the COST 231-Bertoni-Ikegami Model," in *2009 3rd European Conference on Antennas and Propagation*, pp. 1681–1685, March 2009.

[96] V. Erceg, L. J. Greenstein, S. Y. Tjandra, S. R. Parkoff, A. Gupta, B. Kulic, A. A. Julius, and R. Bianchi, "An Empirically Based Path Loss Model for Wireless Channels in Suburban Environments," *IEEE Journal on Selected Areas in Communications*, vol. 17, pp. 1205–1211, July 1999.

[97] A. Ikpehai, B. Adebisi, K. M. Rabie, K. Anoh, R. E. Ande, M. Hammoudeh, H. Gacanin, and U. M. Mbanaso, "Low-Power Wide Area Network Technologies for Internet-of-Things: A Comparative Review," *IEEE Internet of Things Journal*, vol. 6, pp. 2225–2240, April 2019.

[98] D. Har, A. M. Watson, and A. G. Chadney, "Comment on Diffraction Loss of Rooftop-to-street in COST 231-Walfisch-Ikegami Model," *IEEE Transactions on Vehicular Technology*, vol. 48, no. 5, pp. 1451–1452, 1999.

[99] Adeunis, "FTD: Network Tester." Available from: `https://www.adeunis.com`. Accessed: 2020-05-14.

[100] LoRa Alliance®, "RP002-1.0.1® Regional Parameters," Final, LoRa Alliance®, Beaverton, February 2020.

[101] A. M. Yousuf, E. M. Rochester, B. Ousat, and M. Ghaderi, "Throughput, Coverage and Scalability of LoRa LPWAN for Internet of Things," in *2018 IEEE/ACM 26th International Symposium on Quality of Service (IWQoS)*, pp. 1–10, 2018.

[102] A. Lavric, A. I. Petrariu, and V. Popa, "Long Range SigFox Communication Protocol Scalability Analysis Under Large-Scale, High-Density Conditions," *IEEE Access*, vol. 7, pp. 35816–35825, 2019.

[103] uBlox, "SARA-N2 Modules AT Commands Manual." Available from: `https://www.u-blox.com`. Accessed: 2020-12-15.

[104] M. Bahjat, T. Rahman, O. Abdul Aziz, M. Hindia, and E. Hanafi, "Channel Characterization and Path Loss Modeling in Indoor Environment at 4.5, 28, and 38 GHz for 5G Cellular Networks," *International Journal of Antennas and Propagation*, vol. 2018, pp. 1–14, 09 2018.

[105] M. Stusek, D. Moltchanov, P. Masek, K. Mikhaylov, J. Hosek, S. Andreev, Y. Koucheryavy, P. Kustarev, O. Zeman, and M. Roubicek, "LPWAN Coverage Assessment Planning without Explicit Knowledge of Base Station Locations," *IEEE Internet of Things Journal*, pp. 1–1, 2021.

[106] M. Stusek, D. Moltchanov, P. Masek, S. Andreev, Y. Koucheryavy, and J. Hosek, "Time-Dependent Propagation Analysis and Modeling of LPWAN Technologies," in *2020 IEEE Global Communications Conference*, pp. 1–6, december 2020.

[107] M. Stusek, D. Moltchanov, P. Masek, J. Hosek, S. Andreev, and Y. Koucheryavy, "Learning-Aided Multi-RAT Operation for Battery Lifetime Extension in LPWAN Systems," in *12th International Congress on Ultra Modern Telecommunications and Control Systems and Workshops (ICUMT)*, pp. 26–32, 2020.

[108] M. Aernouts, R. Berkvens, K. Van Vlaenderen, and M. Weyn, "Sigfox and LoRaWAN Datasets for Fingerprint Localization in Large Urban and Rural Areas," *Data*, vol. 3, p. 13, Apr 2018.

[109] Y. Liu, W. Huangfu, H. Zhang, and K. Long, "Multi-Criteria Coverage Map Construction Based on Adaptive Triangulation-Induced Interpolation for Cellular Networks," *IEEE Access*, vol. 7, pp. 80767–80777, June 2019.

[110] M. Lauridsen, H. Nguyen, B. Vejlgaard, I. Z. Kovacs, P. Mogensen, and M. Sorensen, "Coverage Comparison of GPRS, NB-IoT, LoRa, and SigFox in a 7800 km^2 Area," in *2017 IEEE 85th Vehicular Technology Conference (VTC Spring)*, pp. 1–5, June 2017.

[111] R. V. Akhpashev and V. G. Drozdova, "Spatial Interpolation of LTE Measurements for Minimization of Drive Tests," in *2018 19th International Conference of Young Specialists on Micro/Nanotechnologies and Electron Devices (EDM)*, pp. 6403–6405, June 2018.

[112] H. Braham, S. Ben Jemaa, B. Sayrac, G. Fort, and E. Moulines, "Coverage mapping using spatial interpolation with field measurements," in *2014 IEEE 25th Annual International Symposium on Personal, Indoor, and Mobile Radio Communication (PIMRC)*, pp. 1743–1747, Sep. 2014.

[113] J. Talvitie, M. Renfors, and E. S. Lohan, "Distance-Based Interpolation and Extrapolation Methods for RSS-Based Localization With Indoor Wireless Signals," *IEEE Transactions on Vehicular Technology*, vol. 64, pp. 1340–1353, April 2015.

[114] "Interpolating Scattered Data," 2019.

[115] P. Getreuer, "Linear Methods for Image Interpolation," *Image Processing On Line*, vol. 1, pp. 238–259, 2011.

[116] K. Hormann and N. Sukumar, *Generalized Barycentric Coordinates in Computer Graphics and Computational Mechanics.* CRC press, 2017.

[117] Y. Diao, Z. Lin, and M. Fu, "A Barycentric Coordinate Based Distributed Localization Algorithm for Sensor Networks," *IEEE Transactions on Signal Processing*, vol. 62, pp. 4760–4771, Sep. 2014.

[118] S. W. Park, L. Linsen, O. Kreylos, J. D. Owens, and B. Hamann, "Discrete Sibson Interpolation," *IEEE Transactions on Visualization and Computer Graphics*, vol. 12, pp. 243–253, March 2006.

[119] R. Sibson, "A Brief Description of Natural Neighbor Interpolation," in *Interpolating multivariate data*, (New York), pp. 21–36, John Wiley & Sons, 1981.

[120] P. M. Bartier and C. Keller, "Multivariate Interpolation to Incorporate Thematic Surface Data Using Inverse Distance Weighting (IDW)," *Computers & Geosciences*, vol. 22, no. 7, pp. 795 – 799, 1996.

[121] D. Shepard, "A Two-dimensional Interpolation Function for Irregularly-spaced Data," in *Proceedings of the 1968 23rd ACM National Conference*, ACM '68, (New York, NY, USA), pp. 517–524, ACM, 1968.

[122] Q. Zhang and J. Wu, "Image Super-resolution Using Windowed Ordinary Kriging Interpolation," *Optics Communications*, vol. 336, pp. 140 – 145, 2015.

[123] A. McBratney and R. Webster, "Choosing Functions for Semi-variograms of Soil Properties and Fitting Them to Sampling Estimates," *Journal of soil Science*, vol. 37, no. 4, pp. 617–639, 1986.

[124] M. R. Inggs and R. T. Lord, "Interpolating Satellite Derived Wind Field Data using Ordinary Kriging, with application to the Nadir Gap," *IEEE Transactions on Geoscience and Remote Sensing*, vol. 34, pp. 250–256, January 1996.

[125] S. K. Sharma and X. Wang, "Toward Massive Machine Type Communications in Ultra-Dense Cellular IoT Networks: Current Issues and Machine Learning-Assisted Solutions," *IEEE Communications Surveys & Tutorials*, vol. 22, no. 1, pp. 426–471, 2020.

[126] International Telecommunication Union, "Guidelines for Evaluation of Radio Interface Technologies for IMT-2020," Report ITU-R M.2412-0, ITU-R, October 2017.

[127] A. Mukherjee, *5G New Radio: Beyond Mobile Broadband.* Artech House, 2019.

[128] V. Petrov, A. Samuylov, V. Begishev, D. Moltchanov, S. Andreev, K. Samouylov, and Y. Koucheryavy, "Vehicle-based Relay Assistance for Opportunistic Crowdsensing over Narrowband IoT (NB-IoT)," *IEEE Internet of Things journal*, vol. 5, no. 5, pp. 3710–3723, 2017.

[129] S. Karlin, *A First Course in Stochastic Processes.* Elsevier Science, 2014.

[130] T. C. Krehbiel, "Correlation Coefficient Rule of Thumb," *Decision Sciences Journal of Innovative Education*, vol. 2, no. 1, pp. 97–100, 2004.

[131] A. Dürre, R. Fried, and T. Liboschik, "Robust Estimation of (Partial) Autocorrelation," *Wiley Interdisciplinary Reviews: Computational Statistics*, vol. 7, no. 3, pp. 205–222, 2015.

[132] S. B. Slimane and T. Le-Ngoc, "A Doubly Stochastic Poisson Model for Self-Similar Traffic," in *Proceedings IEEE International Conference on Communications ICC'95*, vol. 1, pp. 456–460, IEEE, 1995.

[133] D. Moltchanov, Y. Koucheryavy, and J. Harju, "The Model of Single Smoothed MPEG Traffic Source Based on the D-BMAP Arrival Process with Limited State Space," in *Proceedings of ICACT*, pp. 55–60, 2003.

[134] L. Rabiner and B. Juang, "An Introduction to Hidden Markov Models," *IEEE ASSP Magazine*, vol. 3, no. 1, pp. 4–16, 1986.

[135] A. Ometov, D. Moltchanov, M. Komarov, S. V. Volvenko, and Y. Koucheryavy, "Packet Level Performance Assessment of mmWave Backhauling Technology for 3GPP NR Systems," *IEEE Access*, vol. 7, pp. 9860–9871, 2019.

[136] W. Khreich, E. Granger, A. Miri, and R. Sabourin, "A survey of Techniques for Incremental Learning of HMM Parameters," *Information Sciences*, vol. 197, pp. 105–130, 2012.

[137] M. J. Gales, "Maximum Likelihood Linear Transformations for HMM-Based Speech Recognition," *Computer Speech & Language*, vol. 12, no. 2, pp. 75–98, 1998.

[138] Y. Huang, X. Chen, and W. B. Wu, "Recursive Nonparametric Estimation for Time Series," *IEEE Transactions on Information Theory*, vol. 60, pp. 1301–1312, Feb 2014.

[139] A. Hinneburg and D. A. Keim, "A General Approach to Clustering in Large Databases with Noise," *Knowledge and Information Systems*, vol. 5, no. 4, pp. 387–415, 2003.

[140] P. Burns, "Robustness of the Ljung-Box Test and Its Rank Equivalent," *Available at SSRN 443560*, 2002.

[141] R. Mozny, P. Masek, M. Stusek, K. Zeman, A. Ometov, and J. Hosek, "On the Performance of Narrow-band Internet of Things (NB-IoT) for Delay-tolerant Services," in *2019 42nd International Conference on Telecommunications and Signal Processing (TSP)*, pp. 637–642, 2019.

[142] R. S. Sutton and A. G. Barto, *Reinforcement learning: An introduction.* MIT Press, 2018.

[143] T. Lattimore and C. Szepesvári, "Bandit Algorithms," *Cambridge University Press (preprint)*, 2018.

[144] B. Hao, Y. Abbasi-Yadkori, Z. Wen, and G. Cheng, "Bootstrapping Upper Confidence Bound," *arXiv preprint arXiv:1906.05247*, 2019.

[145] D. J. Russo, B. V. Roy, A. Kazerouni, I. Osband, and Z. Wen, "A Tutorial on Thompson Sampling," *Foundations and Trends® in Machine Learning*, vol. 11, no. 1, pp. 1–96, 2018.

[146] Saft, "LS 14500 Primary Li-SOCl$_2$: High energy density 3.6 V AA-size bobbin cell." Available from: `https://www.saftbatteries.com/`. Accessed: 2021-03-01.

List of Symbols, Quantities and Abbreviations

3GPP	Third-Generation Partnership Project.
ACF	Autocorrelation Function.
ADR	Adaptive Data Rate.
AES	Advanced Encryption Standard.
ALOHA	Abramson's Logic of Hiring Access.
AR	Augmented Reality.
BCC	Brno city center.
BPSK	Binary-Phase Shift Keying.
BS	Base Station.
BUT	Brno University of Technology.
CDF	Cumulative Distribution Function.
CDMA	Code Division Multiple Access.
CoMP	Coordinated Multipoint.
COSEM	Companion Specification for Energy Metering.
COST	European Cooperation in Science and Technology.
CP	Cyclic Prefix.
CQI	Channel Quality Indicator.
CR	Coding Rate.
CSD	Circuit-Switched Data.
CSS	Chirp Spread Spectrum.
D2D	Device to Device.
DBPSK	Differential Binary Phase Shift Keying.
DC	Duty Cycle.
DCI	Downlink Control Information.
DECT	Digital Enhanced Cordless Telecommunications.
DL	Downlink.
DLMS	Device Language Message Specification.
DR	Data Rate.
DRX	Discontinuous Reception.

EARFCN	E-UTRA Absolute Radio Frequency Channel Number.
E-CID	Enhanced Cell ID.
ECL	Enhanced Coverage Level.
ED	End-Device.
EDGE	Enhanced Data rates for GSM Evolution.
eDRX	Extended Discontinuous Reception.
EDT	Early Data Transmission.
EFR	Enhanced Full Rate.
EIRP	Equivalent Isotropically Radiated Power.
eMBB	enhanced Mobile Broadband.
eNodeB	evolved Node B.
ERP	Effective Radiated Power.
EU	European Union.
FD	Full Duplex.
FDD	Frequency Division Duplex.
FHSS	Frequency Hopping Spread Spectrum.
FRK	Fixed Rank Kriging.
FSK	Frequency Shift Keying.
GFSK	Gaussian Frequency Shift Keying.
GPRS	General Packet Radio Service.
GSM	Global System for Mobile Communication.
GW	Gateway.
H2H	Human-to-Human.
HARQ	Hybrid Automatic Repeat Request.
HD	Half Duplex.
HetIoT	Heterogeneous IoT.
HetNet	Heterogeneous Network.
HSDPA	High-Speed Downlink Packet Access.
HSPA	High-Speed Packet Access.
HSUPA	High-Speed Uplink Packet Access.
IDW	Inverse Distance Weighting.
IMS	IP-Multimedia Subsystem.

IMSI	International Mobile Subscriber Identity.
IMT-Advanced	International Mobile Telecommunications-Advanced.
IoT	Internet of Things.
IP	Internet Protocol.
IQRF	Intelligent Radio Frequency.
ISM	Industrial, Scientific and Medical.
ITU	International Telecommunication Union.
KDE	Kernel Density Estimation.
LBS	Location Based Services.
LBT	Listen Before Talk.
LoRa	Long Range.
LoS	Line-of-Sight.
LPWA	Low-Power Wide-Area.
LPWAN	Low-Power Wide-Area Network.
LTE	Long Term Evolution.
MAE	Mean Absolut Error.
M-BUS	Meter BUS.
M2M	Machine-to-Machine.
MAB	Multi-Armed Bandit.
MAC	Medium Access Control.
MBMS	Multimedia Broadcast Multicast Service.
MCL	Maximum Coupling Loss.
MIB	Master Information Block.
MIMO	Multiple-Input Multiple-Output.
ML	Machine Learning.
MME	Mobility Management Entity.
mMTC	massive Machine-Type Communication.
MPDCCH	MTC Physical Downlink Control Channel.
MR	Multi Radio.
MTC	Machine-Type Communication.
MTI	Multi-Criteria Triangulation-induced Interpolation.

NB-IoT	Narrowband IoT.
NFC	Near Field Communication.
NLoS	Non-Line-of-Sight.
NPDCCH	Narrowband physical downlink control channel.
NPDSCH	Narrowband Physical Downlink Shared Channel.
NPRACH	Narrowband Physical Random Access Channel.
NPUSH	Narrowband Physical Uplink Channel.
NR	New Radio.
OFDMA	Orthogonal Frequency-Division Multiple Access.
OSI	Open Systems Interconnection.
OTDOA	Observed Time Difference Of Arrival.
PAPR	Peak-to-Average Power Ratio.
PDCCH	Physical Downlink Control Channel.
PDCP	Packet Data Convergence Protocol.
PDF	Probability Density Function.
PDSCH	Physical Downlink Shared Channel.
PMF	Probability Mass Function.
PRACH	Physical Random Access Channel.
PRB	Physical Resource Block.
P-RNTI	Paging-Radio Network Temporary Identifier.
PHY	Physical Layer.
PLC	Programmable Logic Controller.
PLMN	Public Land Mobile Network.
PS	Packet Switched.
PSD	Power Spectral Density.
PSK	Phase Shift Keying.
PSM	Power Saving Mode.
PTT	Push to Talk.
PTW	Paging Transmission Window.
PUSH	Physical Uplink Shared Channel.

QAM	Quadrature Amplitude Modulation.
QoS	Quality of Service.
QPSK	Quadrature Phase Shift Keying.
RAT	Radio Access Technology.
RC	Radio Configuration.
RF	Radio Frequency.
RL	Reinforcement Learning.
RMSE	Root Mean Square Error.
RNC	Radio Network Controller.
RRC	Radio Resource Control.
RRM	Radio resource management.
RRU	Remote Radio Unit.
RSRP	Reference Signal Receive Power.
RSS	Received Signal Strength.
RSSI	Received Signal Strength Indicator.
RW	Receive Window.
SC-FDMA	Singe Carrier Frequency Division Multiple Access.
SCADA	Supervisory Control and Data Acquisition.
SCHC	Static Context Header Compression and Fragmentation.
SDU	Service Data Unit.
SF	Spreading Factor.
SIB	System Information Block.
SINR	Signal to Interference plus Noise Ratio.
SNR	Signal-to-Noise Ratio.
SUI	Stanford University Interim.
TAU	Tracking Area Update.
TBCC	Tail-Biting Convolutional Code.
TBS	Transport Block Size.
TDD	Time-Division Duplexing.
TDMA	Time-Division Multiple Access.
ToA	Time on Air.

UAV	Unmanned Aerial Vehicle.
UCB	Upper Confidence Bound.
UDP	User Datagram Protocol.
UE	User Equipment.
UL	Uplink.
UMTS	Universal Mobile Telecommunications System.
UNB	Ultra-Narrowband.
URLLC	Ultra-Reliable Low-Latency Communication.
USIM	Universal Subscriber Identity Module.
V2X	Vehicle to Everything.
VoIP	Voice over Internet Protocol.
VoLTE	Voice over LTE.
VR	Virtual Reality.
VRN	Virtual Routing Number.
WCDMA	Wideband Code Division Multiple Access.
WI	Walfish-Ikegami.
WiMAX	Worldwide Interoperability for Microwave Access.
WLAN	Wireless Local Area Network.